Electronic Supplementary Information for

From Small Changes to Big Gains: Pyridinium-Based Tetralactam Macrocycle for Enhanced Sugar Recognition in Water

Canjia Zhai[1], Ethan Cross Zulueta[1], Alexander Mariscal[1], Chengkai Xu[1], Yunpeng Cui[1], Xudong Wang[2], Huang Wu[3], Carson Doan[1], Lukasz Wojtas[1], Haixin Zhang[4], Jianfeng Cai[1], Libin Ye[2], Kun Wang[4,5], Wenqi Liu*[1].

[1]Department of Chemistry, University of South Florida, Tampa, FL, 33620, USA

[2]Department of Cell Biology, Microbiology and Molecular Biology, University of South Florida, Tampa, FL, 33620, USA

[3]Department of Chemistry, The University of Hong Kong, Hong Kong SAR 999077, China

[4]Department of Physics, University of Miami, Coral Gables, Florida 33146, USA

[5]Department of Chemistry, University of Miami, Coral Gables, Florida 33146, USA

Table of contents

1. General Method

All Commercially available solvents and chemicals were purchased from Sigma-Aldrich and Fisher Scientific and used without further purification unless otherwise stated. Water was deionized and micro-filtered through a Milli-Q water filtration system. Reactions were monitored by analytical thin-layer chromatography (TLC) on silica gel 60-F_{254} plates, visualized by an ultraviolet (254 nm) lamp. Nuclear magnetic resonance (NMR) spectra were recorded on the Varian Unity Inova 600 MHz spectrometer or Varian Unity Inova 400 MHz system. Variable temperature NMR experiment was conducted on Bruker Avance III 600 MHz system. The chemical shift was presented in ppm and referenced by residual non-deuterated solvent peaks ($CDCl_3$: δ = 7.26 ppm, D_2O: δ = 4.79 ppm, DMSO-d_6: δ = 2.50 ppm). The ^{1}H DOSY NMR spectra were acquired using a convection-compensated gradient-stimulated echo pulse sequence (DgsteSL_cc). Spectral processing was executed with Agilent VrnmJ 4.2 software, and diffusion coefficient extraction was performed using the Mono-exponential Fit feature in MestReNova 14.2. The experimental setup included a fixed delay of 50 ms. Gradient strength calculations adhered to the formula: $\gamma^2 g^2 \delta^2 (\Delta - \delta/3)$, where γ denotes the gyromagnetic ratio, g the native gradient strength, δ the gradient duration, and Δ the echo delay. High-resolution mass spectrometry (HRMS) was obtained on Agilent LC-MS QTOF 6540 using an ESI source or Waters Synapt G2 mass spectrometer using an ESI source. Matrix-assisted laser desorption/ionization-time of flight (MALDI-TOF) mass spectrometry was performed by Bruker UltrafleXtreme spectrometer using trans-2-[3-(4-tert-Butylphenyl)-2-methyl-2-propenylidene]malononitrile as a matrix substance. Circular dichroism spectra were recorded on the JASCO J-1500 Circular Dichroism Spectrophotometer. UV-Vis absorption spectra were collected by Thermo Scientific Evolution 201 UV/Vis Spectrometer. Flash Column chromatography was performed using a Biotage Selekt system with silica gel (SilicaFlash P60 from SILICYCLE) as the stationary phase. Isothermal titration was performed on the MicroCal iTC_{200} system, and samples were all filtered through a 0.45 μm PTFE filter before use. ITC Data were analyzed using MicroCal iTC_{200} analysis software. Detailed experimental procedures are provided below in the appropriate sections of this supporting information.

2. Synthesis and Compounds Characterization

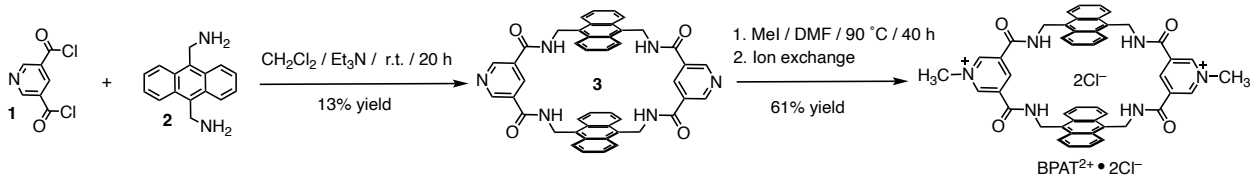

Scheme S1. Synthesis of $BPAT^{2+}$•$2Cl^-$ by a high dilution method.

Tetralactam macrocycle **3**: A solution of pyridine-3,5-dicarbonyl dichloride1 (2.8 g, 13.7 mmol, 1.2 equiv.) in anhydrous CH_2Cl_2 (50 mL) was added dropwise over 6 h by a mechanical syringe pump into a stirred solution containing anthracene methylenediamine 2 (2.7g, 11.4 mmol, 1 equiv.) and Et_3N (9.6 mL, 69 mmol, 6 equiv.) in anhydrous CH_2Cl_2 (700 mL). The reaction solution was stirred at room temperature for 20 h. When the reaction was complete, Et_3N (15 mL) was added to the reaction solution, and the reaction mixture was filtered and rinsed with 40% MeOH/CH_2Cl_2. The filtrate was collected, and the solvent was removed by vacuum to get a light yellow solid. The residue was washed with water (150 mL) and then acetone (150 mL) to get the product tetralactam macrocycle **3** as a light yellow solid (534 mg, yield 13%). R_f = 0.4 (CH_2Cl_2: MeOH = 95: 5). ^{1}H NMR (400 MHz, $CDCl_3$) δ 9.82 (s, 4H), 8.98 (s, 2H), 8.03 (d, *J* = 7.8 Hz, 8H), 7.89 (s, 4H), 7.45 (d, *J* = 7.8 Hz, 8H), 5.59 (d, *J* = 4.5 Hz, 8H). ^{13}C NMR (101 MHz, $CDCl_3$) δ 163.2, 162.8, 162.3, 161.9, 161.8, 145.6, 141.1, 133.1, 130.3, 127.5, 127.1, 123.8, 118.7, 115.9, 113.1, 110.2. Note: The tetralactam macrocycle **3** exhibits poor solubility in $CDCl_3$. To obtain high-resolution ^{1}H NMR and ^{13}C NMR spectra, a trace amount of TFA as an additive was introduced into the $CDCl_3$ solution, enhancing its solubility. HRMS(ESI) *m/z:* $[M+H^+]^+$ Calcd for $[C_{46}H_{35}N_6O_4]^+$ 735.2714; found:735.2696.

$BPAT^{2+}$•$2Cl^-$: A solution of the tetralactam macrocycle **3** (200 mg, 0.272 mmol, 1 equiv.) and iodomethane (1.2 mL, 16.32 mmol, 60 equiv.) in DMF (3 mL) was stirred at 90 ˚C for 40 h. After cooling to room temperature, the solvent was removed by vacuum to generate a yellow solid as pure $BPAT^{2+}$•$2I^-$. ^{1}H NMR (400 MHz, DMSO-d_6) δ 9.58 (s, 4H), 9.35 (d, *J* = 5.4 Hz, 4H), 8.54 (s, 2H), 8.40 – 8.24 (m, 8H), 7.57 – 7.43 (m, 8H), 5.49 (d, *J* = 5.1 Hz, 8H), 4.55 (s, 6H). The solid was redissolved in hot DMSO (80 mL). A solution (20 mL) of KPF_6 (5 g, 27.16 mmol, 100 equiv.) in DMSO was added to the previous solution, followed by the addition of water (300 mL). The resulting precipitate was centrifuged, dried, and redissolved in MeCN (300

mL). A solution (100 mL) of tetrabutylammonium chloride (22 g, 82 mmol, 600 equiv.) in MeCN was added to form a precipitate, which was further washed with MeCN (200 mL) to get product $BPAT^{2+}$•$2Cl^-$ as light-yellow solid (138 mg, yield 61%). ^{1}H NMR (600 MHz, D_2O) δ 8.84 (d, *J* = 1.6 Hz, 4H), 8.37 (s, 2H), 8.29 – 8.13 (m, 8H), 7.59 (dd, *J* = 7.3, 2.9 Hz, 4H), 7.34 (d, *J* = 7.4 Hz, 4H), 5.80 (d, *J* = 15.1 Hz, 4H), 5.39 (d, *J* = 14.9 Hz, 4H), 3.01 (s, 6H). ^{1}H NMR (400 MHz, DMSO-d_6) δ 9.59 (s, 4H), 9.49 (s, 4H), 8.70 (s, 2H), 8.33 (dd, *J* = 7.0, 3.4 Hz, 8H), 7.58 – 7.44 (m, 8H), 5.48 (d, *J* = 5.2 Hz, 8H), 4.54 (s, 6H). ^{1}H NMR (400 MHz, D_2O, 0.8 mM) δ 8.90 (s, 4H), 8.49 (s, 2H), 8.38 – 8.21 (m, 8H), 7.66 (dd, *J* = 7.0, 3.1 Hz, 4H), 7.40 (d, *J* = 7.8 Hz, 4H), 5.84 (d, *J* = 15.0 Hz, 4H), 5.46 (d, *J* = 15.1 Hz, 4H), 3.08 (s, 6H). ^{1}H NMR (400 MHz, D_2O, 0.017 mM) δ 9.57 (s, 4H), 8.96 (s, 2H), 8.27 (s, 8H), 7.57 (d, *J* = 7.9 Hz, 8H), 5.52 (s, 8H), 4.64 (s, 6H).^{13}C NMR (101 MHz, DMSO-d_6) δ 161.4, 147.7, 139.9, 132.5, 129.9, 129.8, 126.0, 125.1, 48.6, 36.1. HRMS(ESI) *m/z:* [*M*–Cl^-]$^+$ Calcd for $[C_{48}H_{40}ClN_6O_4]^+$ 799.2800; found 799.2774.

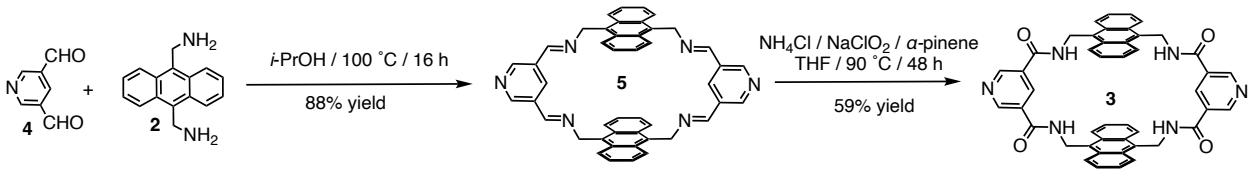

Scheme S2. Synthesis of tetralactam macrocycle **3** by a dynamic approach.

Imine macrocycle **5**: Pyridine-3,5-dicarbaldehyde **4** (100 mg, 0.74 mmol, 1 equiv.) and anthracene methylenediamine **2** (175 mg, 0.74 mmol, 1 equiv.) were added to isopropanol (6 mL). The reaction mixture was stirred at 100 ˚C overnight. The reaction was cooled to room temperature, and the solvent was removed under vacuum. The residue was washed with MeOH (10 mL × 2) to get the imine macrocycle **5** as a yellow solid (217 mg, yield 88%). ^{1}H NMR (400 MHz, $CDCl_3$) δ 9.20 (s, 4H), 8.09 (dd, *J* = 7.1, 3.3 Hz, 8H), 7.79 (s, 4H), 7.43 (dd, *J* = 7.2, 3.1 Hz, 8H), 5.88 (s, 8H). MALDI-TOF *m/z:* [*M*+Na^+]$^+$ Calcd for $[C_{46}H_{34}N_6Na]^+$ 693.3; found:693.7.

Tetralactam macrocycle **3**: A mixture of imine macrocycle **5** (200 mg, 0.298 mmol, 1 equiv.), $NaClO_2$ (647 mg, 7.16 mmol, 24 equiv.), NH_4Cl (128 mg, 2.38 mmol, 8 equiv.) and α-pinene (1.9 mL, 11.9 mmol, 40 equiv.) in anhydrous THF (5 mL) was stirred at 90 ˚C for 48 h. The solvent was then removed by vacuum. The residue was washed with water (12 mL × 3), acetone (10 mL × 3) and a small amount of DMF (2 mL) to get the tetralactam macrocycle **3** as a yellow solid (130 mg, yield 59%).

3. Mass Spectrometry

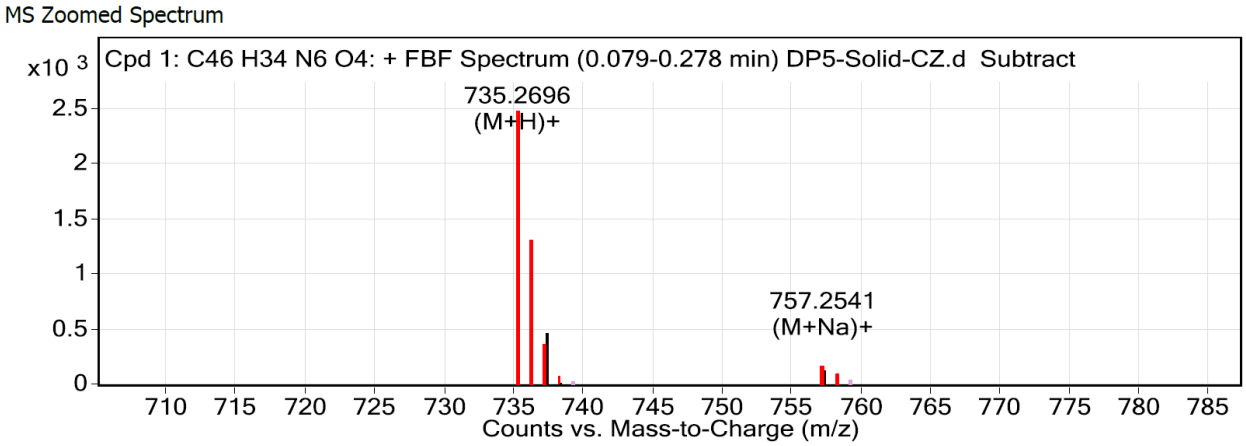

Fig. S1. HRMS (ESI) spectrum of tetralactam macrocycle **3**.

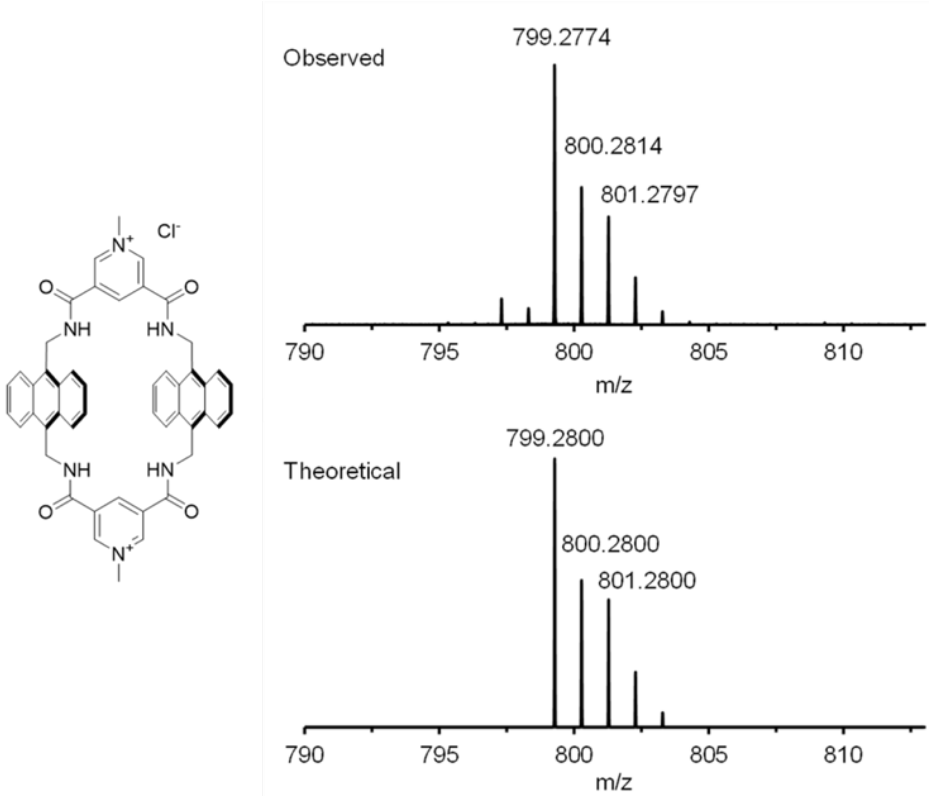

Fig. S2. HRMS(ESI) spectrum of $BPAT^{2+}\bullet Cl^{-}$.

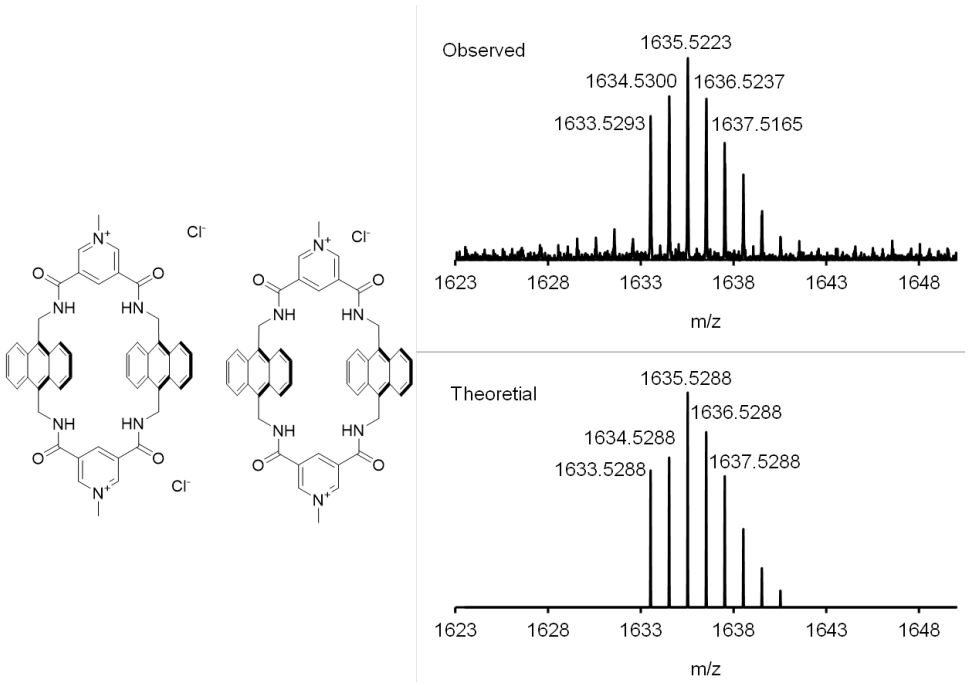

Fig. S3. HRMS (ESI) spectrum of $2BPAT^{2+}\bullet 3Cl^{-}$.

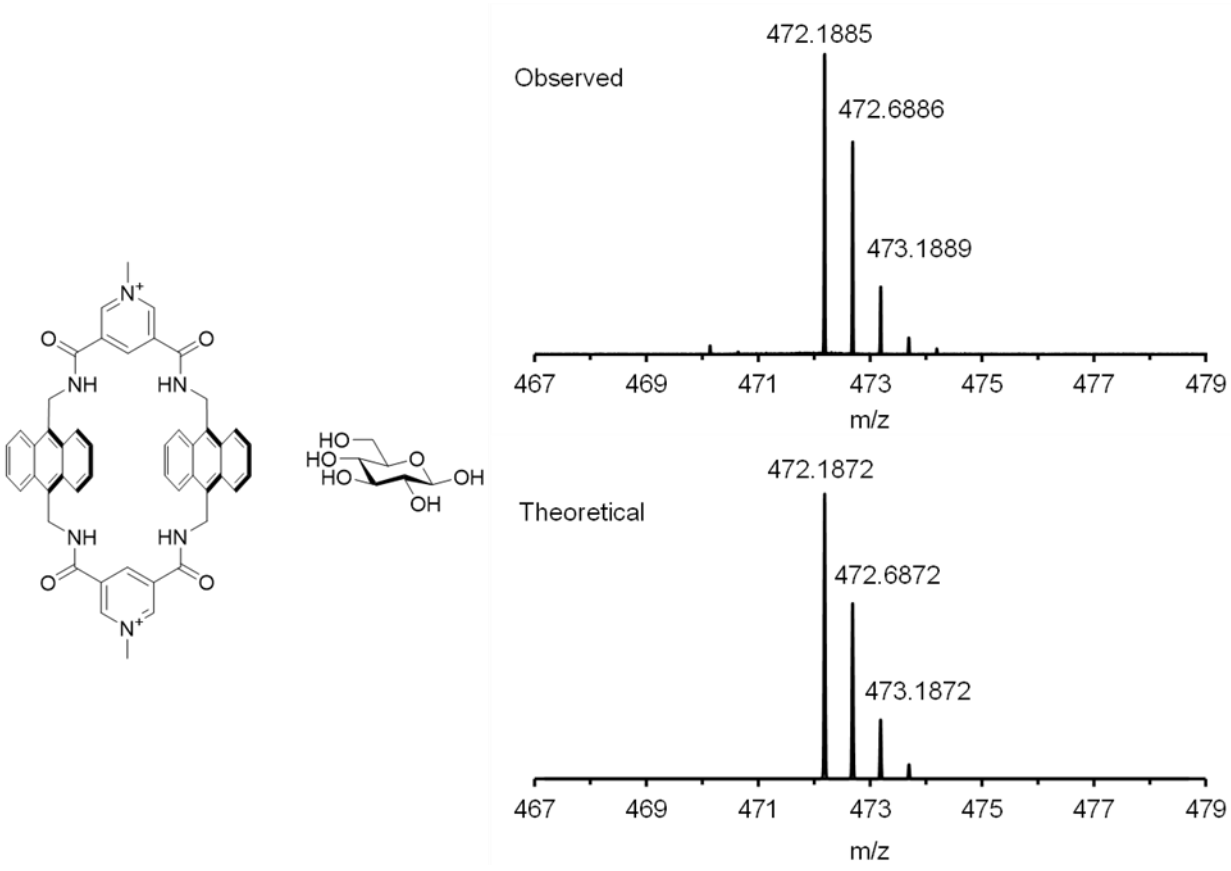

Fig. S4. HRMS (ESI) spectrum of glucose $\subset BPAT^{2+}$.

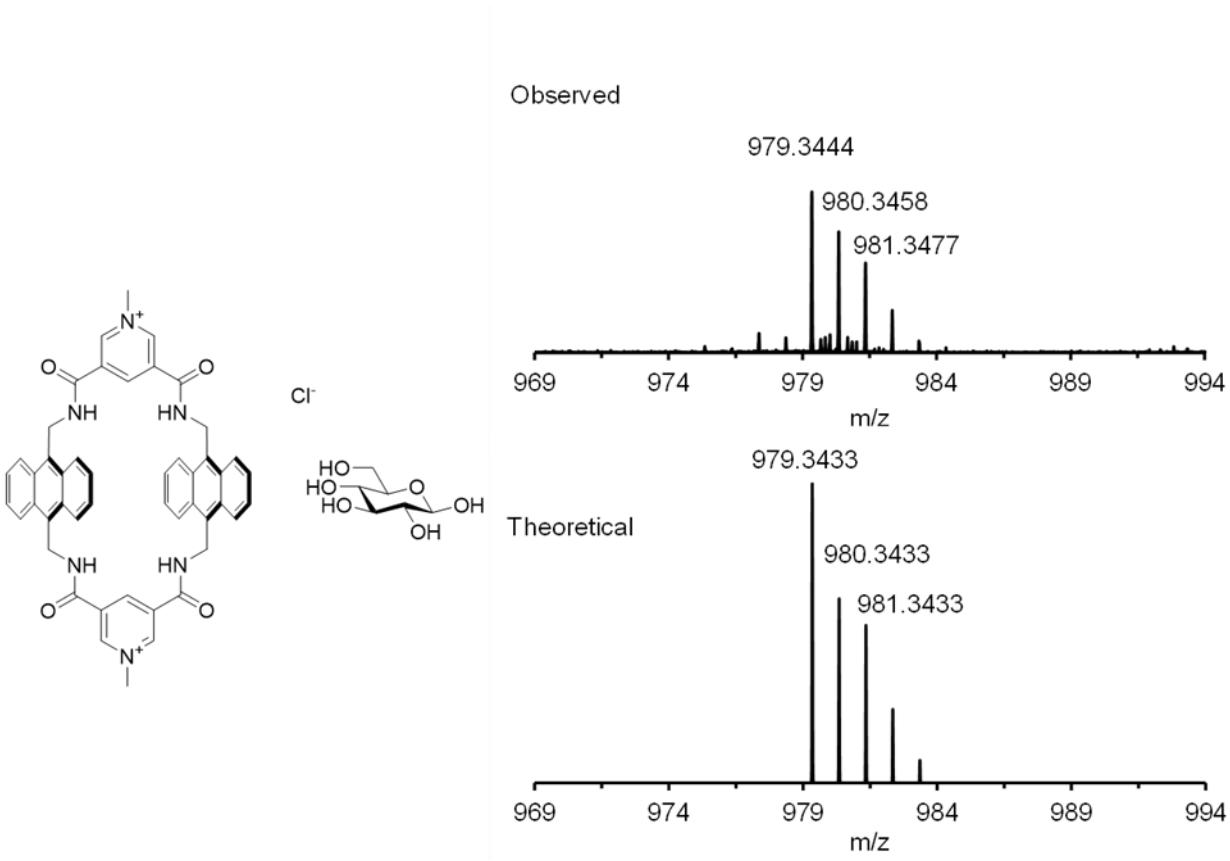

Fig. S5. HRMS (ESI) spectrum of glucose ⊂$BPAT^{2+}$•Cl^{-}.

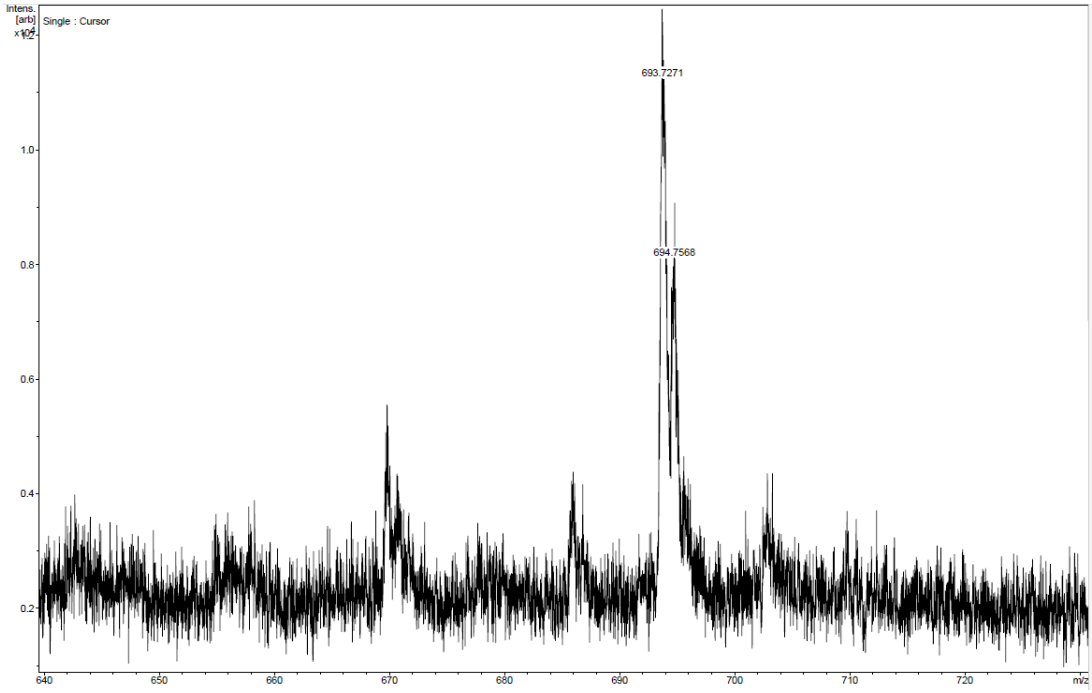

Fig. S6. MALDI-TOF spectrum of the imine macrocycle **5**.

4. NMR Spectroscopy

Compound characterization

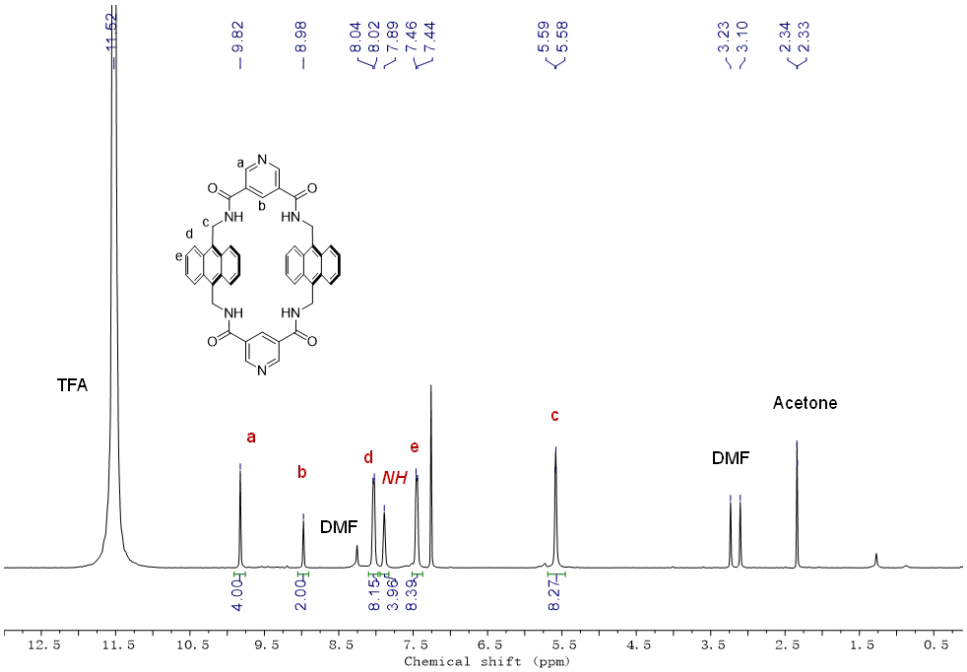

Fig. S7. ^{1}H NMR spectrum (400 MHz, $CDCl_3$, 298 K) of the tetralactam macrocycle **3** with TFA as additive.

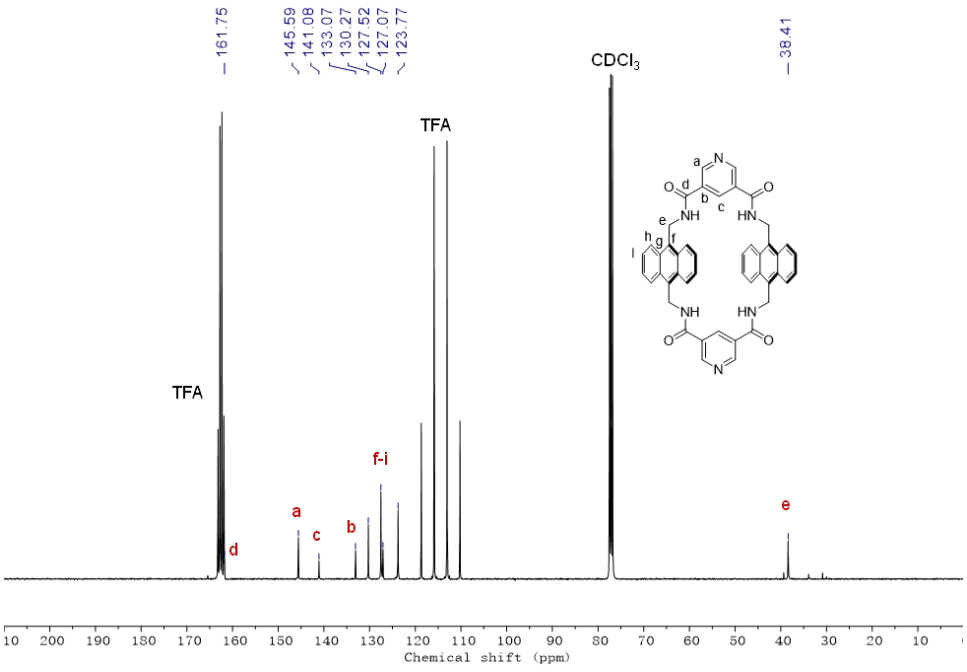

Fig. S8. ^{13}C NMR spectrum (101 MHz, $CDCl_3$, 298 K) of the tetralactam macrocycle **3** with TFA as additive.

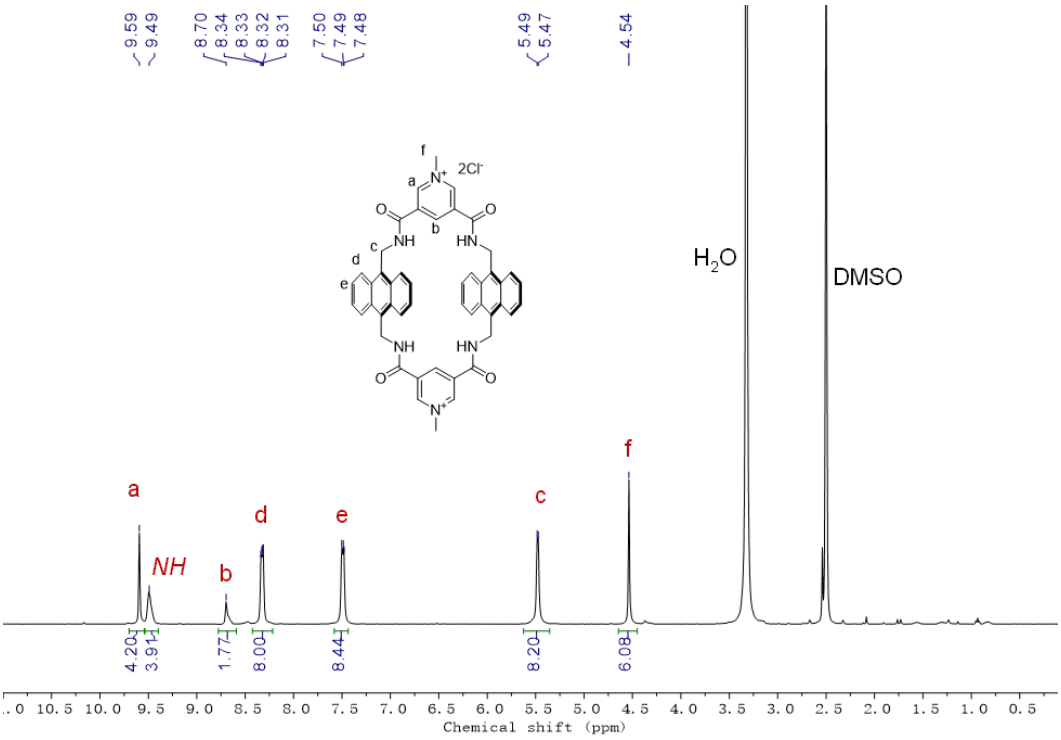

Fig. S9. ^{1}H NMR spectrum (400 MHz, DMSO-d_6, 298 K) of $BPAT^{2+}\bullet 2Cl^{-}$.

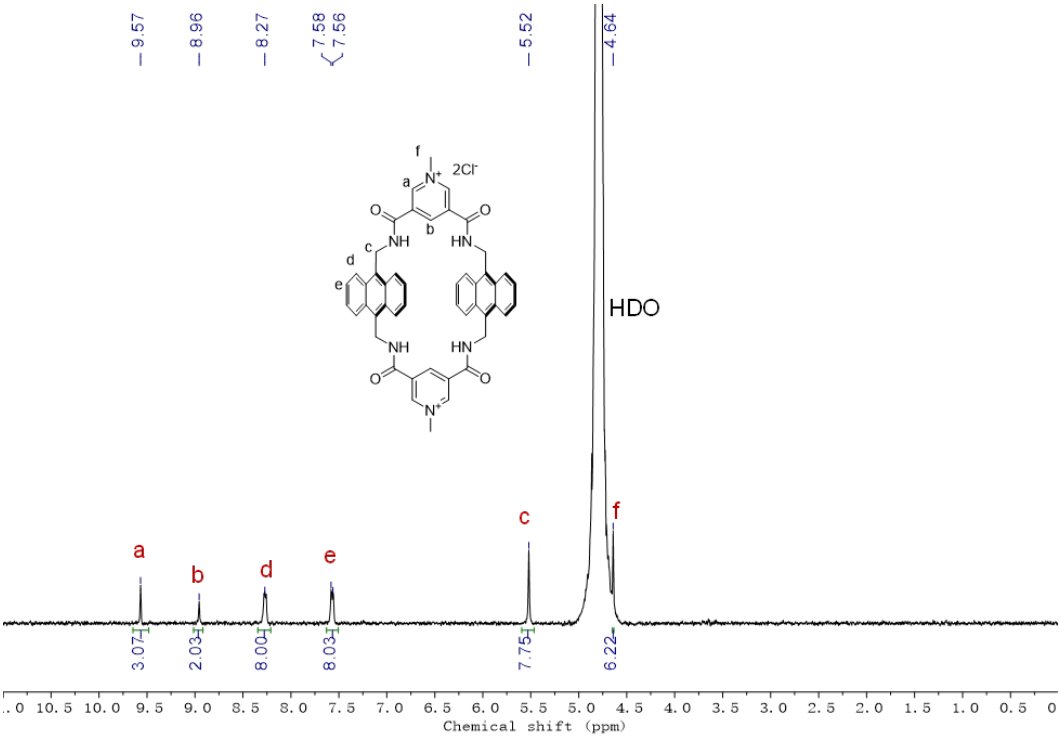

Fig. S10. ^{1}H NMR spectrum (400 MHz, D_2O, 298 K) of $BPAT^{2+}\bullet 2Cl^{-}$ (0.017 mM) in its free form.

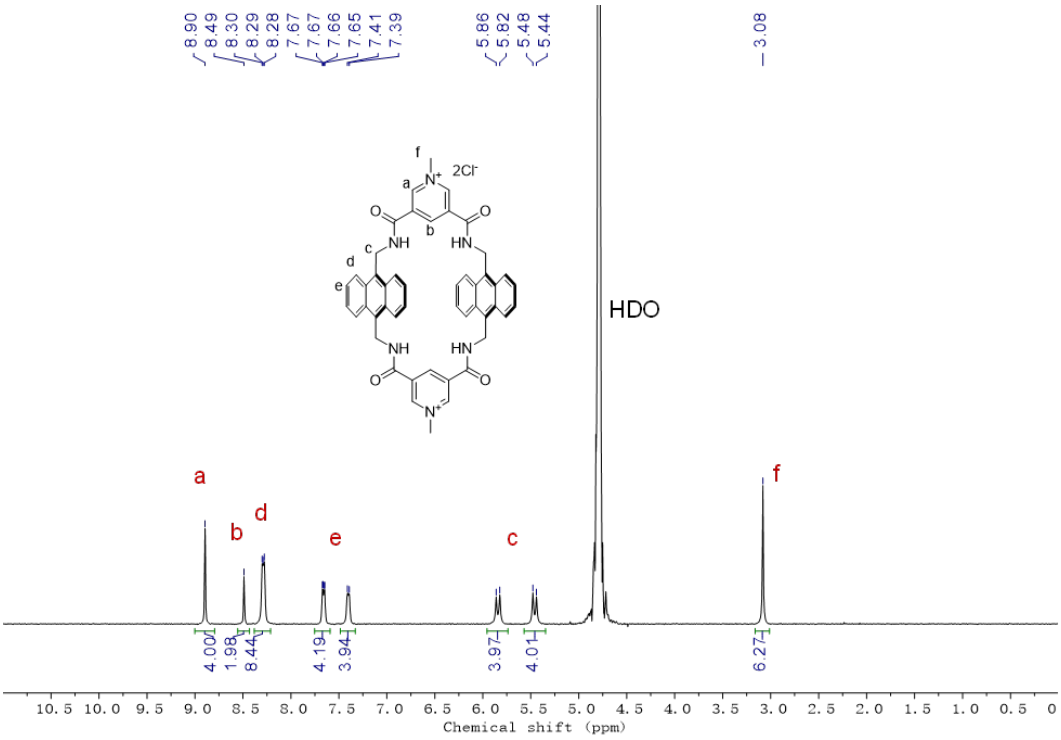

Fig. S11. ^{1}H NMR spectrum (400 MHz, D_2O, 298 K) of $BPAT^{2+}\bullet 2Cl^-$ (0.8 mM) in its aggregated form.

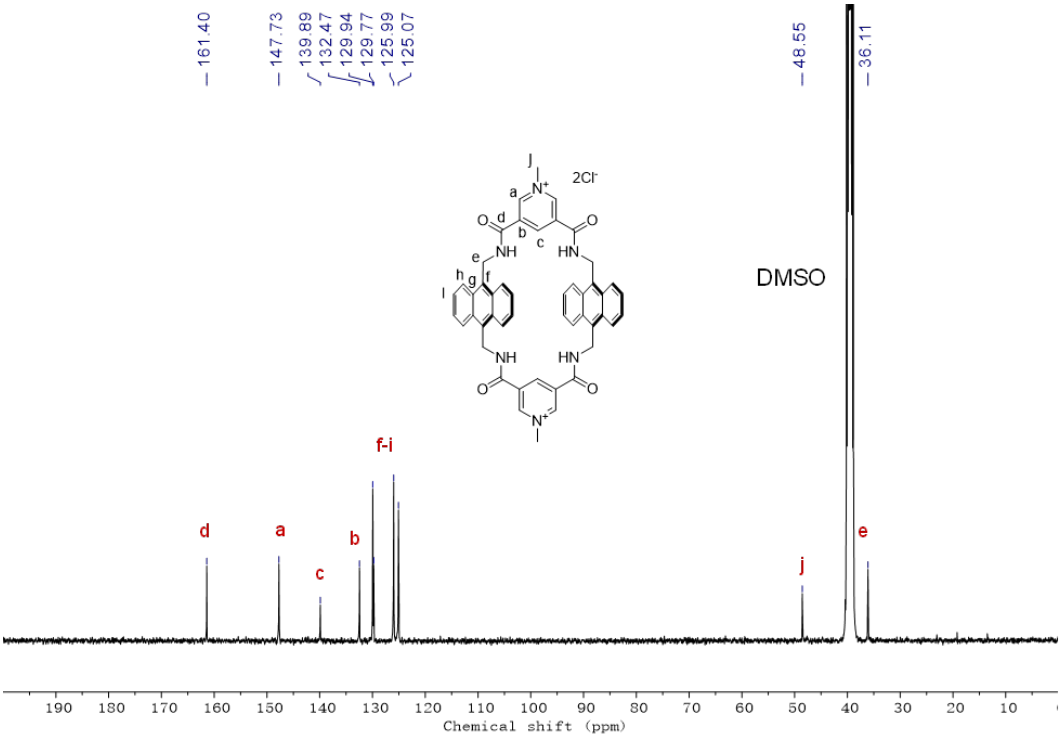

Fig. S12. ^{13}C NMR spectrum (101 MHz, DMSO-d_6, 298 K) of compound $BPAT^{2+}\bullet 2Cl^-$.

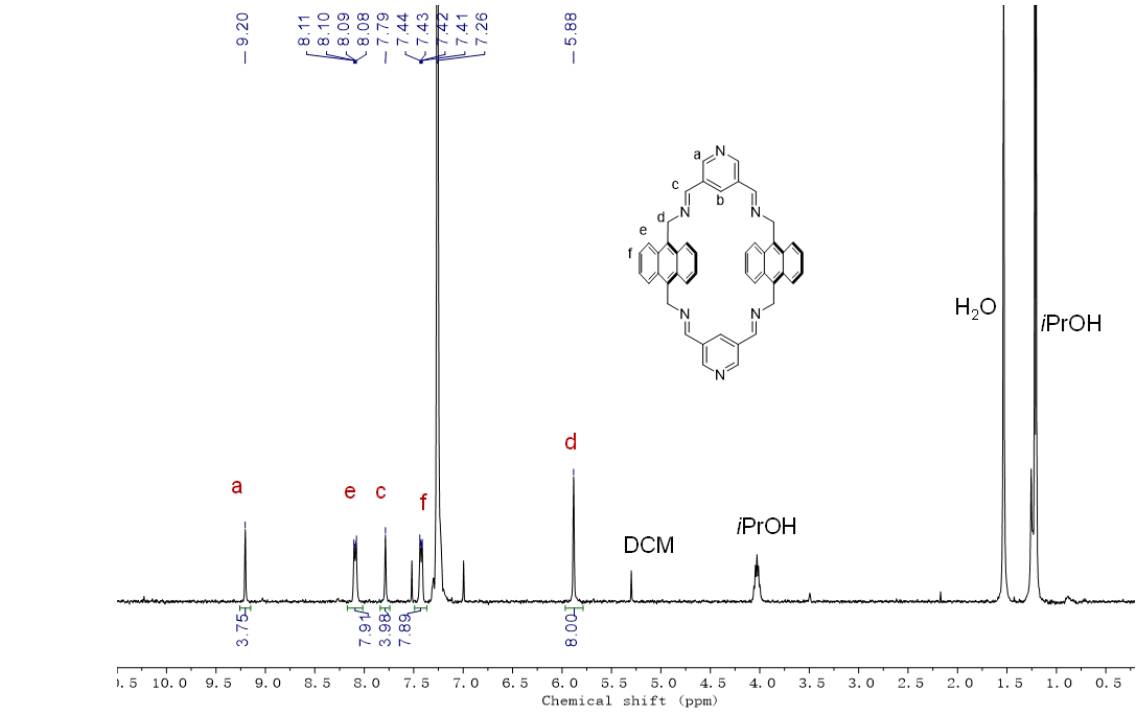

Fig. S13. ^{1}H NMR spectrum (600 MHz, $CDCl_3$, 298 K) of the imine macrocycle **5**.

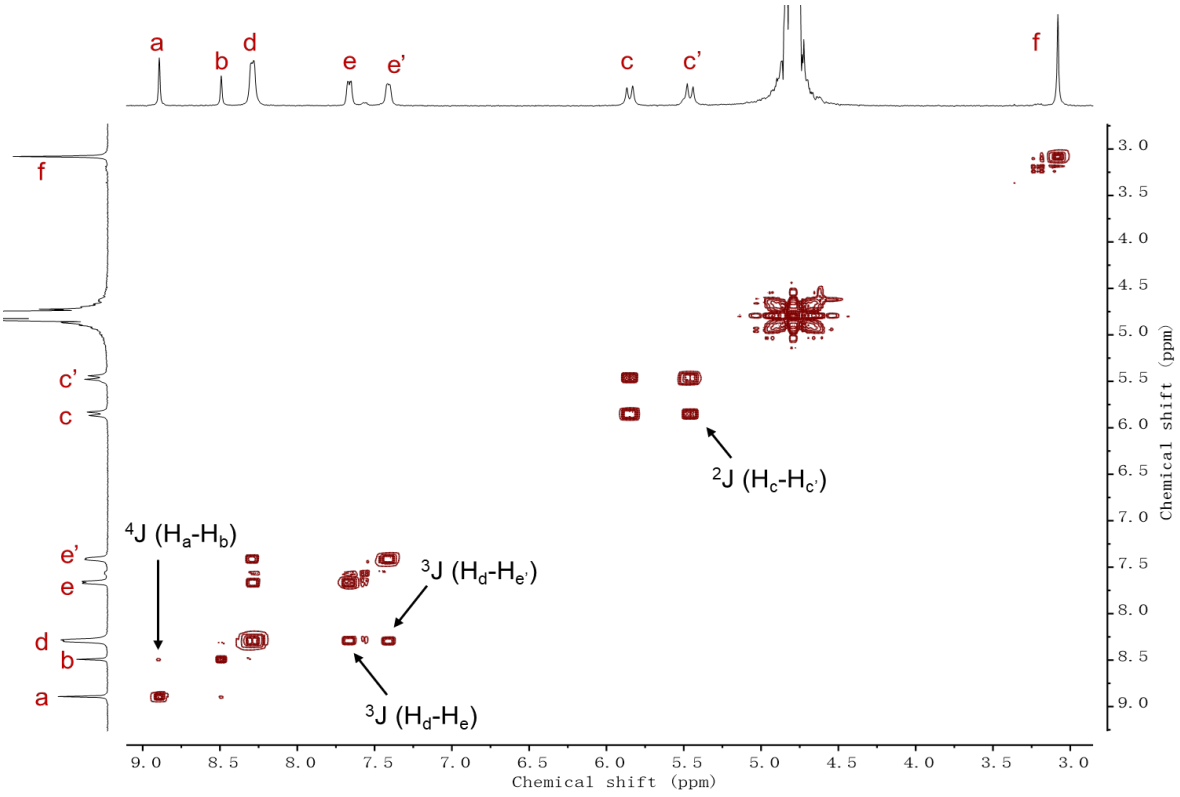

Fig. S14. Partial ^{1}H-^{1}H gCOSY NMR spectrum (400 MHz, D_2O, 298 K) of compound $BPAT^{2+}$•$2Cl^{-}$ (0.2 mM).

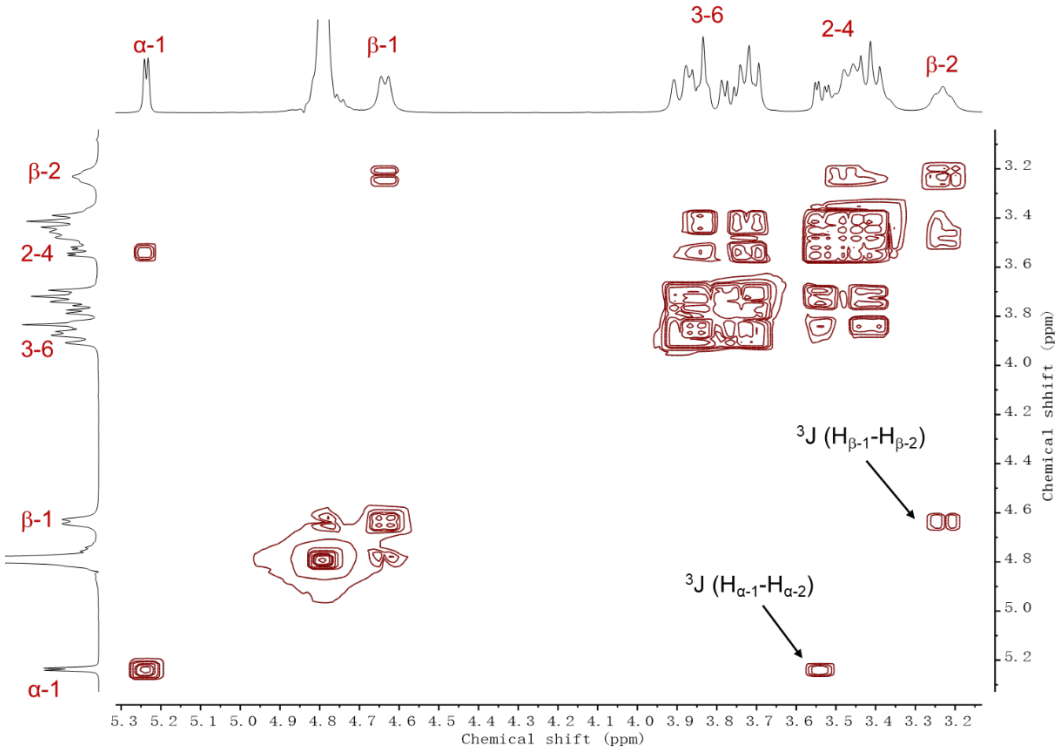

Fig. S15. Partial ^{1}H–^{1}H gCOSY NMR spectrum (400 MHz, D_2O, 298 K) of a mixture of glucose (50 mM) and $BPAT^{2+}$•2Cl^- (0.2 mM).

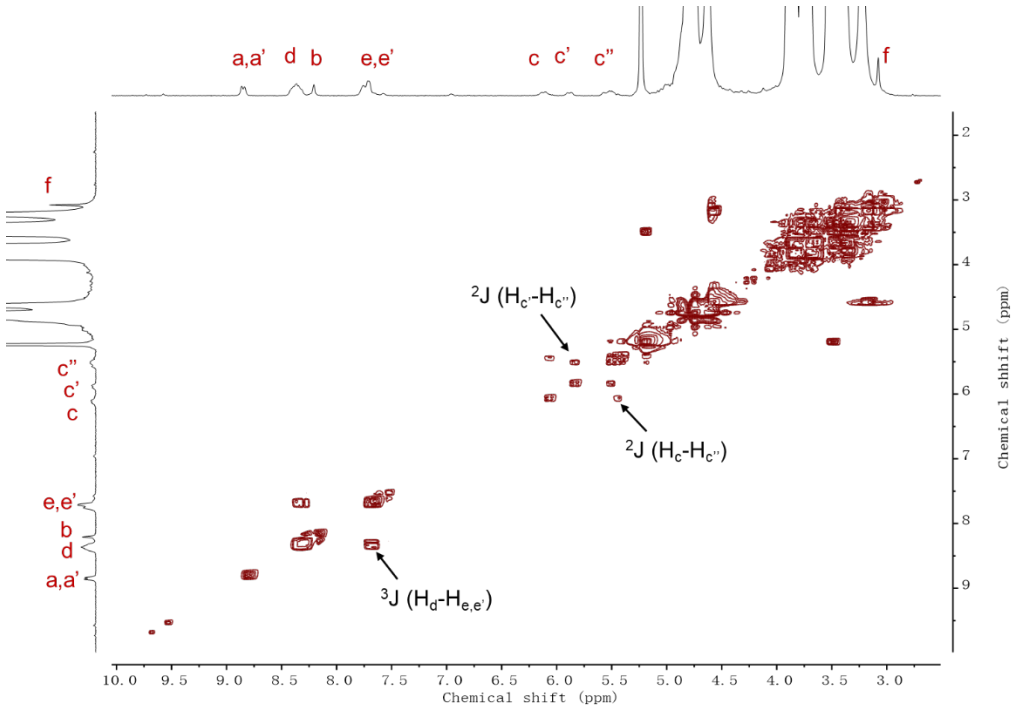

Fig. S16. Partial ^{1}H–^{1}H gCOSY NMR spectrum (400 MHz, D_2O, 298 K) of a mixture of glucose (47 mM), NaCl (20 mM), and $BPAT^{2+}$•2Cl^- (0.5 mM).

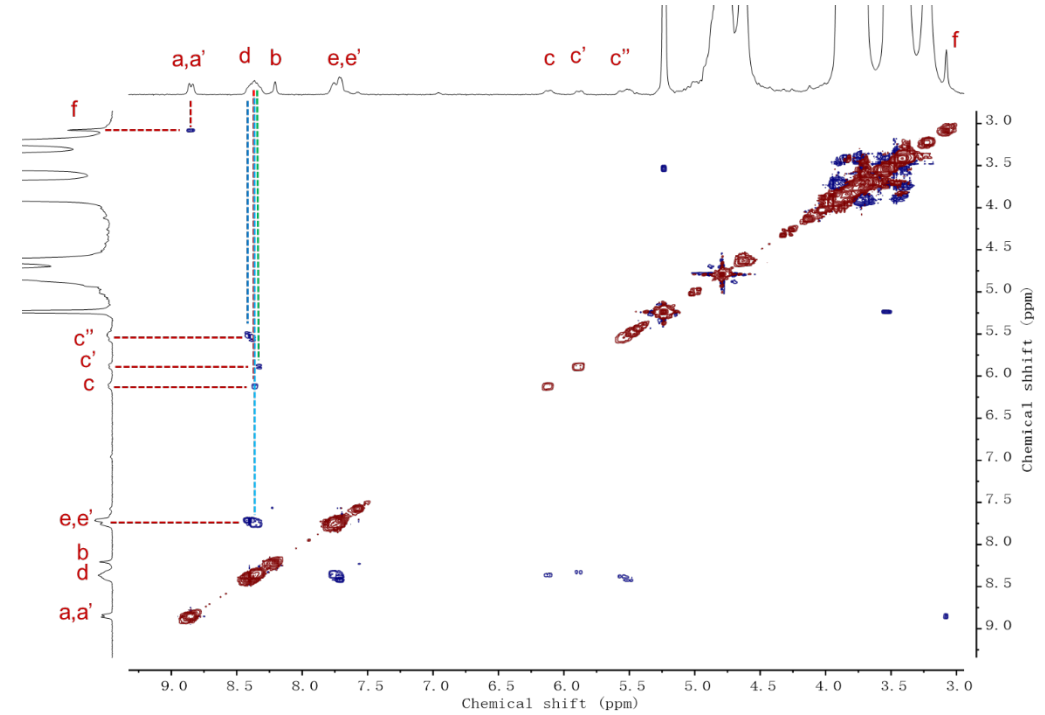

Fig. S17. Partial ^{1}H–^{1}H ROESY NMR spectrum (400 MHz, D_2O, 298 K) of a mixture of glucose (47 mM), NaCl (20 mM), and $BPAT^{2+}$•$2Cl^{-}$ (0.5 mM).

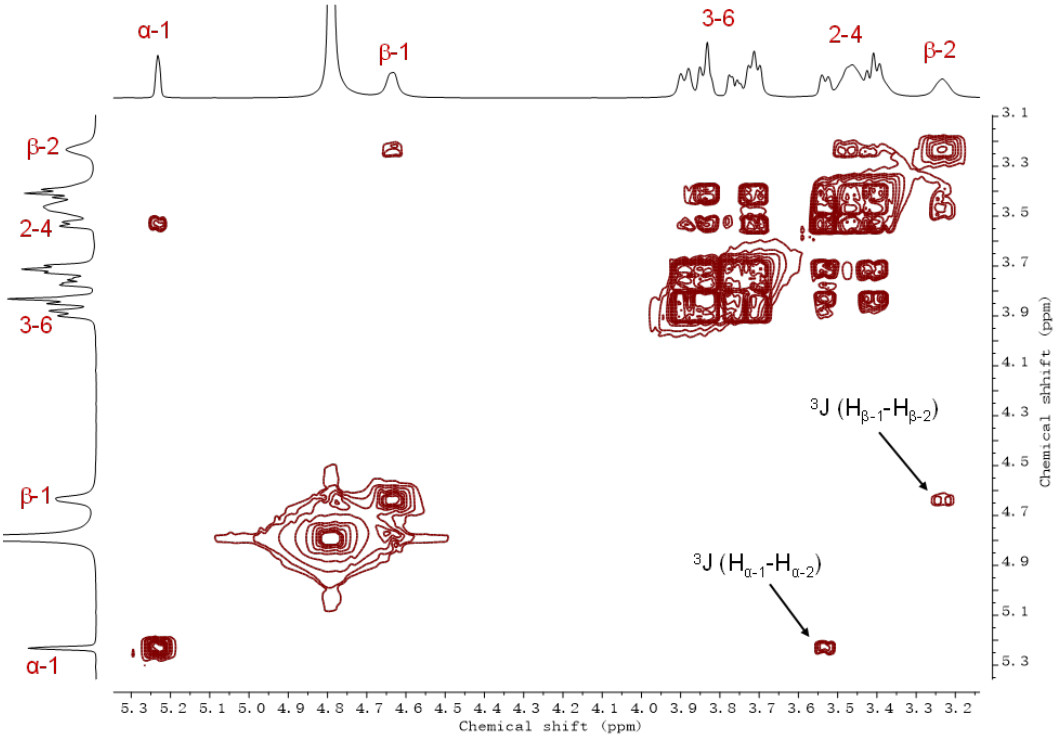

Fig. S18. Partial ^{1}H–^{1}H gCOSY NMR spectrum (600 MHz, D_2O, 298 K) of a mixture of glucose (170 mM) and $BPAT^{2+}$•$2Cl^{-}$ (0.76 mM).

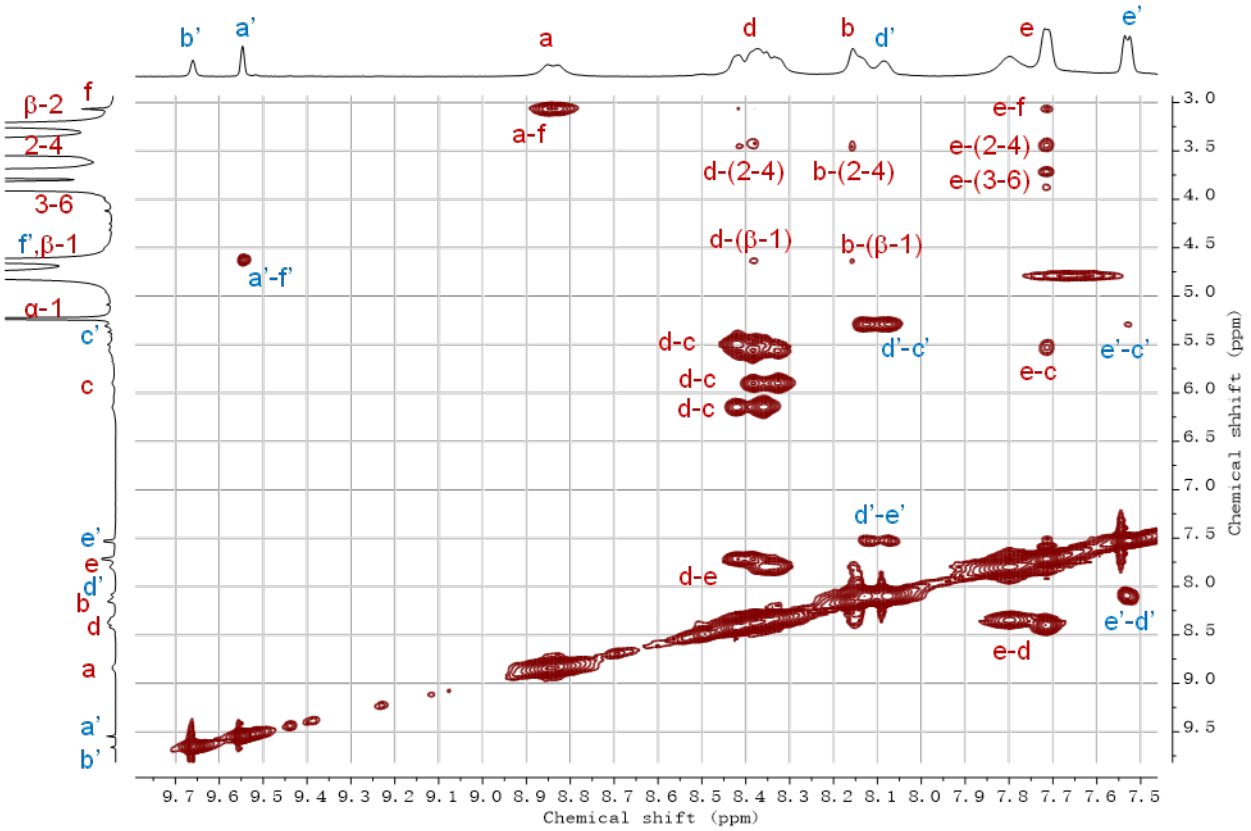

Fig. S19. Partial ^{1}H–^{1}H NOESY NMR spectrum (600 MHz, D_2O, 298 K) of a mixture of glucose (170 mM) and $BPAT^{2+}$•$2Cl^{-}$ (0.76 mM). The mixing time is set at 0.2 seconds for data acquisition.

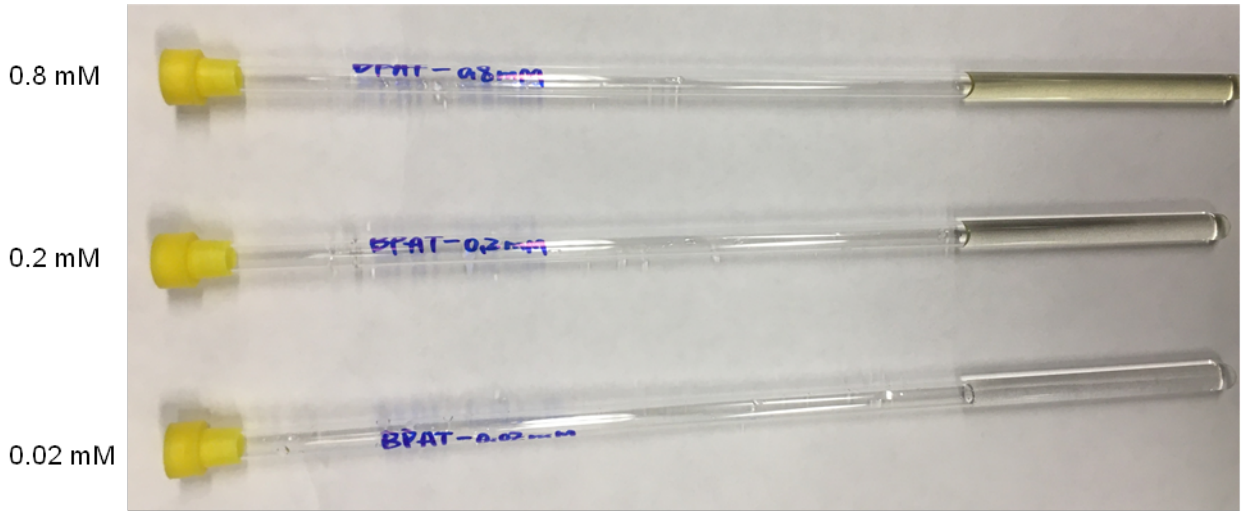

Fig. S20. A picture of $BPAT^{2+}$•$2Cl^{-}$solutions used for the DOSY experiment at different concentrations showing no sedimentation.

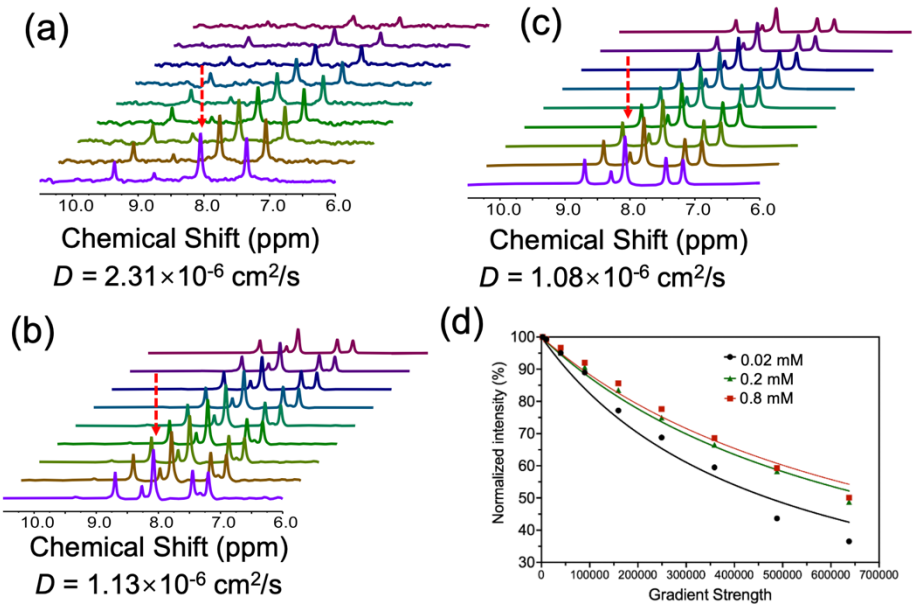

Fig. S21. DOSY NMR spectra (600 MHz, D_2O) of $BPAT^{2+}$•$2Cl^-$ at (a) 0.02 mM, (b) 0.2 mM, and (c) 0.8 mM. The change of peak intensity from proton d (indicated by the red arrow) was used to determine the diffusion coefficient (*D*). (d) Fitting of the peak intensity of proton d over the gradient strength.

Variable Temperature NMR and Thermodynamic Analysis

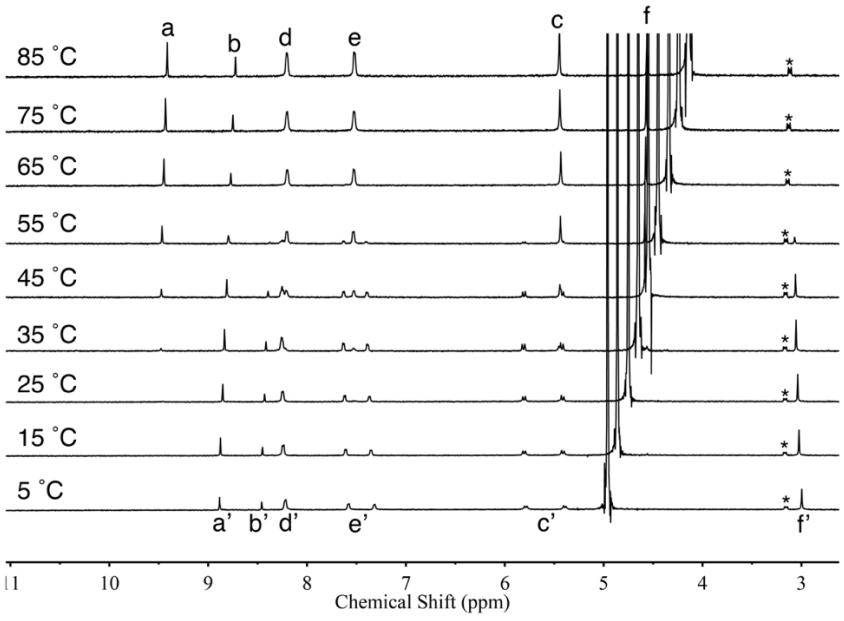

Fig. S22. Variable temperature ^1H NMR spectra (600 MHz, D_2O) of $BPAT^{2+}$•$2Cl^-$ (0.2 mM). * represents a trace amount of TBACl residue. The solvent peaks HDO were calibrated using the formula $\delta(HDO) = 7.83 - T / 96.9$, where the temperature is measured in Kelvins.

Determination of thermodynamic parameters based on VT ^{1}H NMR experiments

Considering the volume of the aggregate is eight times larger than that of the free macrocycle from the results of DOSY experiments, we arbitrarily assume that the aggregation is mainly in the form of octamer. Based on this assumption, we define the following equilibrium:

$$8\ [BPAT^{2+}\bullet 2Cl^{-}]_{free} \rightleftharpoons [BPAT^{2+}\bullet 2Cl^{-}]_{8}$$

The equilibrium constant (K) for this reaction can be expressed as the concentration of the aggregate ($[BPAT^{2+}\bullet 2Cl^{-}]_8$) divided by the concentration of free molecules ($[BPAT^{2+}\bullet 2Cl^{-}]_{free}$) raised to the power of 8:

$$K = [BPAT^{2+}\bullet 2Cl^{-}]_8 / [BPAT^{2+}\bullet 2Cl^{-}]_{free}{}^{\wedge 8}$$

We can exploit the fact that the sum of the fraction from free ($X\_[BPAT^{2+}\bullet 2Cl^{-}]_{free}$) and aggregated ($X\_[BPAT^{2+}\bullet 2Cl^{-}]_8$) states represents the total fraction of $BPAT^{2+}\bullet 2Cl^{-}$, which is always 1. Mathematically:

$$X\_[BPAT^{2+}\bullet 2Cl^{-}]_8 + X\_[BPAT^{2+}\bullet 2Cl^{-}]_{free} = 1$$

Now, the K_a equation can be expressed in the form of relative fractions of the two components:

$$K = X\_[BPAT^{2+}\bullet 2Cl^{-}]_8 / (X\_[BPAT^{2+}\bullet 2Cl^{-}]_{free})\wedge 8$$

Since the free state $[BPAT^{2+}\bullet 2Cl^{-}]_{free}$ and aggregated state $[BPAT^{2+}\bullet 2Cl^{-}]_8$ are in slow exchange at ^{1}H NMR time scale, the relative fractions of $X\_[BPAT^{2+}\bullet 2Cl^{-}]_8$ and $X\_[BPAT^{2+}\bullet 2Cl^{-}]_{free}$ can be directly measured by comparing the integrations of protons e at their state, resulting in the following data listed in Table S1.

Table S1. Equilibrium parameters derived from VT NMR experiments.

Temperature / K	Fraction $[BPAT^{2+}\bullet 2Cl^{-}]_{free}$	Fraction of $[BPAT^{2+}\bullet 2Cl^{-}]_8$	ln$K$
308	0.175	0.825	13.8
318	0.39	0.61	7.1
328	0.77	0.23	0.6

The obtained ln$K$ value was plotted against 1/T, and the resulting plots were fitting based on the Van't Hoff equation to yield the corresponding enthalpy and entropy associated with this aggregation process:

$$\ln K = -\frac{1}{T}\frac{\Delta H}{R} + \frac{\Delta S}{R}$$

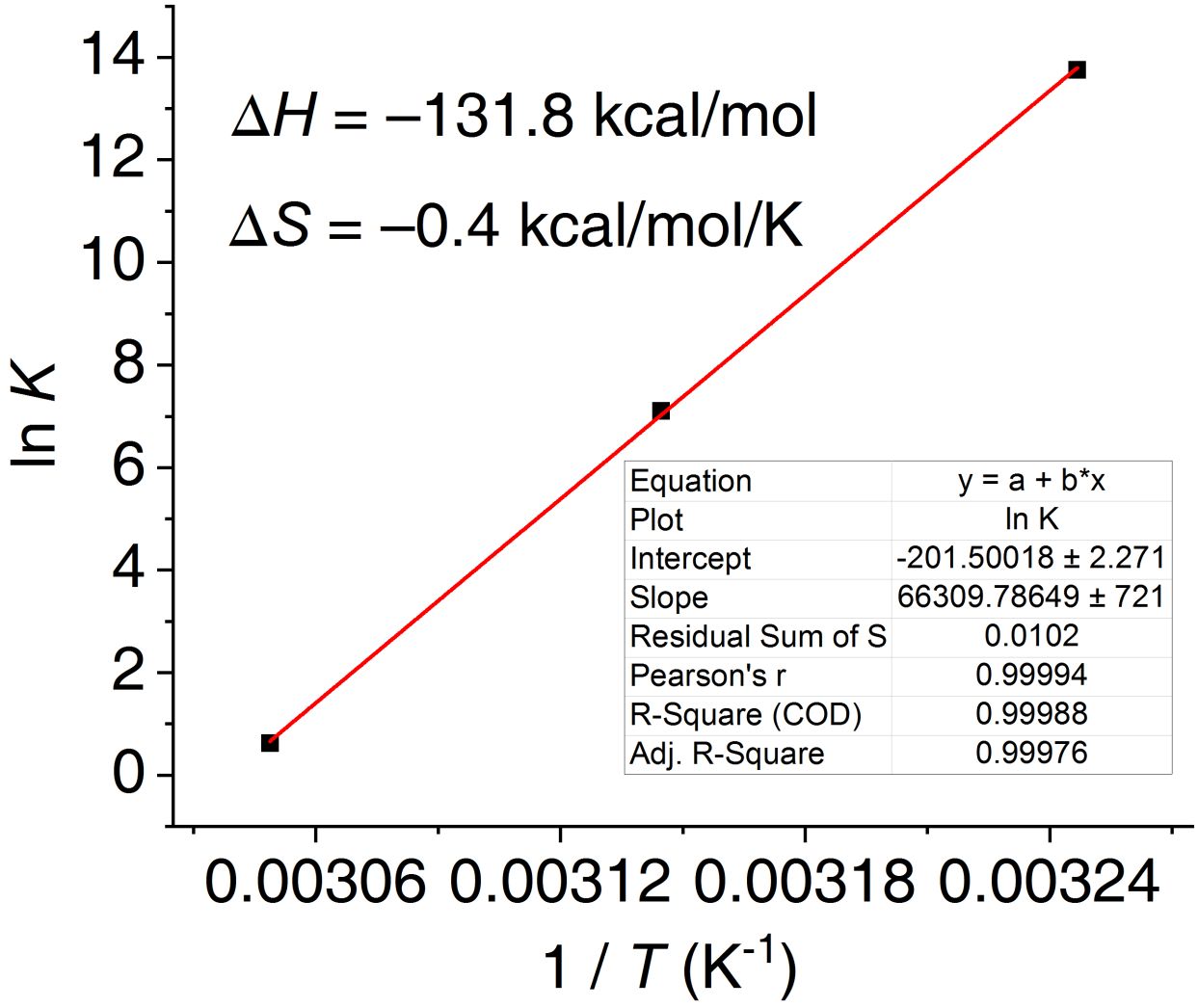

Fig. S23. Van't Hoff plot of the aggregation process of $BPAT^{2+}$•$2Cl^-$ at 308, 318, and 328 K.

Discussion of Van't Hoff plot analysis

Thermodynamic analysis from the Van't Hoff plot reveals an enthalpy change (ΔH) of –131.8 kcal/mol and an entropy change (ΔS) of –0.4 kcal/mol/K for the aggregation process. These parameters suggest that the aggregation is driven by favorable enthalpy but is offset by a significant entropy penalty. This behavior indicates that the hydrophobic effect from the stacking of

anthracene panels, typically associated with an entropic benefit, cannot solely explain the aggregation mechanism. Instead, the electrostatic interactions between chloride ions and the macrocycles are essential for this distinct aggregation mechanism. The pronounced entropy penalty implies a considerable restriction in the macrocycle's translational and conformational freedom of motion in the aggregated state. As temperature rises, particularly from 35˚C to 65˚C, the entropic penalty starts to dominate over enthalpic contributions, shifting the Gibbs free energy (ΔG) from –8.6 kcal/mol to +3.4 kcal/mol and thus leading to dissociation. This observation also provides insight into why larger aggregates are not observed at higher concentrations, which would incur even more significant entropy penalties, making further aggregation thermodynamically unfavorable.

Sugar Binding Analysis Using ^{1}H NMR Titration.

^{1}H NMR titrations in D_2O were conducted at 298 K on a Varian Unity Inova 400 MHz system equipped with a cryoprobe. All samples were equilibrated for 24 hours before use. Aliquots from a stock solution containing the corresponding carbohydrate were added sequentially to an NMR tube containing the solution of $BPAT^{2+}\bullet 2Cl^-$ (600 μL). The concentration of $BPAT^{2+}\bullet 2Cl^-$ was calibrated using imidazole as an external standard by comparing their relative integrations. The ^{1}H NMR spectrum was acquired after each addition. The ^{1}H NMR titration spectra were analyzed using MestReNova software. The NMR titration isotherms were fitted[S1,S2] to a 1:1 host-guest binding model using Thordarson's equations at http://app.supramolecular.org/bindfit/. The data were then plotted using OriginLab software. The binding constants K_a were presented with standard deviations from the fitting outcomes.

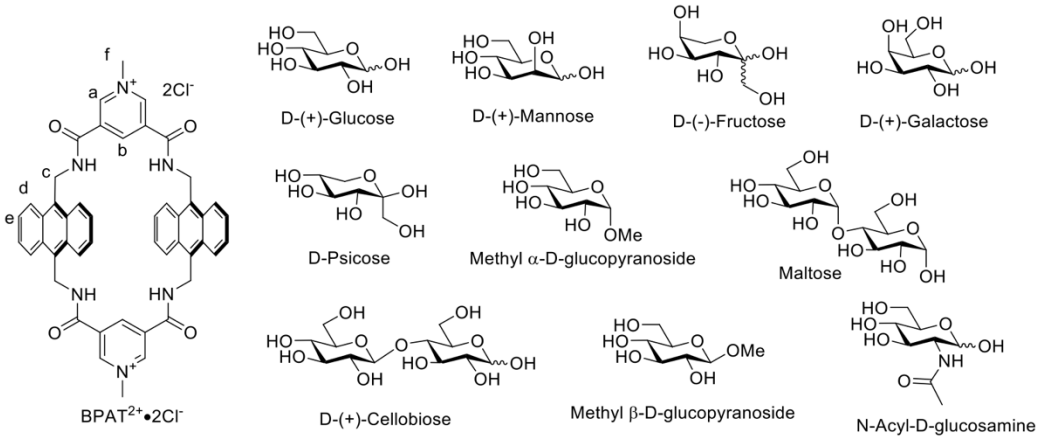

Fig. S24. Structures of $BPAT^{2+}\bullet 2Cl^-$ and different carbohydrate substrates.

Sugar binding of $BPAT^{2+}$•$2Cl^-$ in the free state

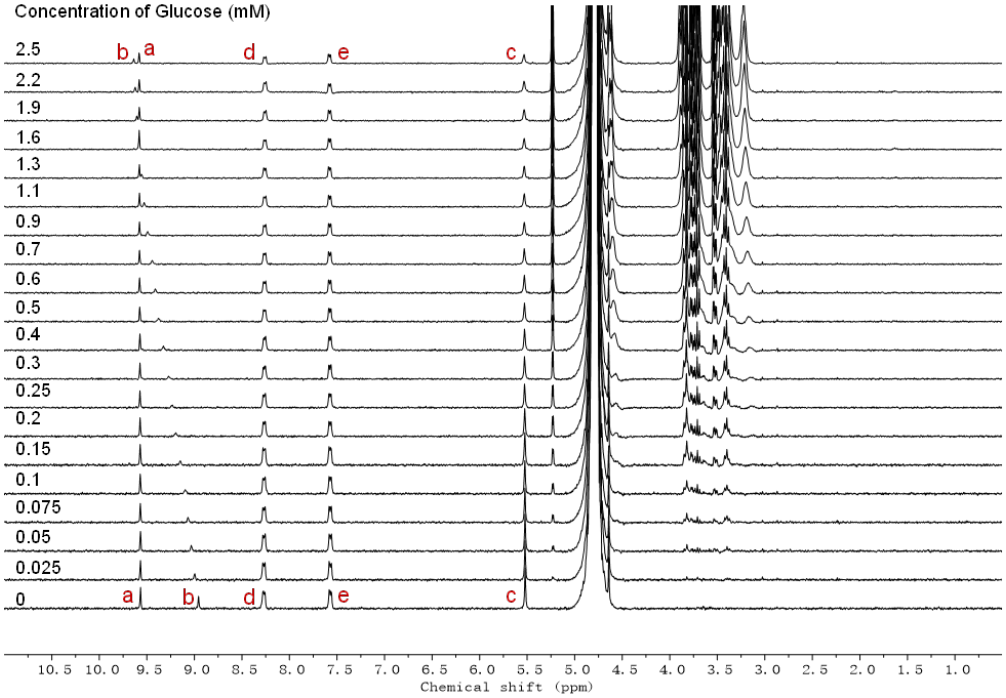

Fig. S25. Full ^1H NMR spectra (400 MHz, D_2O, 298 K) of $BPAT^{2+}$•$2Cl^-$ (0.017 mM) titrated with glucose.

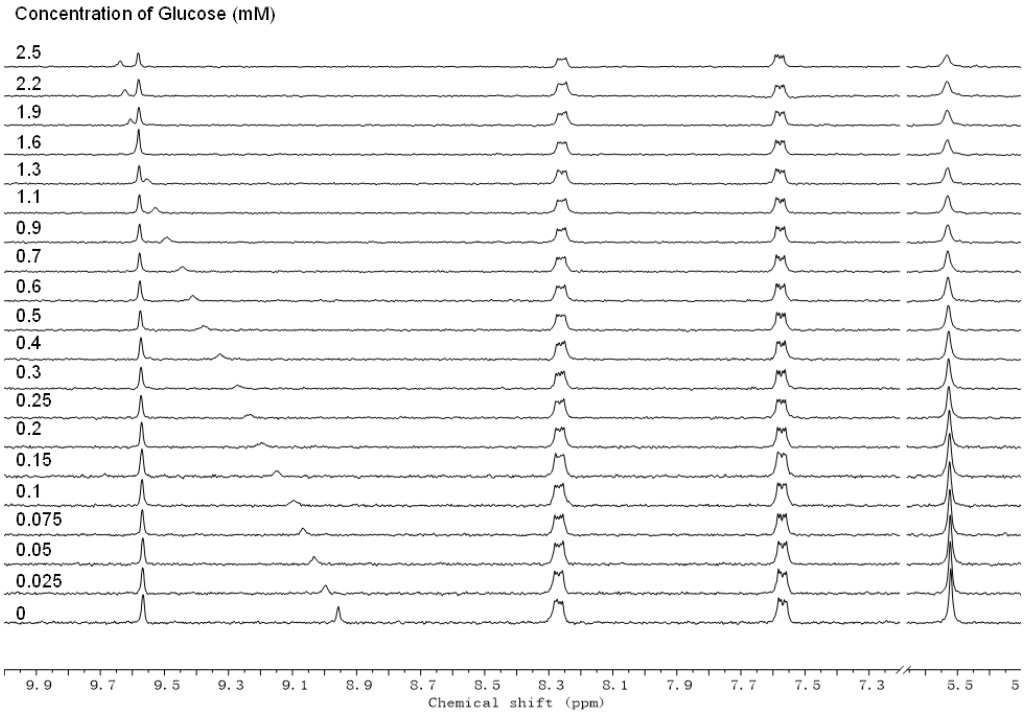

Fig. S26. Partial ^1H NMR spectra (400 MHz, D_2O, 298 K) of $BPAT^{2+}$•$2Cl^-$ (0.017 mM) titrated with glucose showing the change of $BPAT^{2+}$•$2Cl^-$ showing the change of chemical shifts of $BPAT^{2+}$•$2Cl^-$.

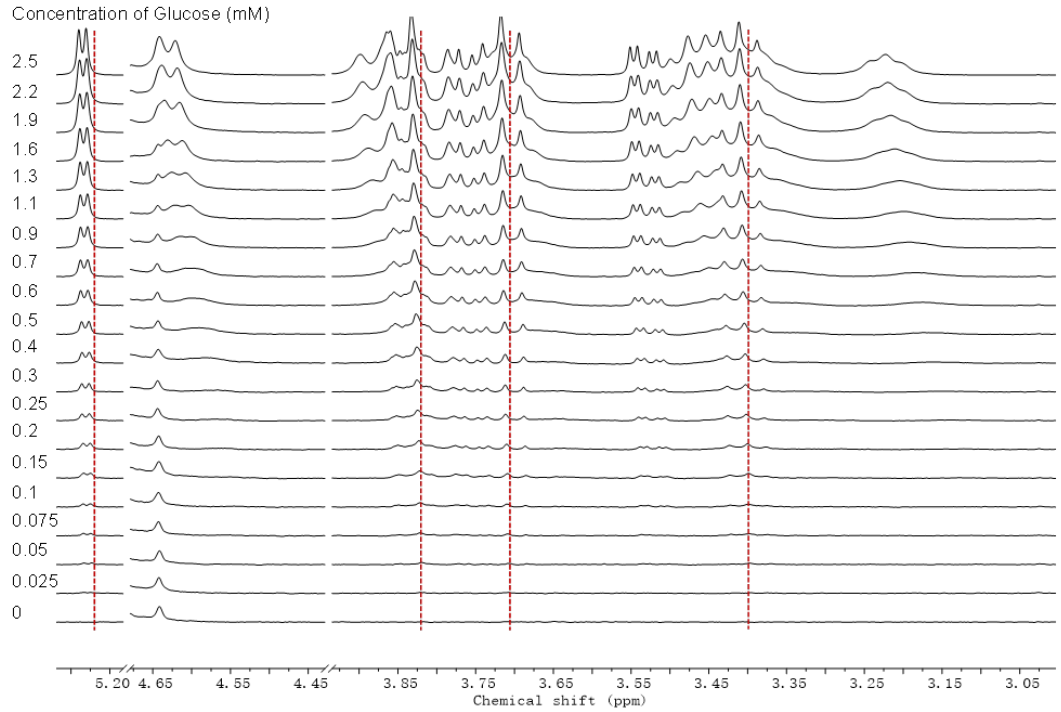

Fig. S27. Partial ^{1}H NMR spectra (400 MHz, D_2O, 298 K) of $BPAT^{2+}$•$2Cl^-$ (0.017 mM) titrated with glucose showing the change of chemical shifts of glucose.

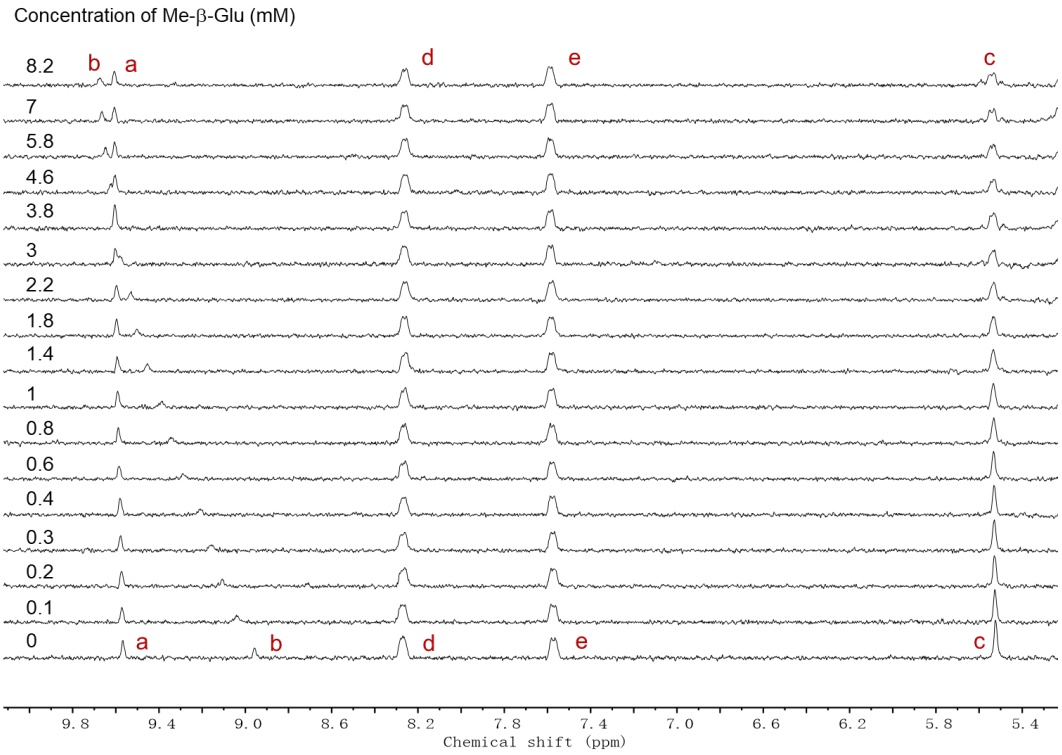

Fig. S28. Partial ^{1}H NMR spectra (400 MHz, D_2O, 298 K) of $BPAT^{2+}$•$2Cl^-$ (0.017 mM) titrated with Me-β-glucoside.

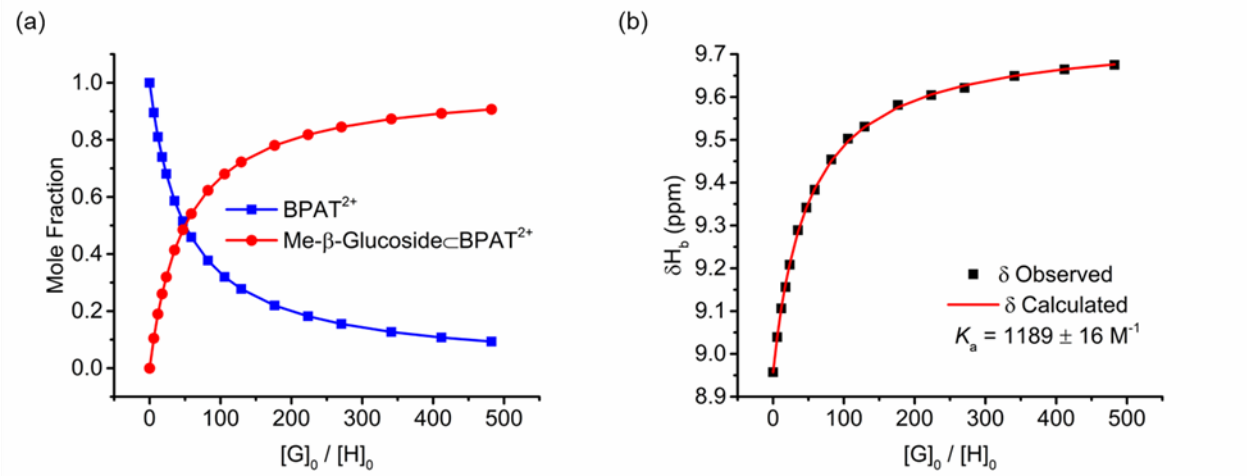

Fig. S29. (a) Calculated changes of mole fractions for $BPAT^{2+}$•$2Cl^{-}$ (blue trace) and Me-β-glucoside⊂ $BPAT^{2+}$•$2Cl^{-}$ (red trace) over the guest-host mole ratio. (b) Titration isotherm created by monitoring changes in the chemical shift of proton b for $BPAT^{2+}$•$2Cl^{-}$ (0.017 mM) caused by the addition of Me-β-glucoside in D_2O at 298 K. Red lines are the curve fitting using a 1:1 host-guest binding model.

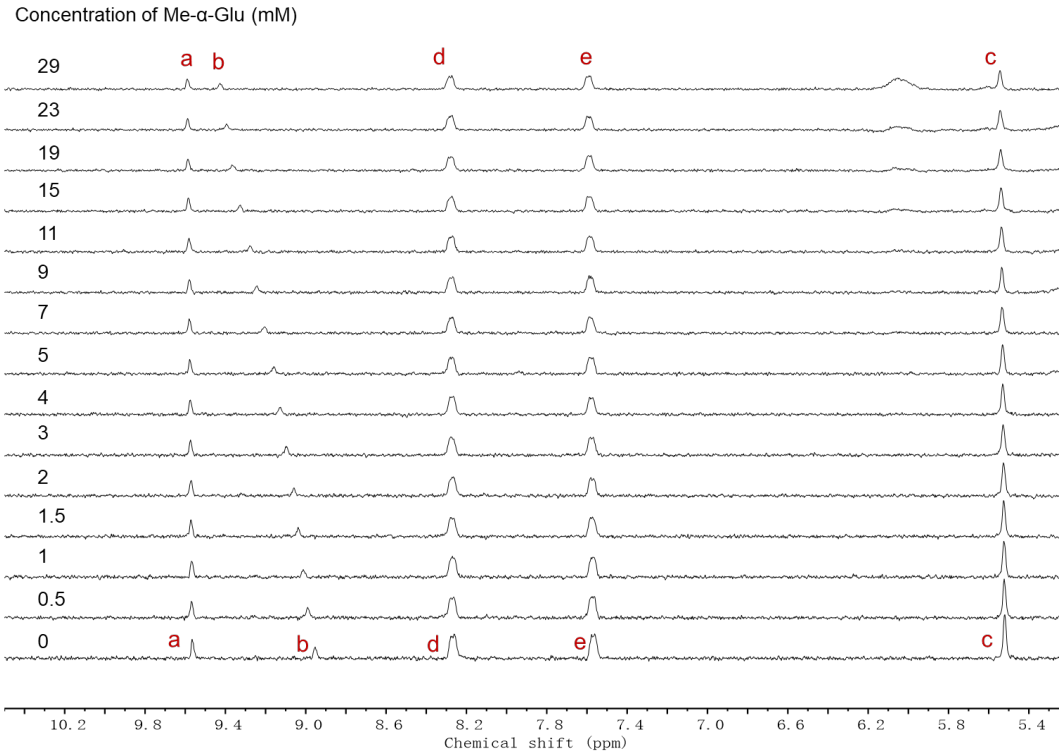

Fig. S30. Partial ^{1}H NMR spectra (400 MHz, D_2O, 298 K) of $BPAT^{2+}$•$2Cl^{-}$ (0.017 mM) titrated with Me-α-glucoside.

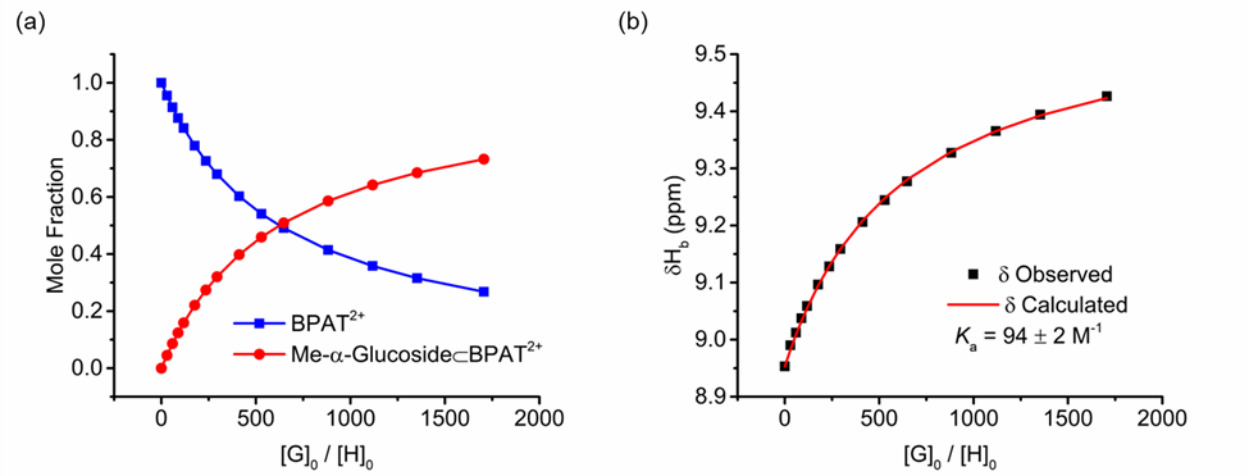

Fig. S31. (a) Calculated changes of mole fractions for $BPAT^{2+}$•$2Cl^-$ (blue trace) and Me-α-glucoside⊂ $BPAT^{2+}$•$2Cl^-$ (red trace) over the guest-host mole ratio. (b) Titration isotherm created by monitoring changes in the chemical shift of proton b for $BPAT^{2+}$•$2Cl^-$ (0.017 mM) caused by the addition of Me-α-glucoside in D_2O at 298 K. Red lines are the curve fitting using a 1:1 host-guest binding model.

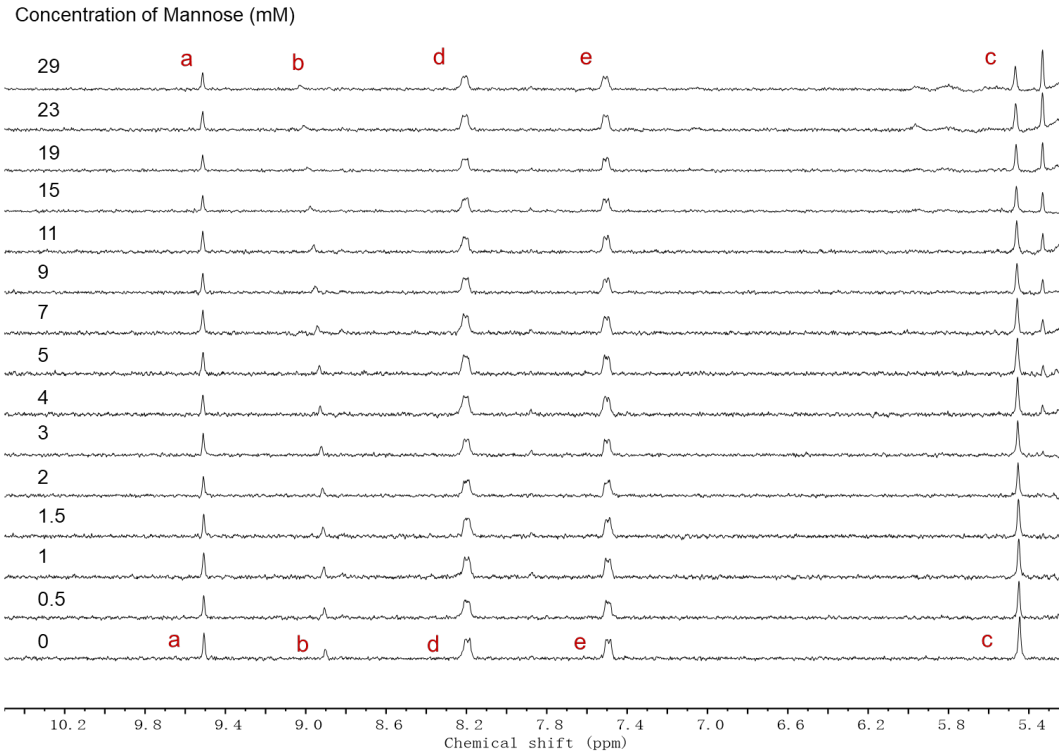

Fig. S32. Partial ^1H NMR spectra (400 MHz, D_2O, 298 K) of $BPAT^{2+}$•$2Cl^-$ (0.017 mM) titrated with mannose.

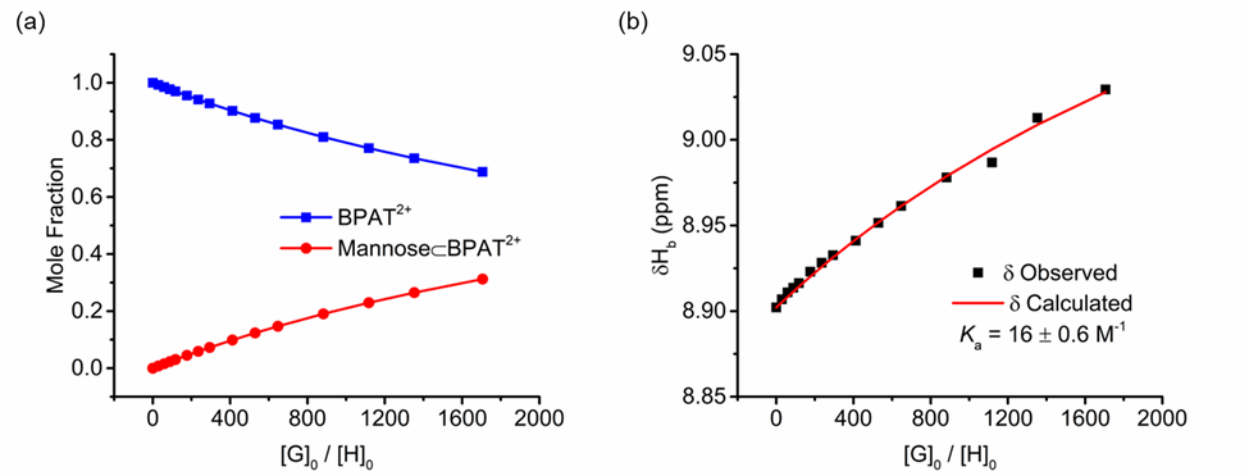

Fig. S33. (a) Calculated changes of mole fractions for $BPAT^{2+}$•$2Cl^-$ (blue trace) and mannose⊂ $BPAT^{2+}$•$2Cl^-$ (red trace) over the guest-host mole ratio. (b) Titration isotherm created by monitoring changes in the chemical shift of proton b for $BPAT^{2+}$•$2Cl^-$ (0.017 mM) caused by the addition of mannose in D_2O at 298 K. Red lines are the curve fitting using a 1:1 host-guest binding model.

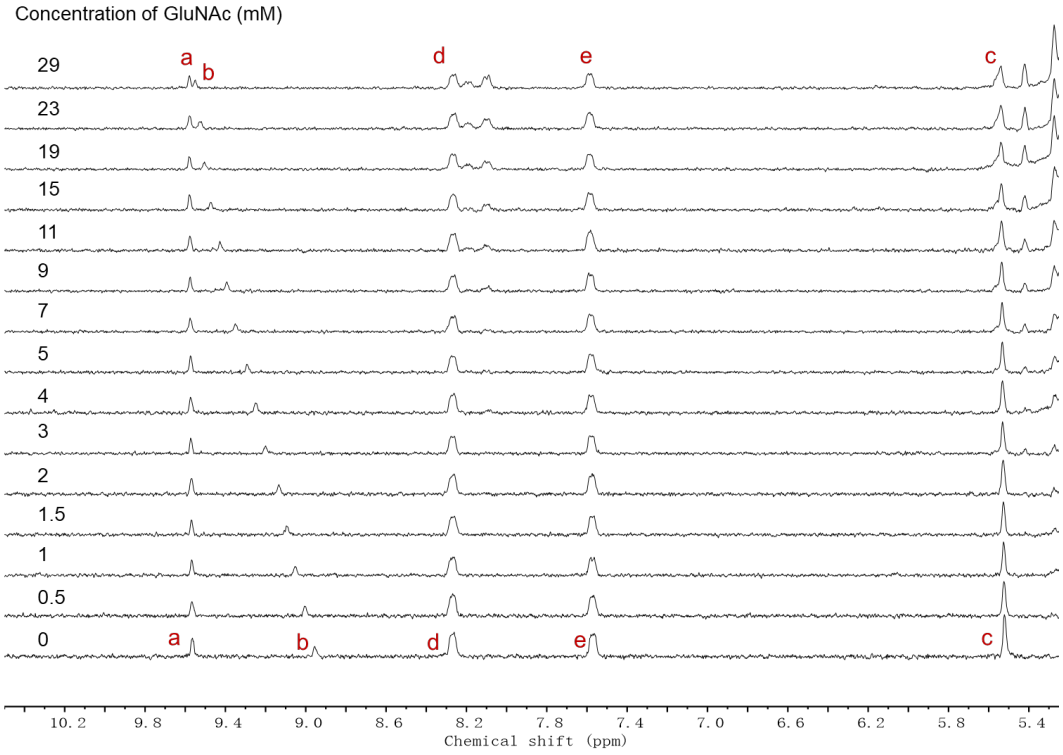

Fig. S34. Partial ^1H NMR spectra (400 MHz, D_2O, 298 K) of $BPAT^{2+}$•$2Cl^-$ (0.017 mM) titrated with GluNAc.

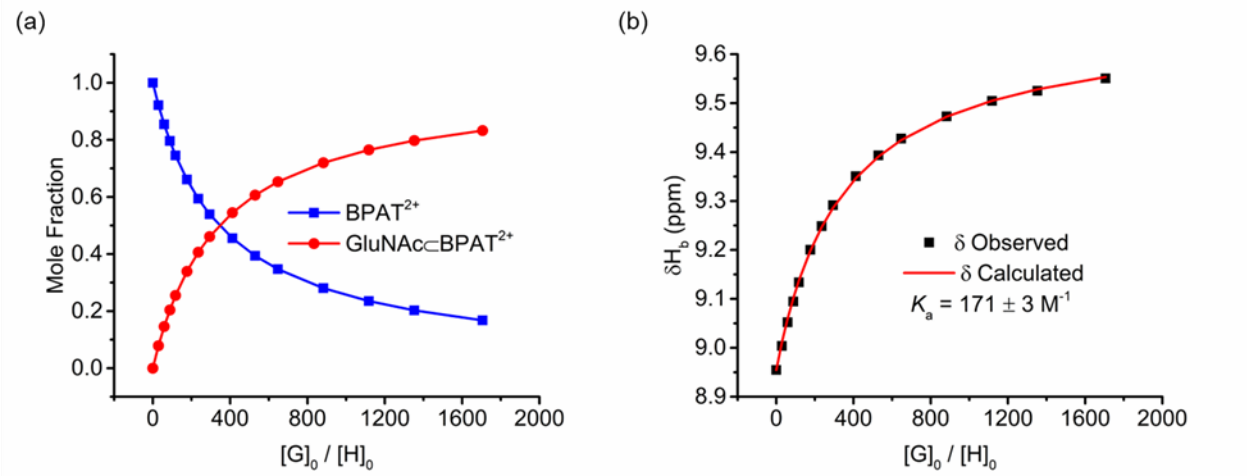

Fig. S35. (a) Calculated changes of mole fractions for $BPAT^{2+}$•$2Cl^-$ (blue trace) and GluNAc⊂ $BPAT^{2+}$•$2Cl^-$ (red trace) over the guest-host mole ratio. (b) Titration isotherm created by monitoring changes in the chemical shift of proton b for $BPAT^{2+}$•$2Cl^-$ (0.017 mM) caused by the addition of GluNAc in D_2O at 298 K. Red lines are the curve fitting using a 1:1 host-guest binding model.

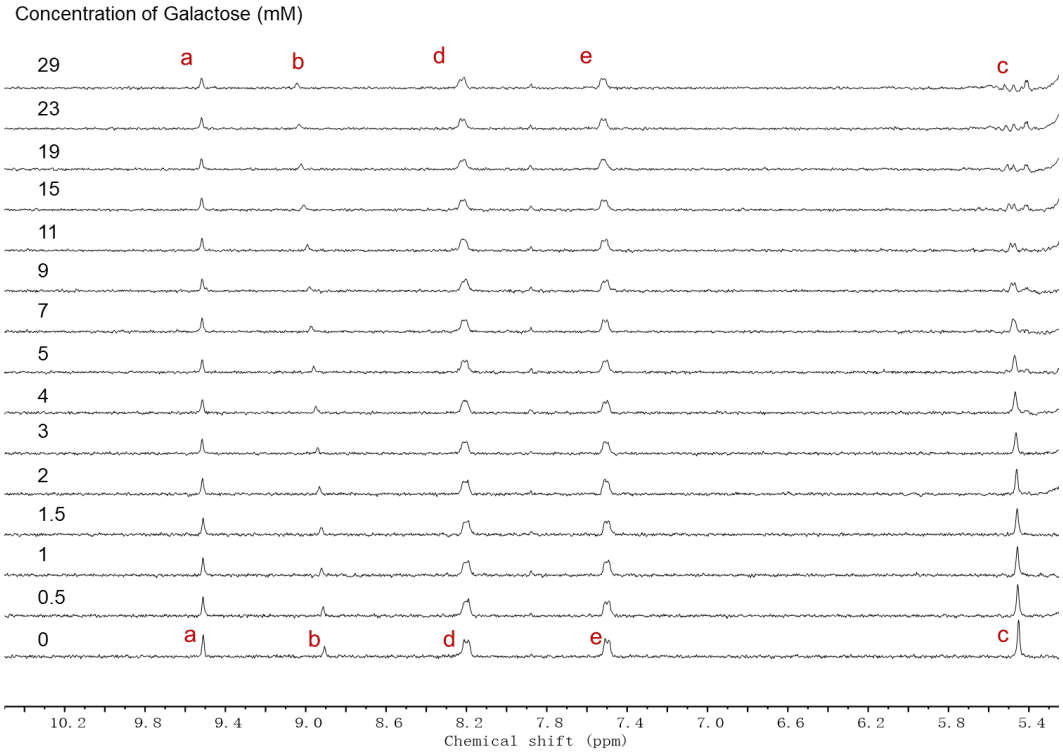

Fig. S36. Partial ^1H NMR spectra (400 MHz, D_2O, 298 K) of $BPAT^{2+}$•$2Cl^-$ (0.017 mM) titrated with galactose.

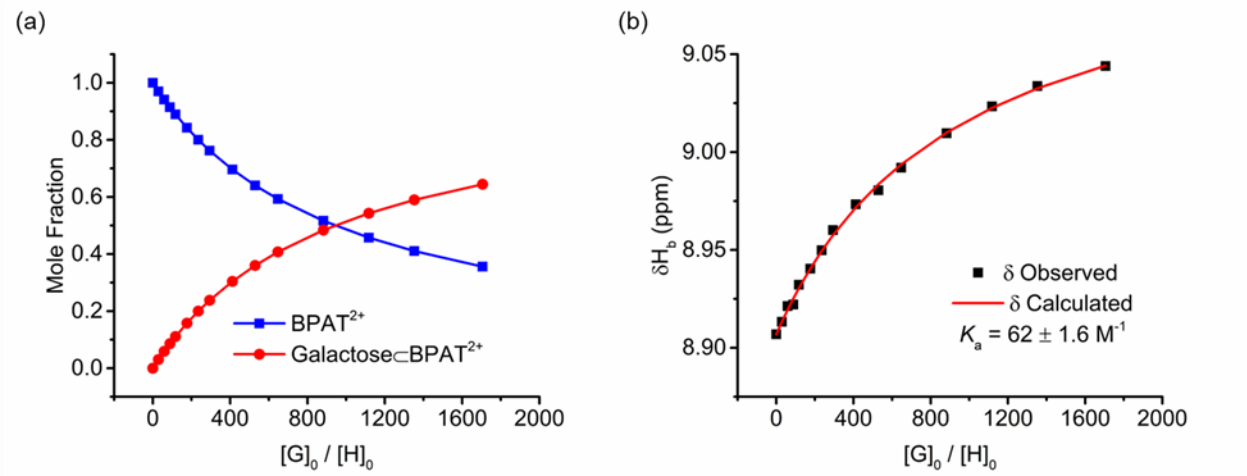

Fig. S37. (a) Calculated changes of mole fractions for $BPAT^{2+}$•$2Cl^-$ (blue trace) and galactose⊂ $BPAT^{2+}$•$2Cl^-$ (red trace) over the guest-host mole ratio. (b) Titration isotherm created by monitoring changes in the chemical shift of proton b for $BPAT^{2+}$•$2Cl^-$ (0.017 mM) caused by the addition of galactose in D_2O at 298 K. Red lines are the curve fitting using a 1:1 host-guest binding model.

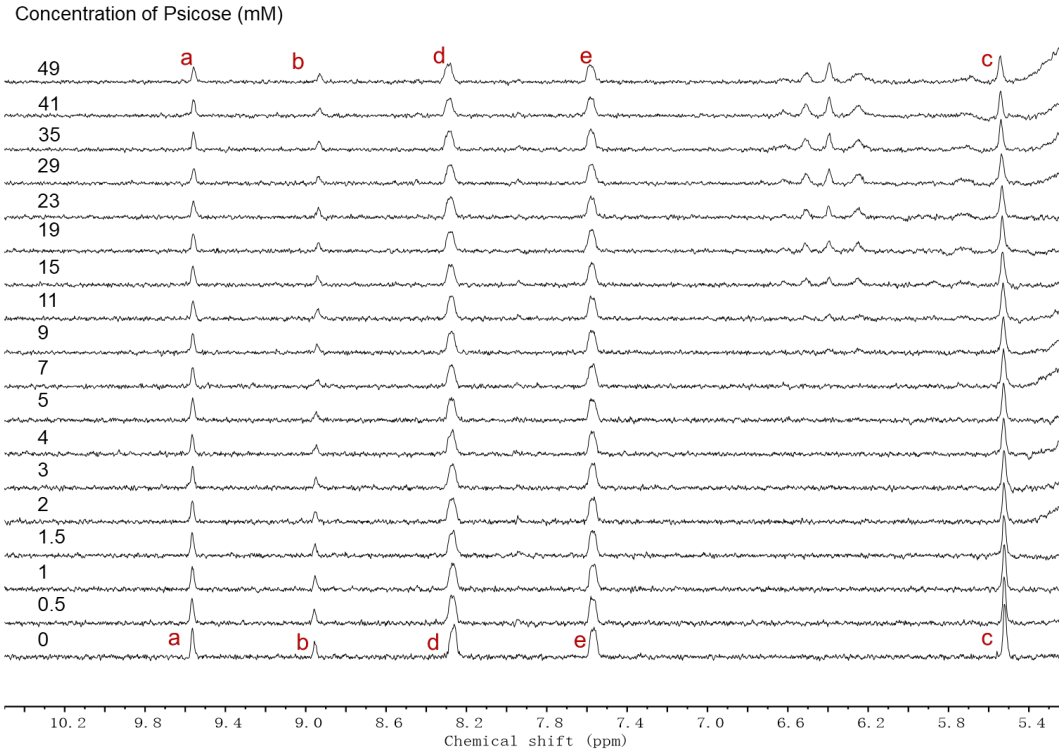

Fig. S38. Partial ^1H NMR spectra (400 MHz, D_2O, 298 K) of $BPAT^{2+}$•$2Cl^-$ (0.017 mM) titrated with psicose.

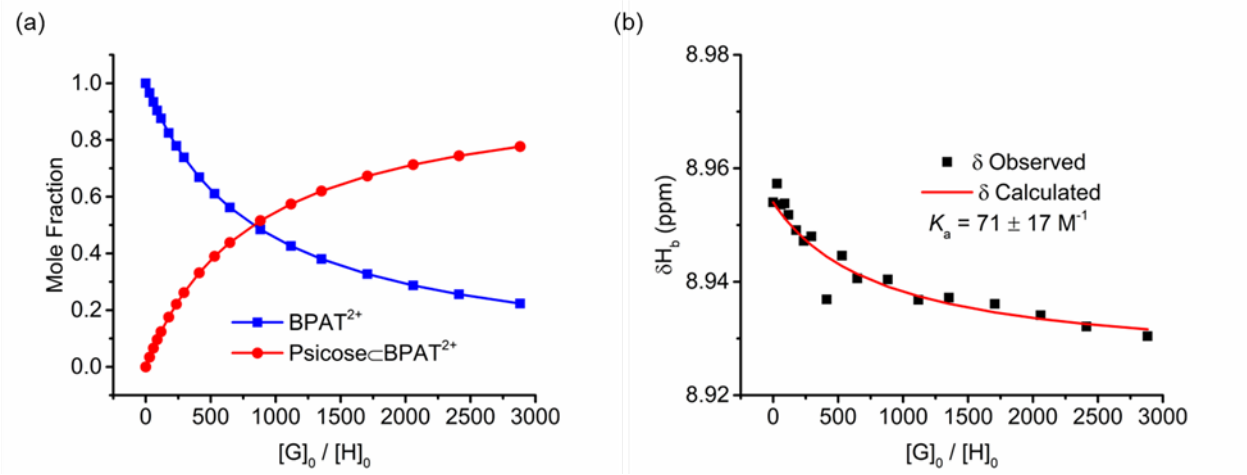

Fig. S39. (a) Calculated changes of mole fractions for $BPAT^{2+}$•$2Cl^-$ (blue trace) and psicose⊂ $BPAT^{2+}$•$2Cl^-$ (red trace) over the guest-host mole ratio. (b) Titration isotherm created by monitoring changes in the chemical shift of proton b for $BPAT^{2+}$•$2Cl^-$ (0.017 mM) caused by the addition of psicose in D_2O at 298 K. Red lines are the curve fitting using a 1:1 host-guest binding model.

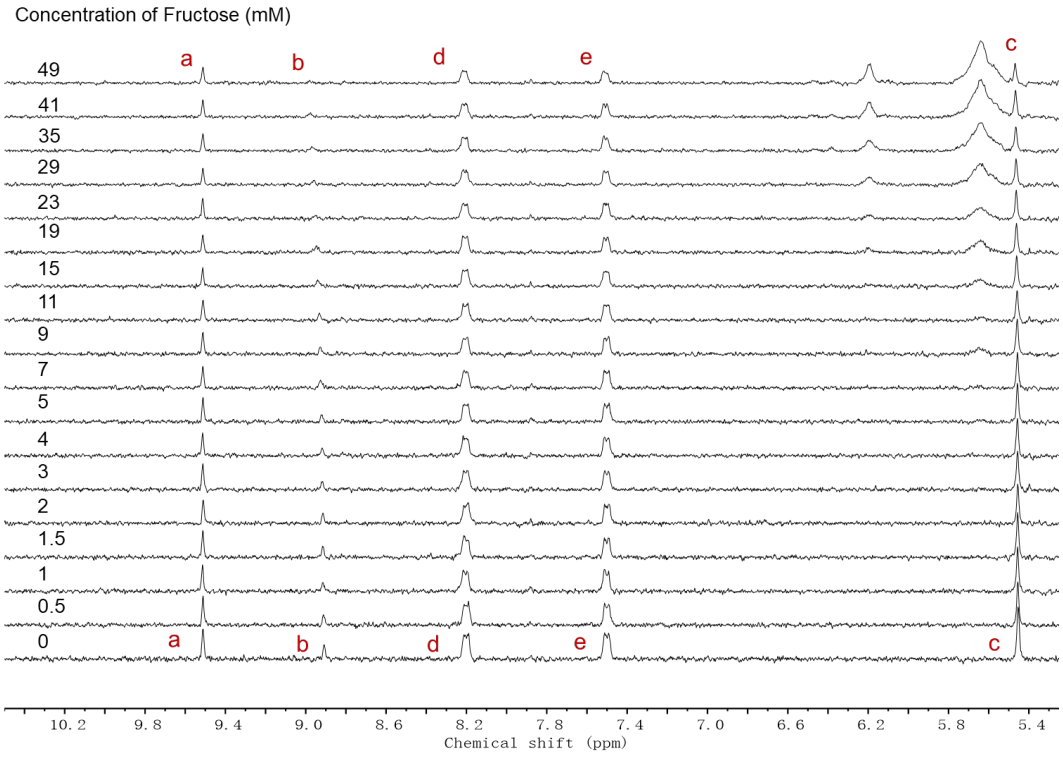

Fig. S40. Partial ^1H NMR spectra (400 MHz, D_2O, 298 K) of $BPAT^{2+}$•$2Cl^-$ (0.017 mM) titrated with fructose.

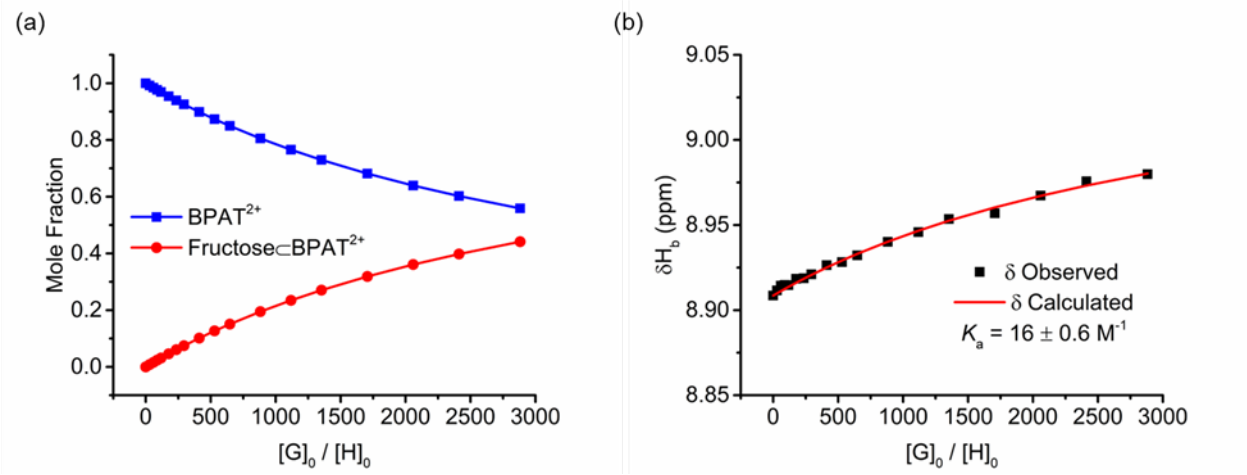

Fig. S41. (a) Calculated changes of mole fractions for $BPAT^{2+}$•$2Cl^-$ (blue trace) and fructose⊂ $BPAT^{2+}$•$2Cl^-$ (red trace) over the guest-host mole ratio. (b) Titration isotherm created by monitoring changes in the chemical shift of proton b for $BPAT^{2+}$•$2Cl^-$ (0.017 mM) caused by the addition of fructose in D_2O at 298 K. Red lines are the curve fitting using a 1:1 host-guest binding model.

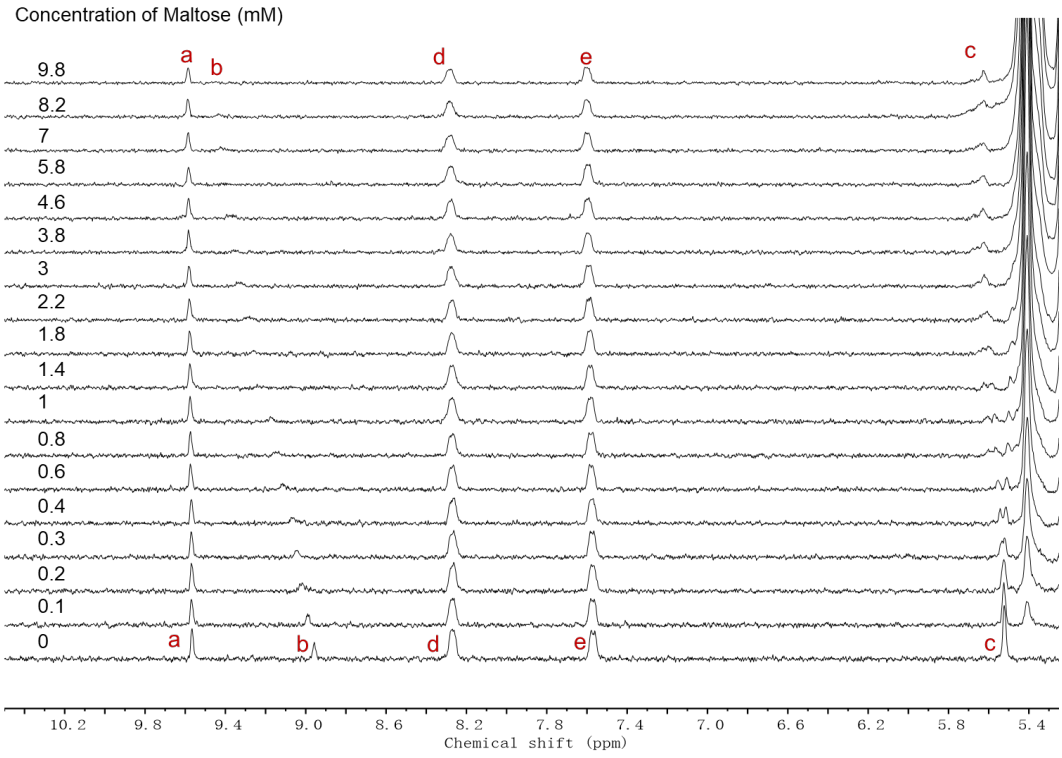

Fig. S42. Partial ^1H NMR spectra (400 MHz, D_2O, 298 K) of $BPAT^{2+}$•$2Cl^-$ (0.017 mM) titrated with maltose.

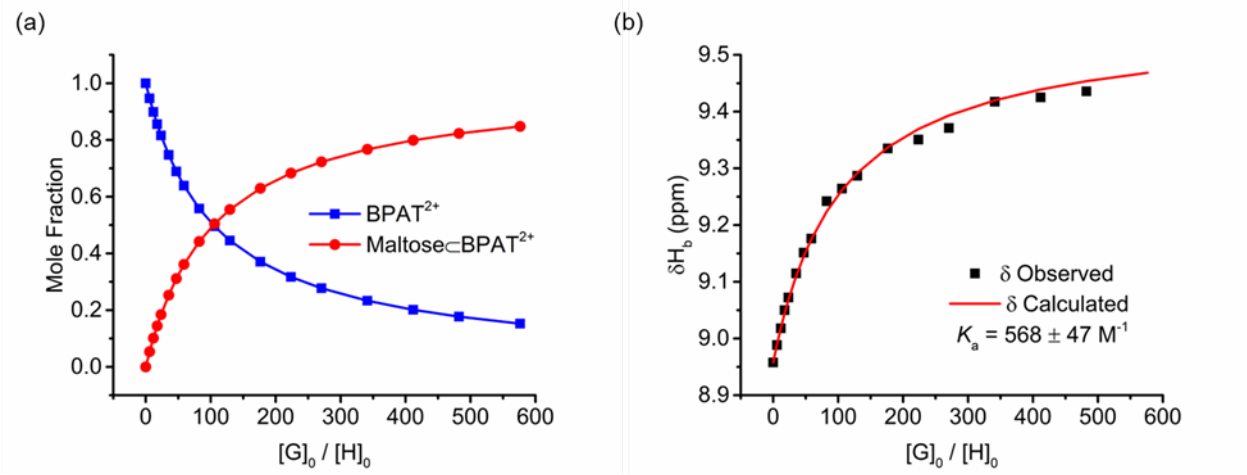

Fig. S43. (a) Calculated changes of mole fractions for $BPAT^{2+}$•$2Cl^-$ (blue trace) and maltose⊂ $BPAT^{2+}$•$2Cl^-$ (red trace) over the guest-host mole ratio. (b) Titration isotherm created by monitoring changes in the chemical shift of proton b for $BPAT^{2+}$•$2Cl^-$ (0.017 mM) caused by the addition of maltose in D_2O at 298 K. Red lines are the curve fitting using a 1:1 host-guest binding model.

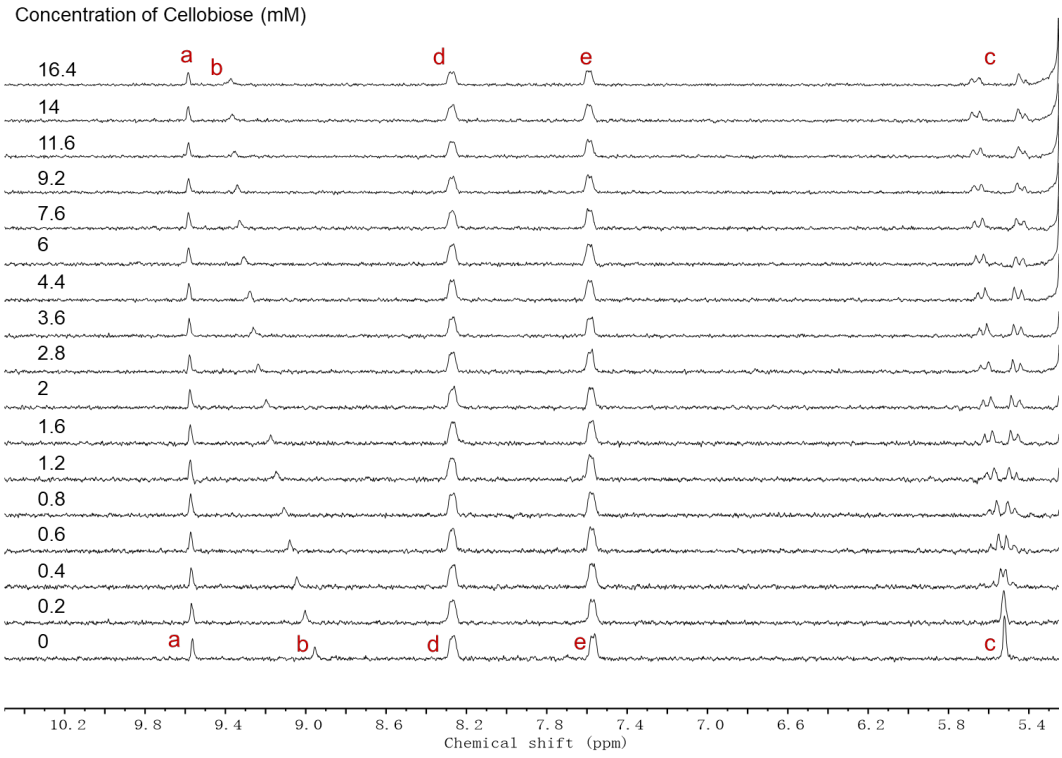

Fig. S44. Partial ^1H NMR spectra (400 MHz, D_2O, 298 K) of $BPAT^{2+}$•$2Cl^-$ (0.017 mM) titrated with cellobiose.

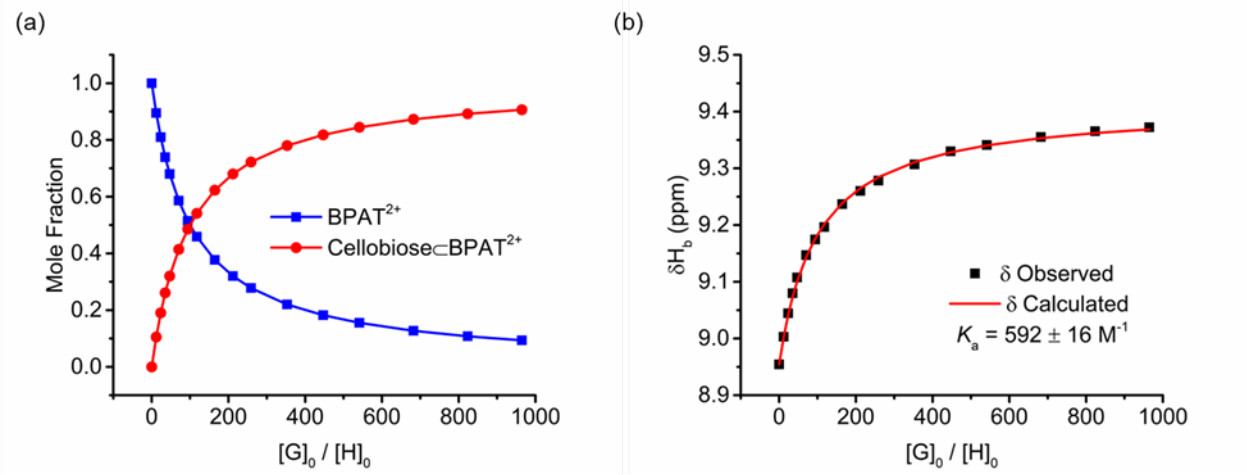

Fig. S45. (a) Calculated changes of mole fractions for $BPAT^{2+}$•$2Cl^-$ (blue trace) and cellobiose⊂ $BPAT^{2+}$•$2Cl^-$ (red trace) over the guest-host mole ratio. (b) Titration isotherm created by monitoring changes in the chemical shift of proton b for $BPAT^{2+}$•$2Cl^-$ (0.017 mM) caused by the addition of cellobiose in D_2O at 298 K. Red lines are the curve fitting using a 1:1 host-guest binding model.

Sugar binding of $BPAT^{2+}$•$2Cl^-$ in the aggregated state

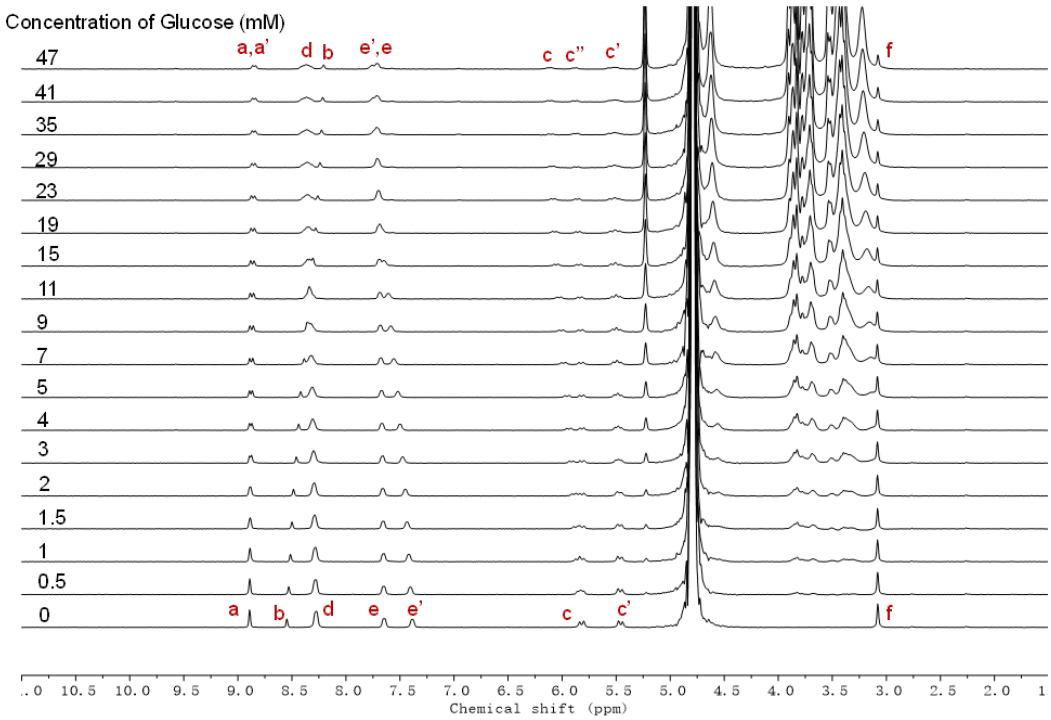

Fig. S46. Full ^1H NMR spectra (400 MHz, D_2O, 298 K) of $BPAT^{2+}$•$2Cl^-$ (0.5 mM) and NaCl (20 mM) titrated with glucose.

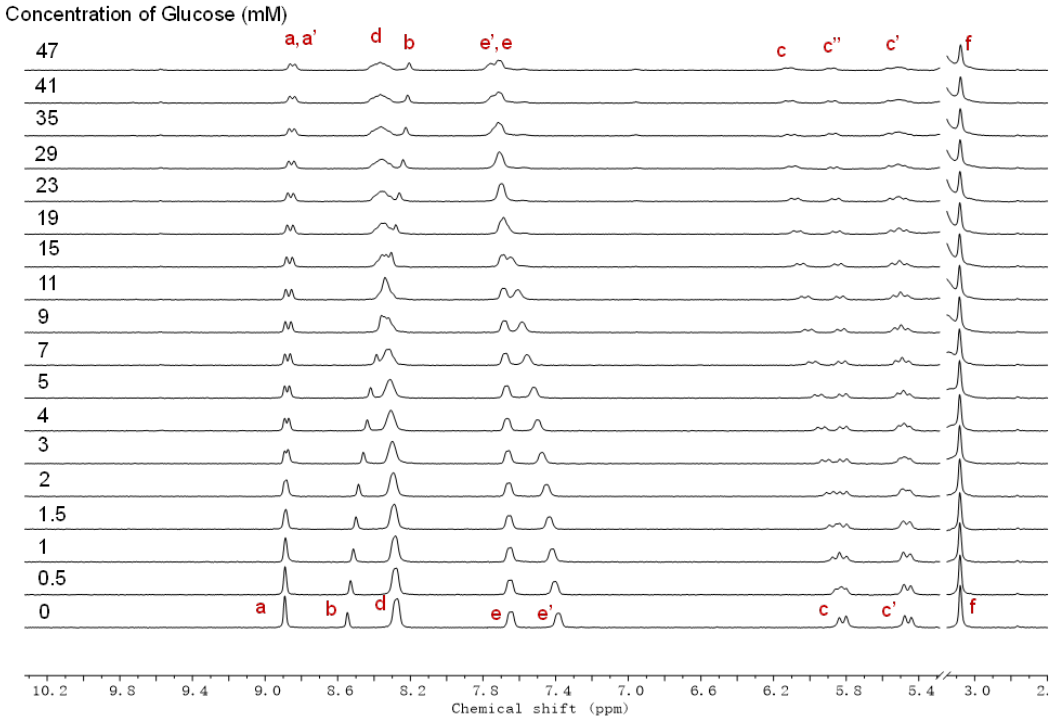

Fig. S47. Partial ^{1}H NMR spectra (400 MHz, D_2O, 298 K) of $BPAT^{2+}\bullet 2Cl^{-}$ (0.5 mM) and NaCl (20 mM) titrated with glucose showing the change of chemical shift of $BPAT^{2+}\bullet 2Cl^{-}$.

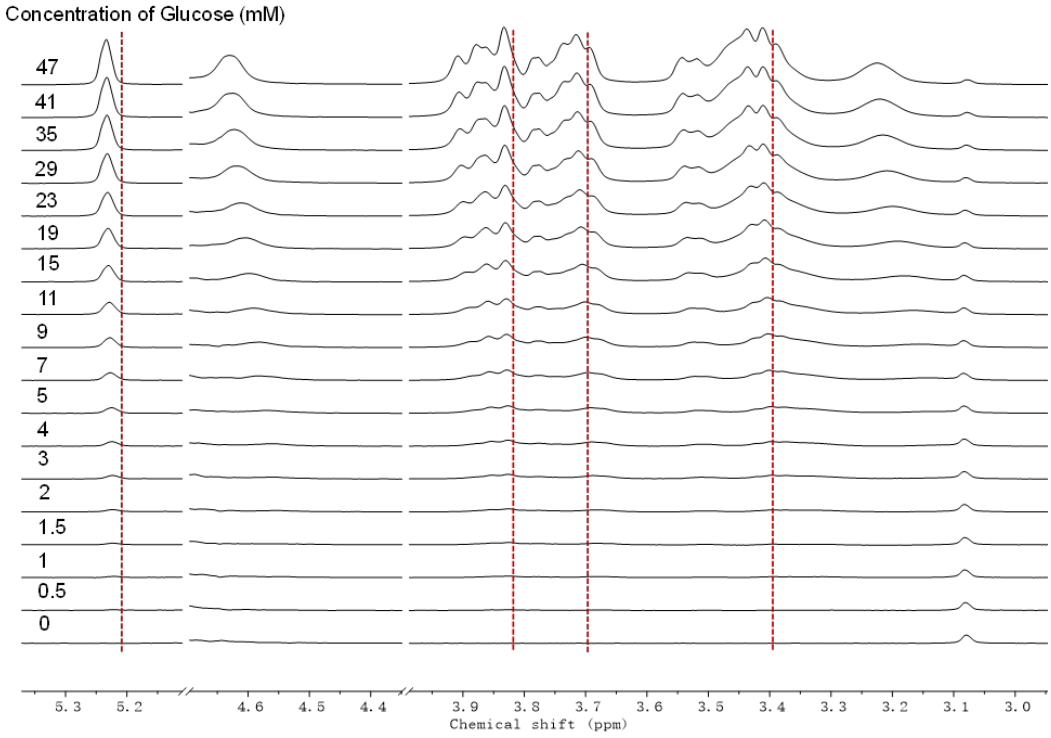

Fig. S48. Partial ^{1}H NMR spectra (400 MHz, D_2O, 298 K) of $BPAT^{2+}\bullet 2Cl^{-}$ (0.5 mM) and NaCl (20 mM) titrated with glucose showing the change of chemical shift of glucose.

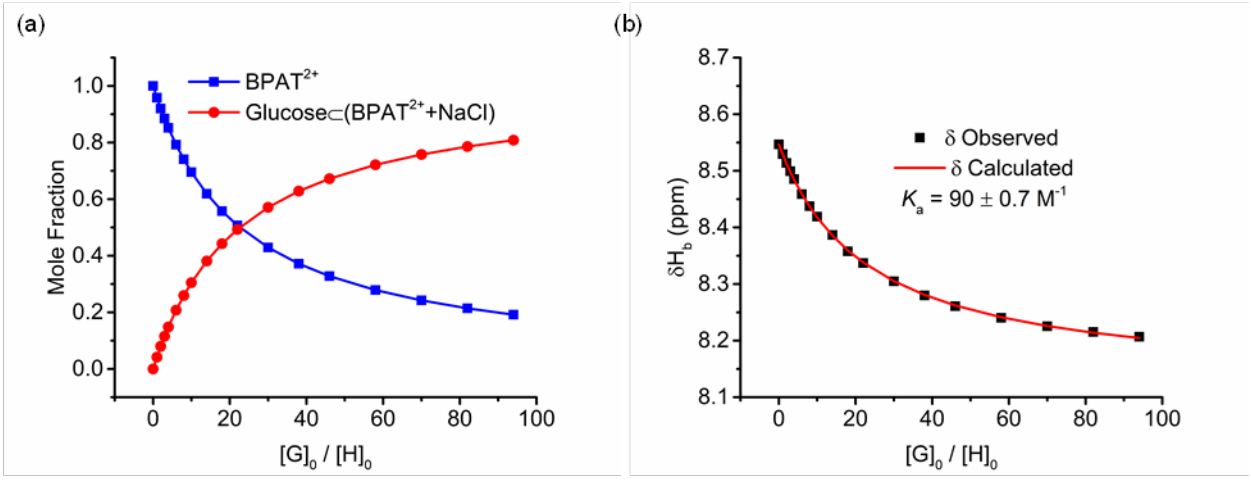

Fig. S49. (a) Calculated changes of mole fractions for $BPAT^{2+}$•$2Cl^-$ (blue trace) and glucose⊂ $BPAT^{2+}$•$2Cl^-$ (red trace) in the presence of NaCl (20 mM) over the guest-host mole ratio. (b) Titration isotherm created by monitoring changes in the chemical shift of proton b for $BPAT^{2+}$•$2Cl^-$ (0.5 mM) in the presence of NaCl (20 mM) caused by the addition of glucose in D_2O at 298 K. Red lines are the curve fitting using a 1:1 host-guest binding model.

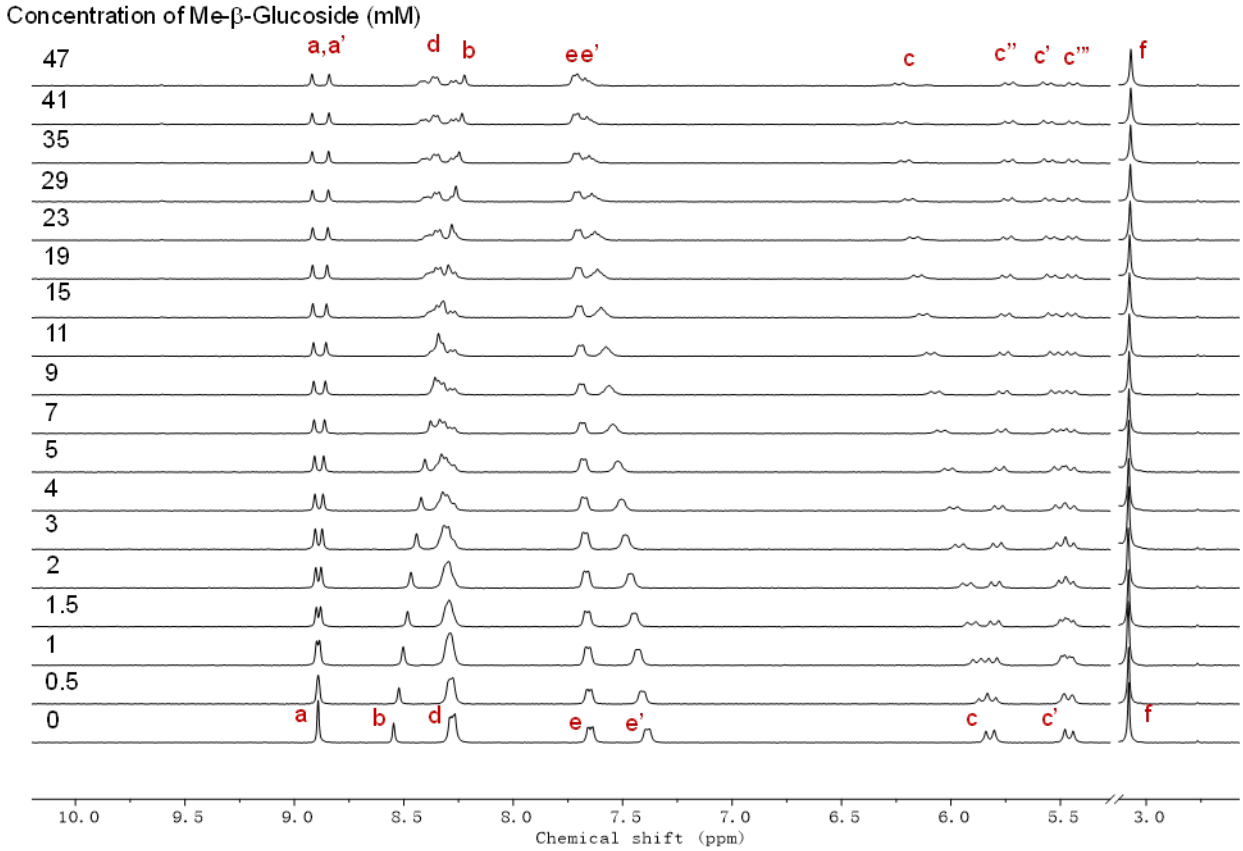

Fig. S50. Partial ^1H NMR spectra (400 MHz, D_2O, 298 K) of $BPAT^{2+}$•$2Cl^-$ (0.5 mM) and NaCl (20 mM) titrated with Me-β-glucoside.

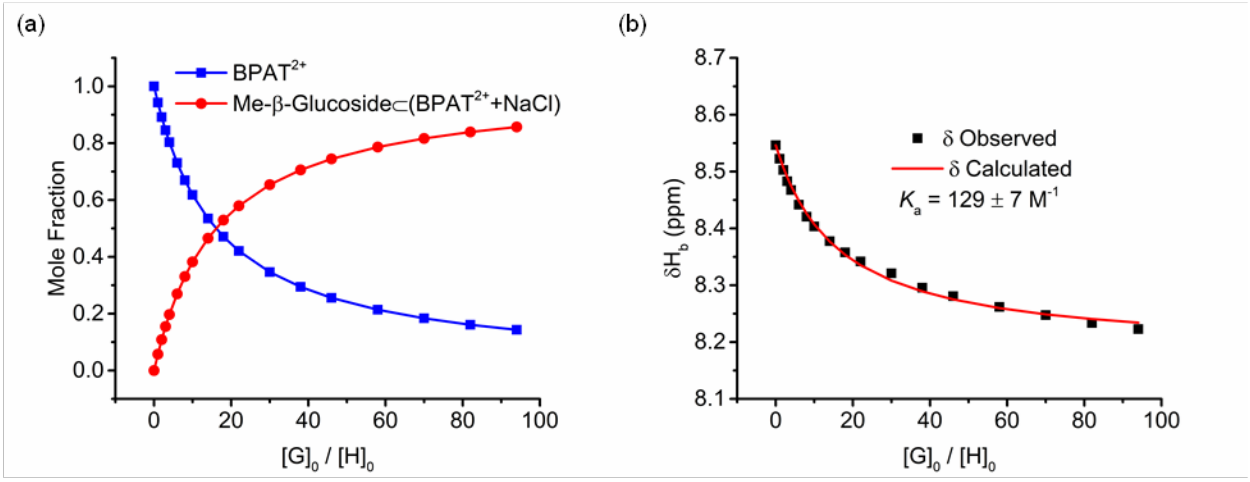

Fig. S51. (a) Calculated changes of mole fractions for $BPAT^{2+}$•$2Cl^-$ (blue trace) and Me-β-glucoside⊂ $BPAT^{2+}$•$2Cl^-$ (red trace) in the presence of NaCl (20 mM) over the guest-host mole ratio. (b) Titration isotherm created by monitoring changes in the chemical shift of proton b for $BPAT^{2+}$•$2Cl^-$ (0.5 mM) in the presence of NaCl (20 mM) caused by the addition of Me-β-glucoside in D_2O at 298 K. Red lines are the curve fitting using a 1:1 host-guest binding model.

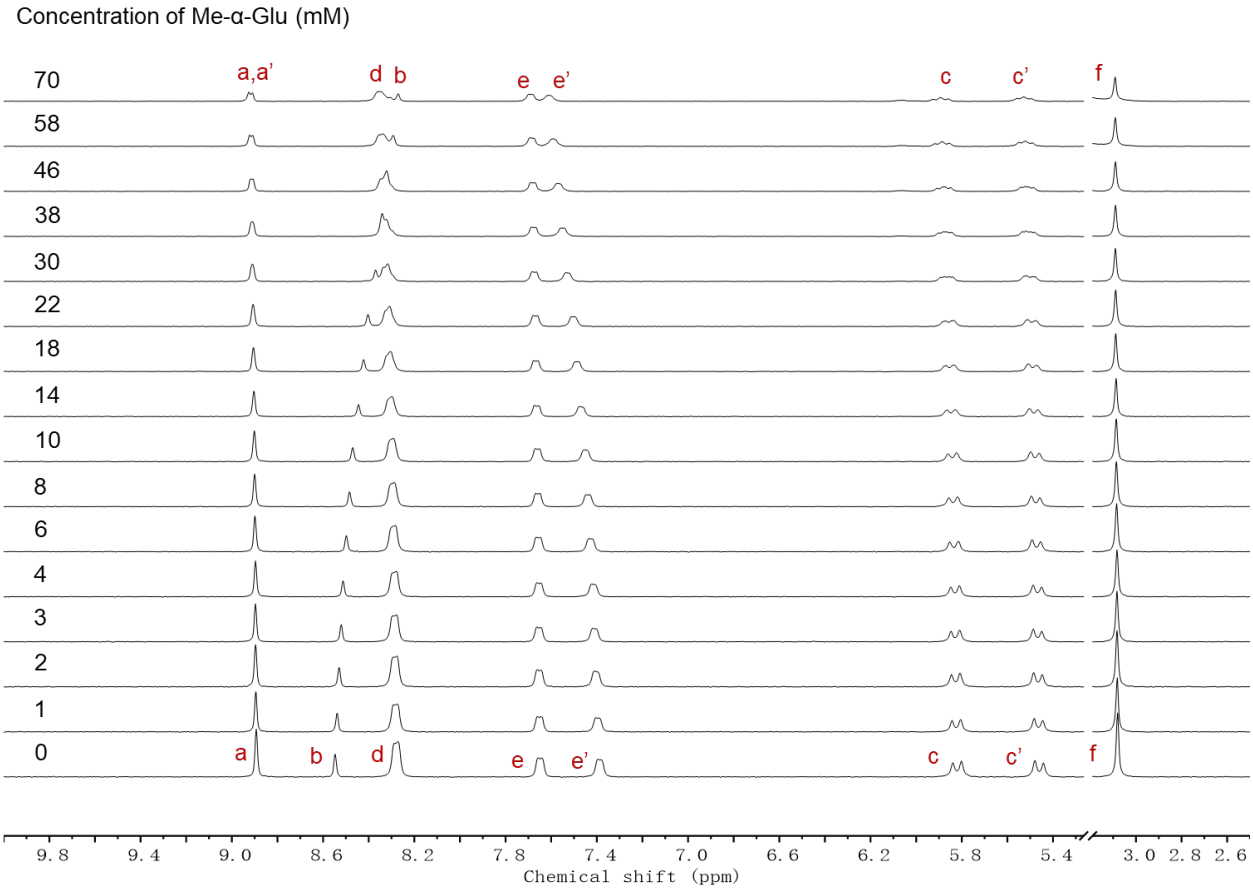

Fig. S52. Partial ^1H NMR spectra (400 MHz, D_2O, 298 K) of $BPAT^{2+}$•$2Cl^-$ (0.5 mM) and NaCl (20 mM) titrated with Me-α-glucoside.

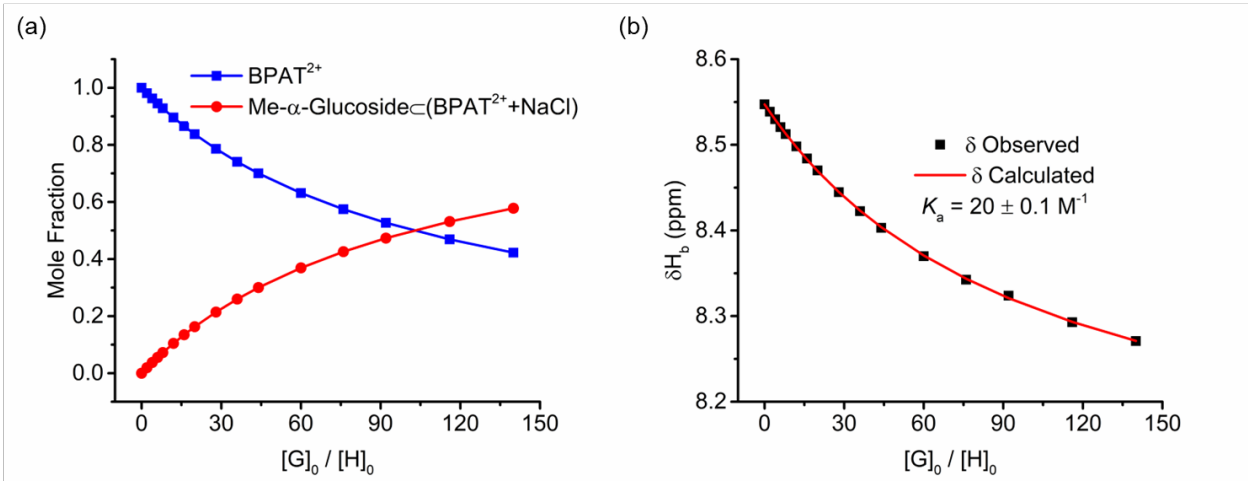

Fig. S53. (a) Calculated changes of mole fractions for $BPAT^{2+}$•$2Cl^-$ (blue trace) and Me-α-glucoside⊂ $BPAT^{2+}$•$2Cl^-$ (red trace) in the presence of NaCl (20 mM) over the guest-host mole ratio. (b) Titration isotherm created by monitoring changes in the chemical shift of proton b for $BPAT^{2+}$•$2Cl^-$ (0.5 mM) in the presence of NaCl (20 mM) caused by the addition of Me-α-glucoside in D_2O at 298 K. Red lines are the curve fitting using a 1:1 host-guest binding model.

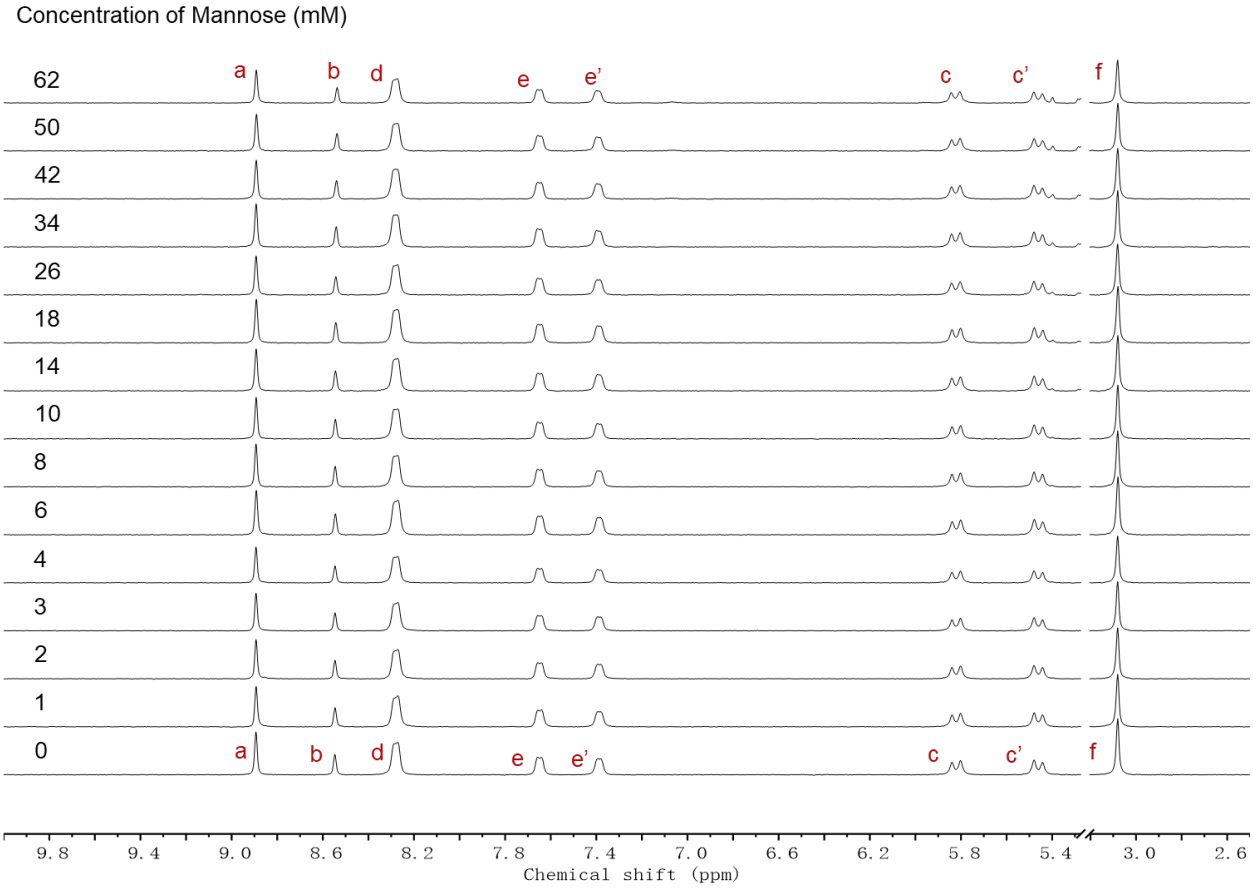

Fig. S54. Partial ^1H NMR spectra (400 MHz, D_2O, 298 K) of $BPAT^{2+}$•$2Cl^-$ (0.5 mM) and NaCl (20 mM) titrated with mannose.

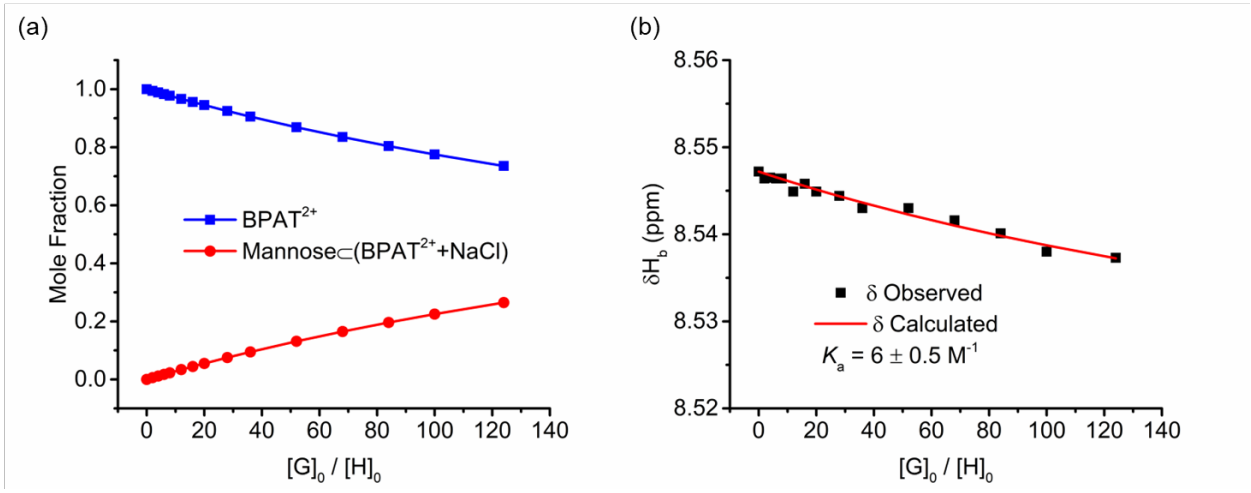

Fig. S55. (a) Calculated changes of mole fractions for $BPAT^{2+}$•$2Cl^-$ (blue trace) and mannose⊂ $BPAT^{2+}$•$2Cl^-$ (red trace) in the presence of NaCl (20 mM) over the guest-host mole ratio. (b) Titration isotherm created by monitoring changes in the chemical shift of proton b for $BPAT^{2+}$•$2Cl^-$ (0.5 mM) in the presence of NaCl (20 mM) caused by the addition of mannose in D_2O at 298 K. Red lines are the curve fitting using a 1:1 host-guest binding model.

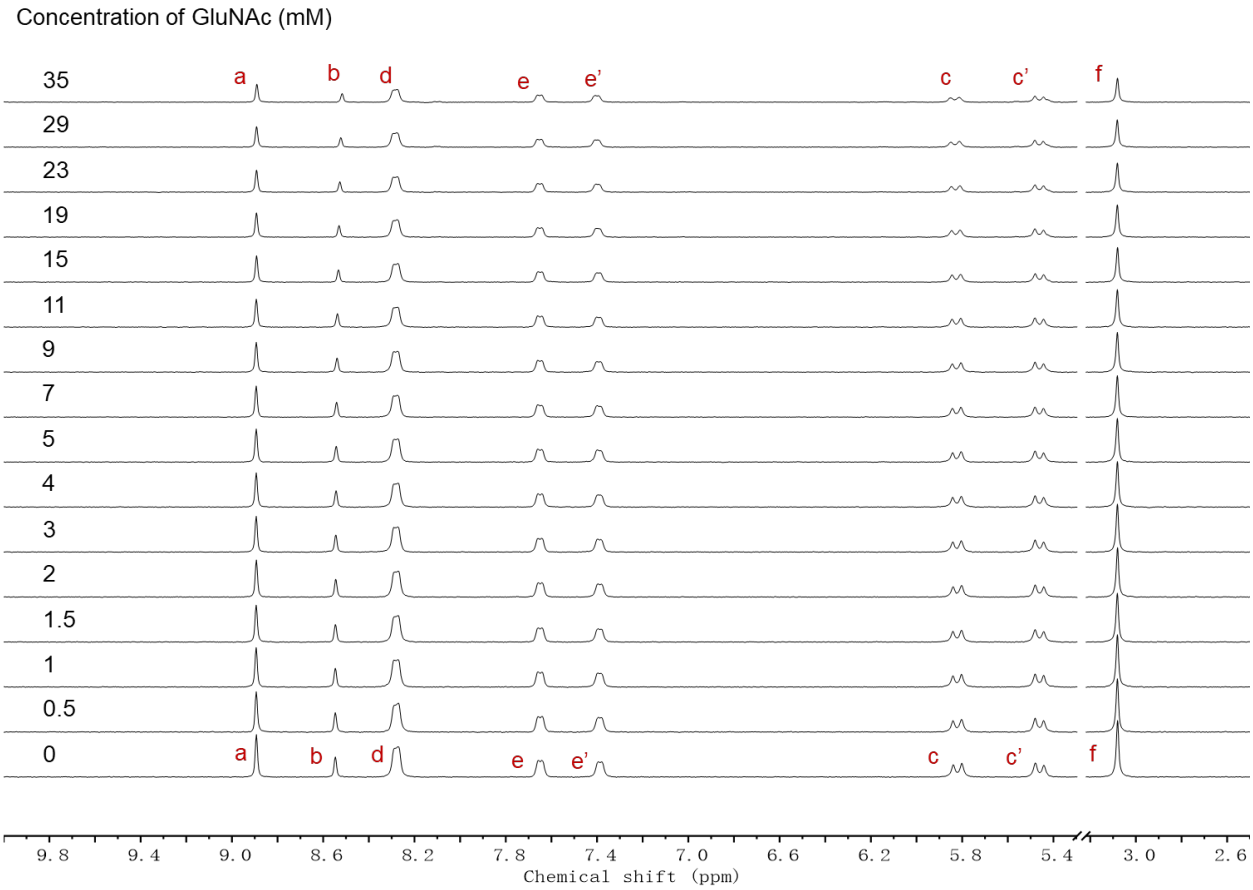

Fig. S56. Partial ^1H NMR spectra (400 MHz, D_2O, 298 K) of $BPAT^{2+}$•$2Cl^-$ (0.5 mM) and NaCl (20 mM) titrated with GluNAc.

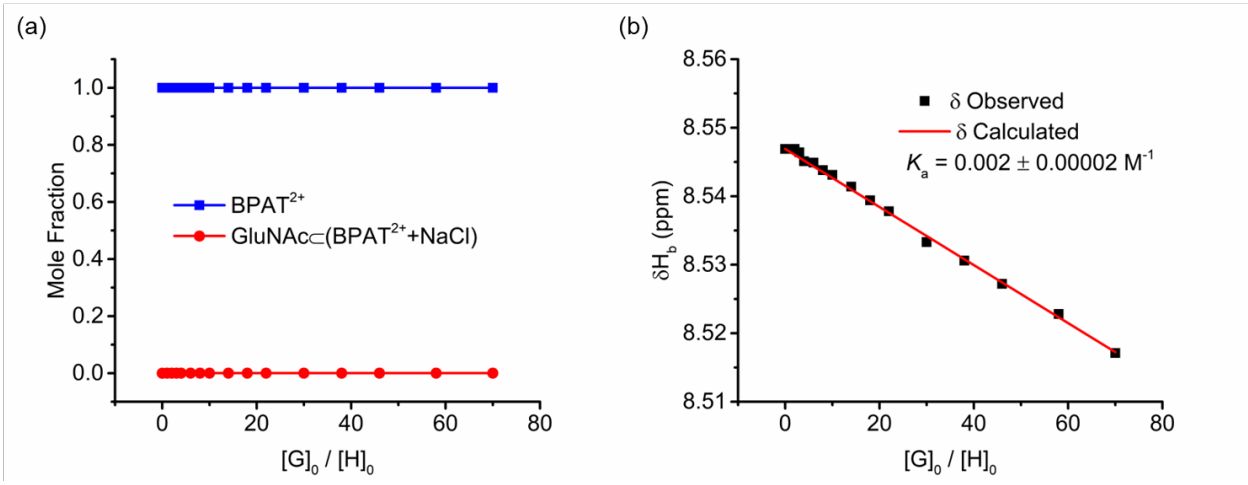

Fig. S57. (a) Calculated changes of mole fractions for $BPAT^{2+}$•$2Cl^-$ (blue trace) and GluNAc⊂ $BPAT^{2+}$•$2Cl^-$ (red trace) in the presence of NaCl (20 mM) over the guest-host mole ratio. (b) Titration isotherm created by monitoring changes in the chemical shift of proton b for $BPAT^{2+}$•$2Cl^-$ (0.5 mM) in the presence of NaCl (20 mM) caused by the addition of GluNAc in D_2O at 298 K. Red lines are the curve fitting using a 1:1 host-guest binding model.

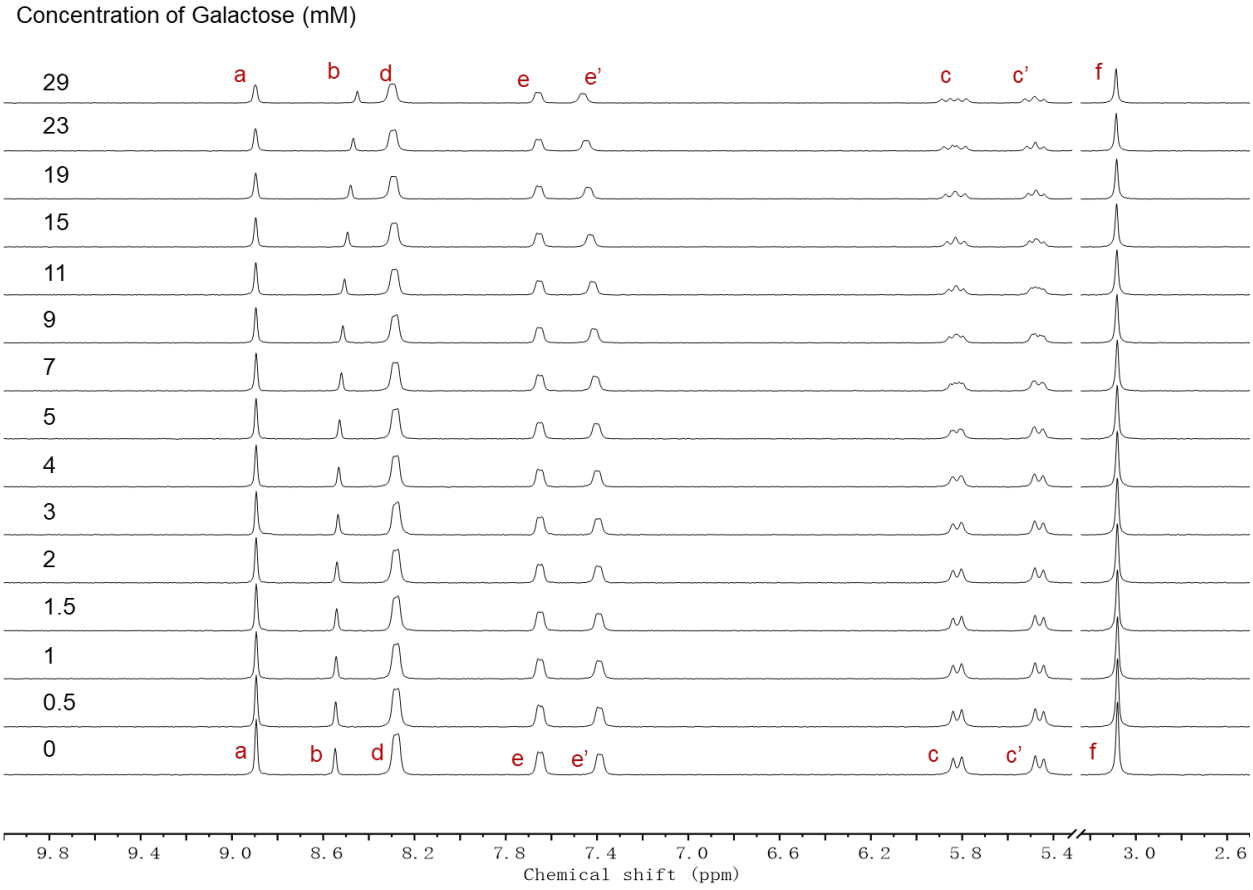

Fig. S58. Partial ^1H NMR spectra (400 MHz, D_2O, 298 K) of $BPAT^{2+}$•$2Cl^-$ (0.5 mM) and NaCl (20 mM) titrated with galactose.

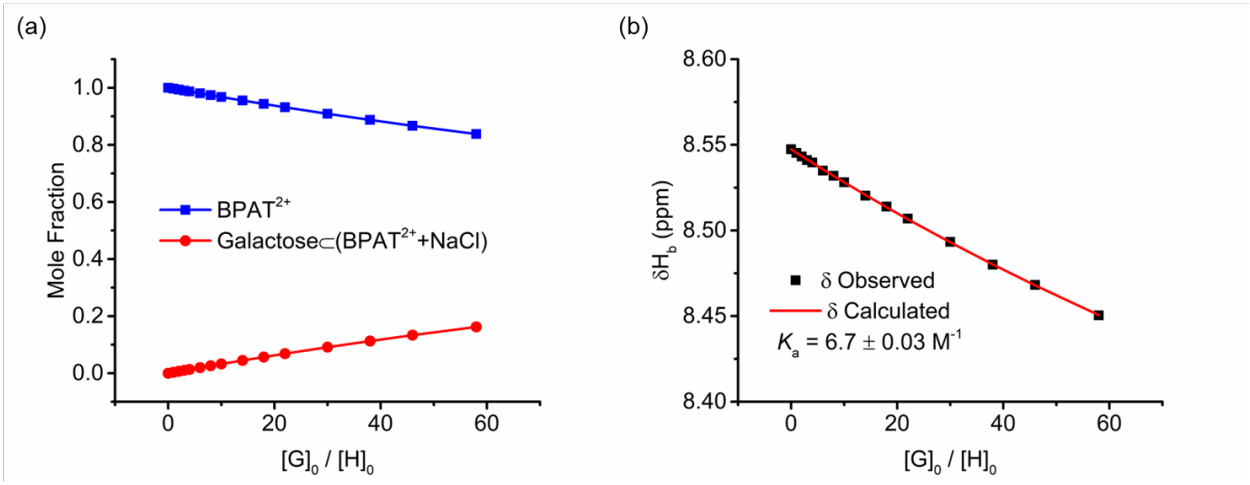

Fig. S59. (a) Calculated changes of mole fractions for $BPAT^{2+}$•$2Cl^-$ (blue trace) and galactose⊂ $BPAT^{2+}$•$2Cl^-$ (red trace) in the presence of NaCl (20 mM) over the guest-host mole ratio. (b) Titration isotherm created by monitoring changes in the chemical shift of proton b for $BPAT^{2+}$•$2Cl^-$ (0.5 mM) in the presence of NaCl (20 mM) caused by the addition of galactose in D_2O at 298 K. Red lines are the curve fitting using a 1:1 host-guest binding model.

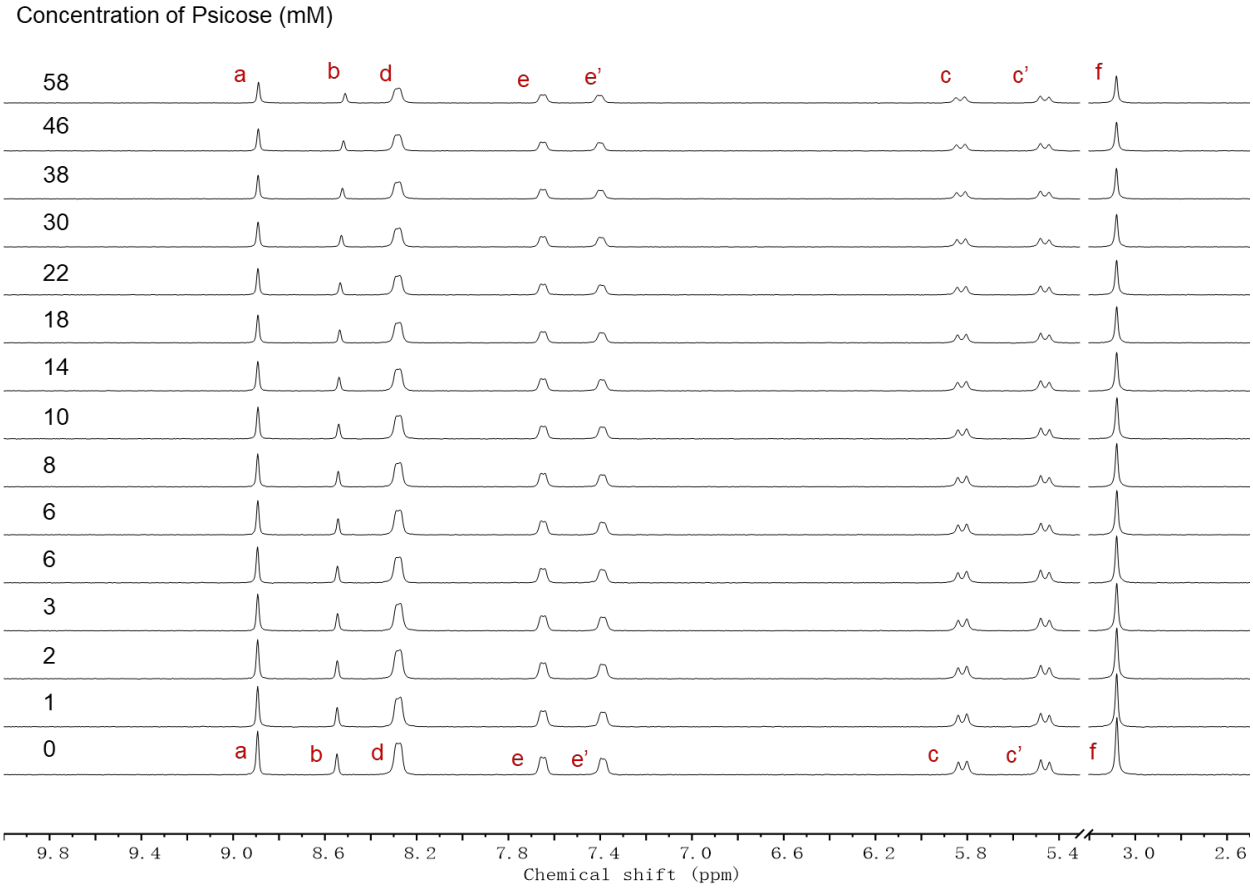

Fig. S60. Partial ^1H NMR spectra (400 MHz, D_2O, 298 K) of $BPAT^{2+}$•$2Cl^-$ (0.5 mM) and NaCl (20 mM) titrated with psicose.

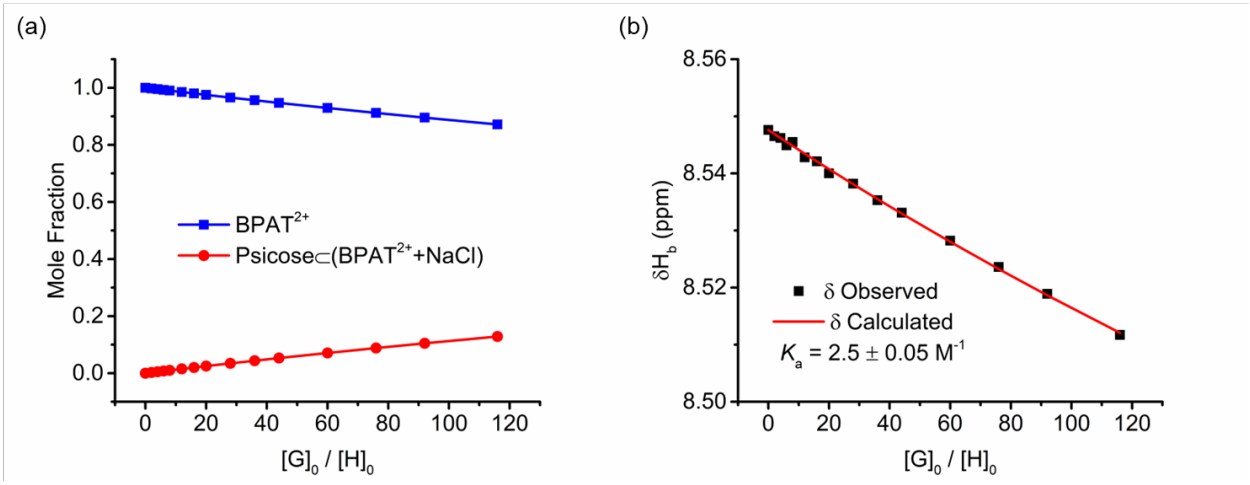

Fig. S61. (a) Calculated changes of mole fractions for $BPAT^{2+}$•$2Cl^-$ (blue trace) and psicose⊂ $BPAT^{2+}$•$2Cl^-$ (red trace) in the presence of NaCl (20 mM) over the guest-host mole ratio. (b) Titration isotherm created by monitoring changes in the chemical shift of proton b for $BPAT^{2+}$•$2Cl^-$ (0.5 mM) in the presence of NaCl (20 mM) caused by the addition of psicose in D_2O at 298 K. Red lines are the curve fitting using a 1:1 host-guest binding model.

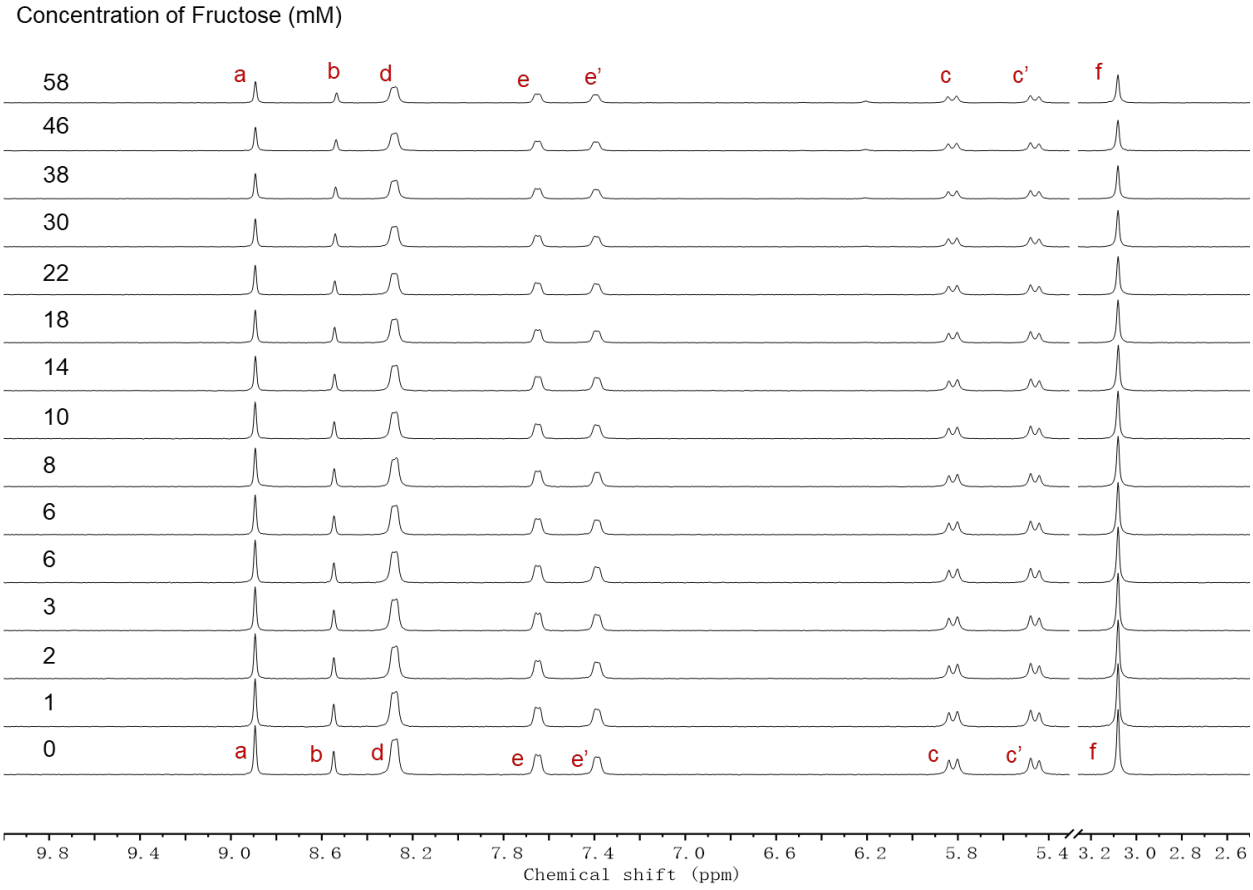

Fig. S62. Partial ^1H NMR spectra (400 MHz, D_2O, 298 K) of $BPAT^{2+}$•$2Cl^-$ (0.5 mM) and NaCl (20 mM) titrated with fructose.

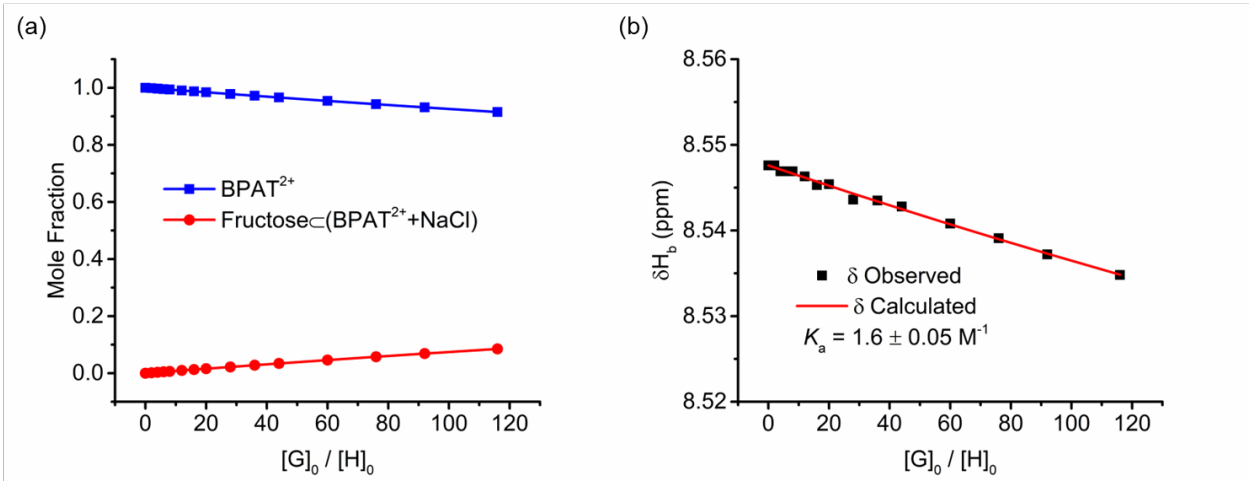

Fig. S63. (a) Calculated changes of mole fractions for $BPAT^{2+}$•$2Cl^-$ (blue trace) and fructose⊂ $BPAT^{2+}$•$2Cl^-$ (red trace) in the presence of NaCl (20 mM) over the guest-host mole ratio. (b) Titration isotherm created by monitoring changes in the chemical shift of proton b for $BPAT^{2+}$•$2Cl^-$ (0.5 mM) in the presence of NaCl (20 mM) caused by the addition of fructose in D_2O at 298 K. Red lines are the curve fitting using a 1:1 host-guest binding model.

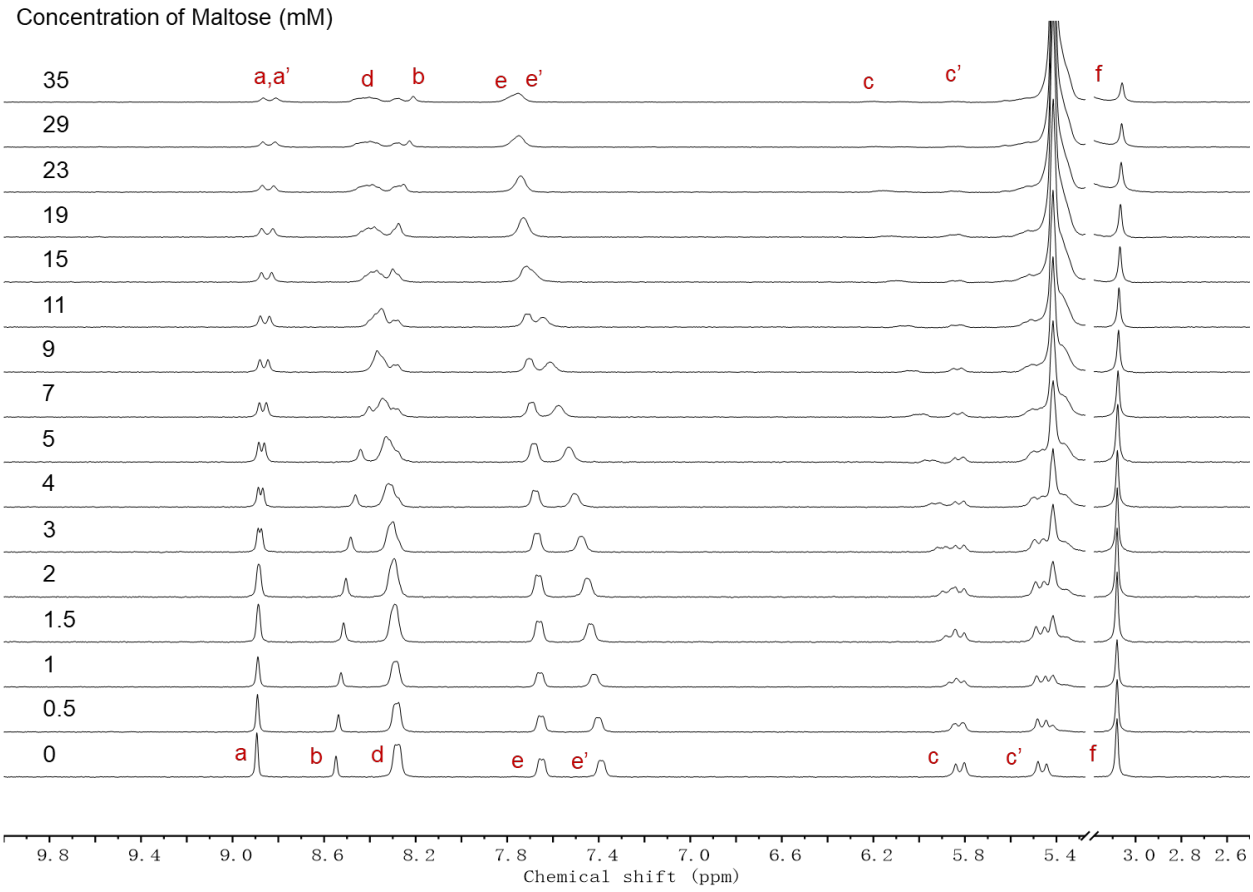

Fig. S64. Partial ^1H NMR spectra (400 MHz, D_2O, 298 K) of $BPAT^{2+}$•$2Cl^-$ (0.5 mM) and NaCl (20 mM) titrated with maltose.

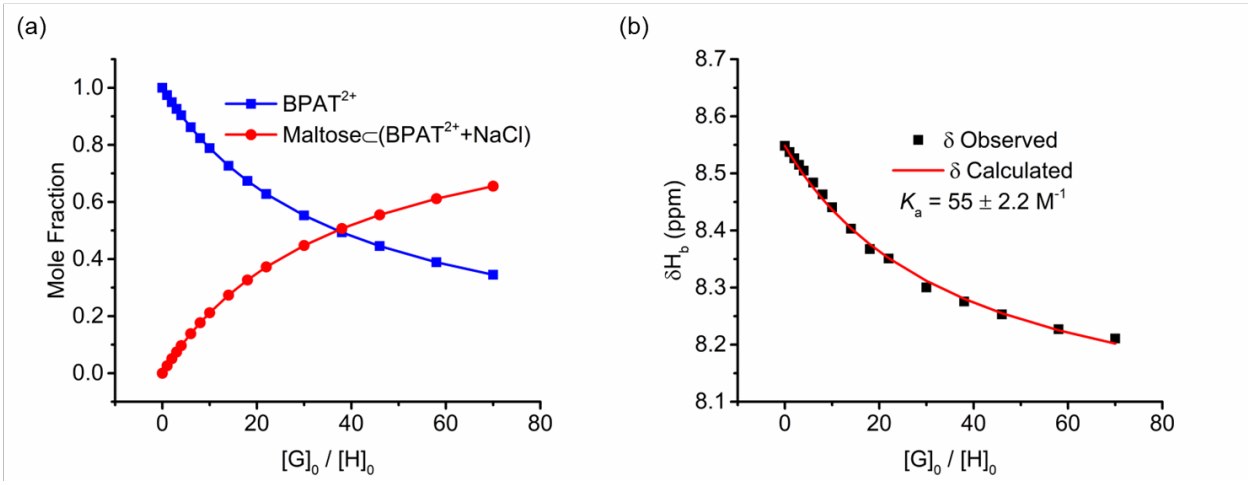

Fig. S65. (a) Calculated changes of mole fractions for $BPAT^{2+}$•$2Cl^-$ (blue trace) and maltose⊂ $BPAT^{2+}$•$2Cl^-$ (red trace) in the presence of NaCl (20 mM) over the guest-host mole ratio. (b) Titration isotherm created by monitoring changes in the chemical shift of proton b for $BPAT^{2+}$•$2Cl^-$ (0.5 mM) in the presence of NaCl (20 mM) caused by the addition of maltose in D_2O at 298 K. Red lines are the curve fitting using a 1:1 host-guest binding model.

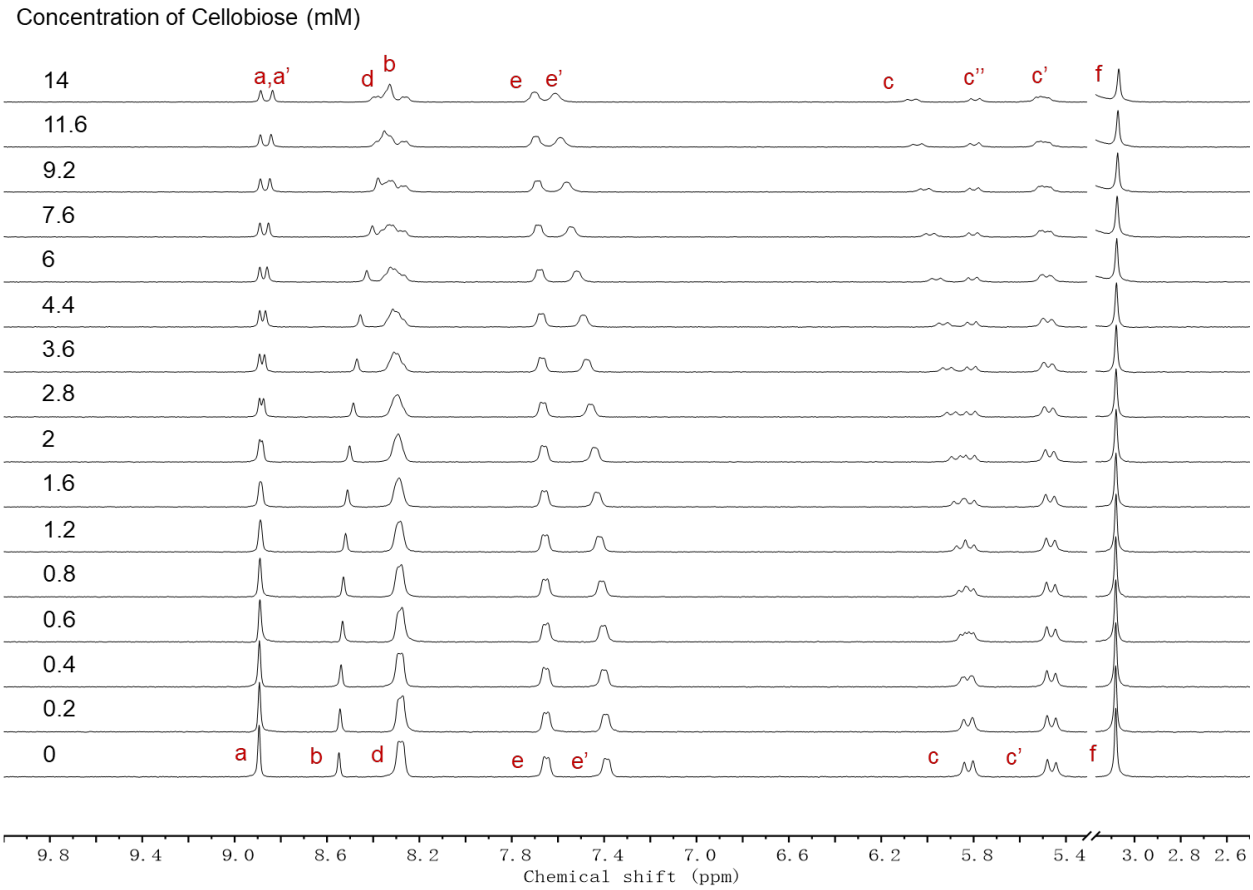

Fig. S66. Partial ^1H NMR spectra (400 MHz, D_2O, 298 K) of $BPAT^{2+}$•$2Cl^-$ $^-$ (0.5 mM) and NaCl (20 mM) titrated with cellobiose.

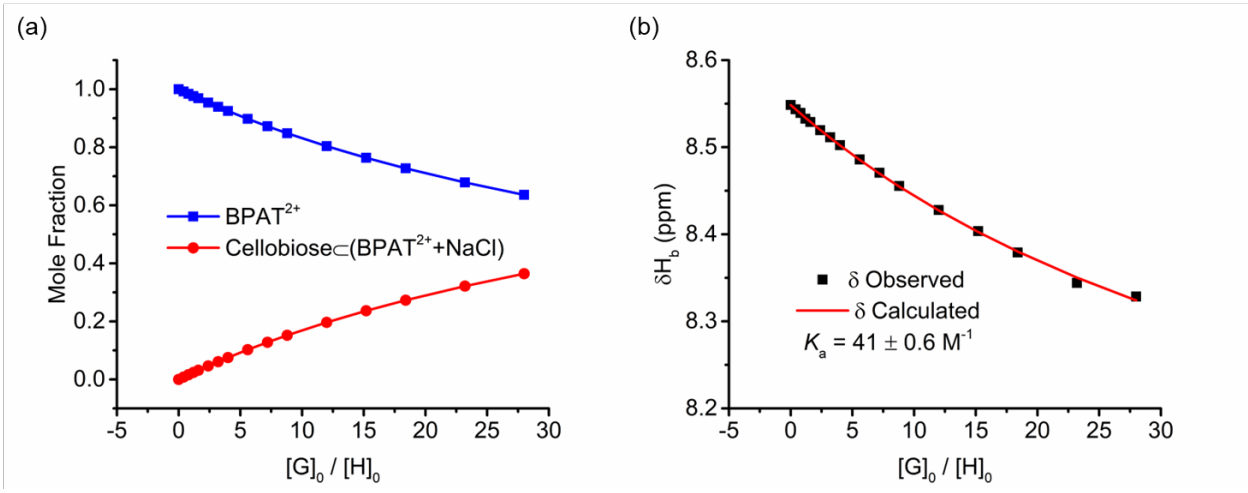

Fig. S67. (a) Calculated changes of mole fractions for $BPAT^{2+}$•$2Cl^-$ (blue trace) and cellobiose⊂ $BPAT^{2+}$•$2Cl^-$ (red trace) in the presence of NaCl (20 mM) over the guest-host mole ratio. (b) Titration isotherm created by monitoring changes in the chemical shift of proton b for $BPAT^{2+}$•$2Cl^-$ (0.5 mM) in the presence of NaCl (20 mM) caused by the addition of cellobiose in D_2O at 298 K. Red lines are the curve fitting using a 1:1 host-guest binding model.

Miscellaneous titrations

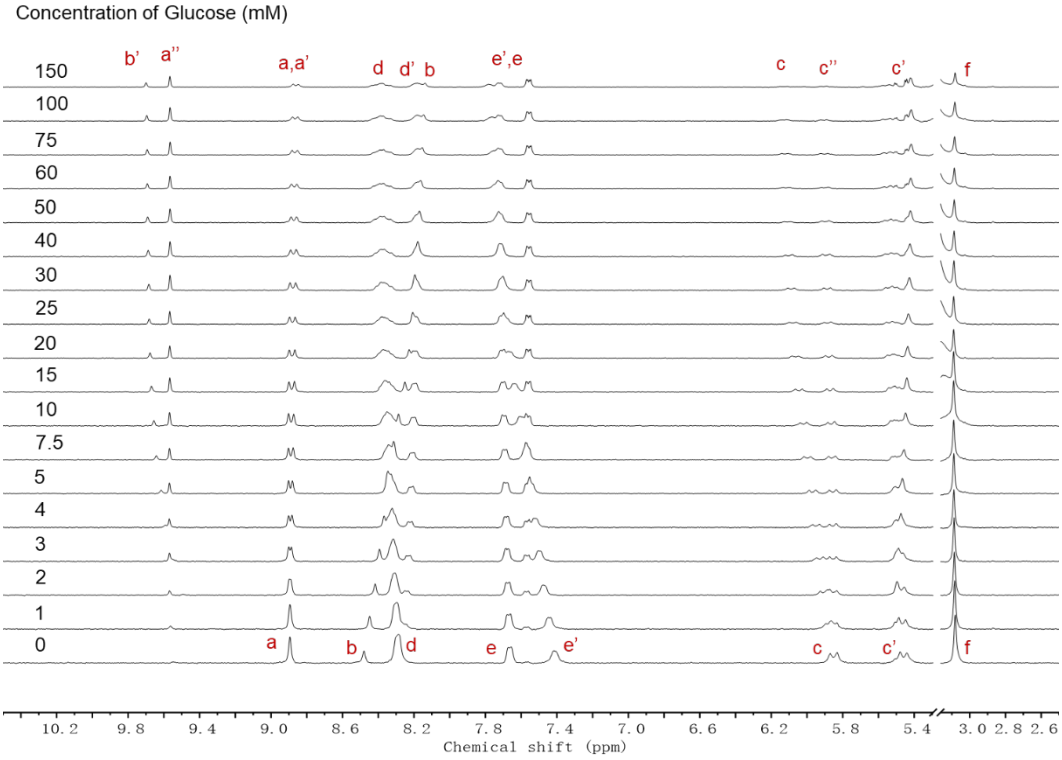

Fig. S68. Partial ^1H NMR spectra (400 MHz, D_2O, 298 K) of $BPAT^{2+}$•$2Cl^-$ (0.2 mM) titrated with glucose.

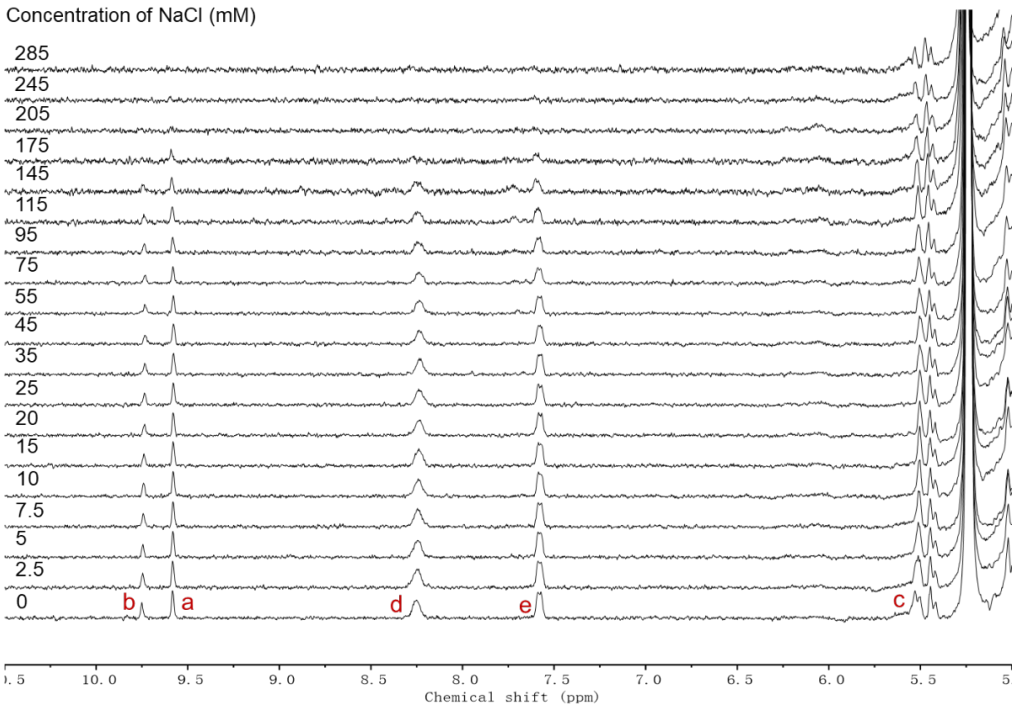

Fig. S69. Partial ^{1}H NMR spectra (400 MHz, D_2O, 298 K) of $BPAT^{2+}$•$2Cl^{-}$ (0.017 mM) in the presence of glucose (50 mM) titrated with NaCl, showing no aggregation of glucose ⊂ $BPAT^{2+}$•$2Cl^{-}$ in the presence of NaCl.

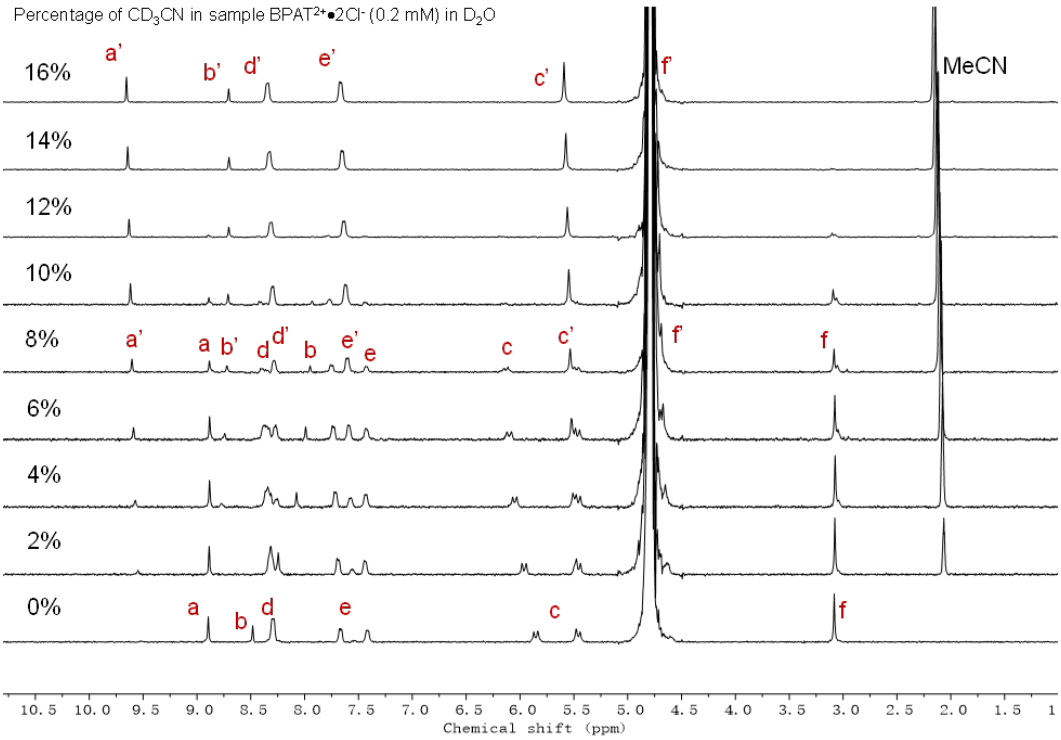

Fig. S70. Change of ^{1}H NMR spectra (400 MHz, D_2O/CD_3CN, 298 K) of $BPAT^{2+}$•$2Cl^{-}$ (0.2 mM) with increasing percentage volume of CD_3CN, showing the disruption of aggregation by decreasing the hydrophobic effect of the solvent.

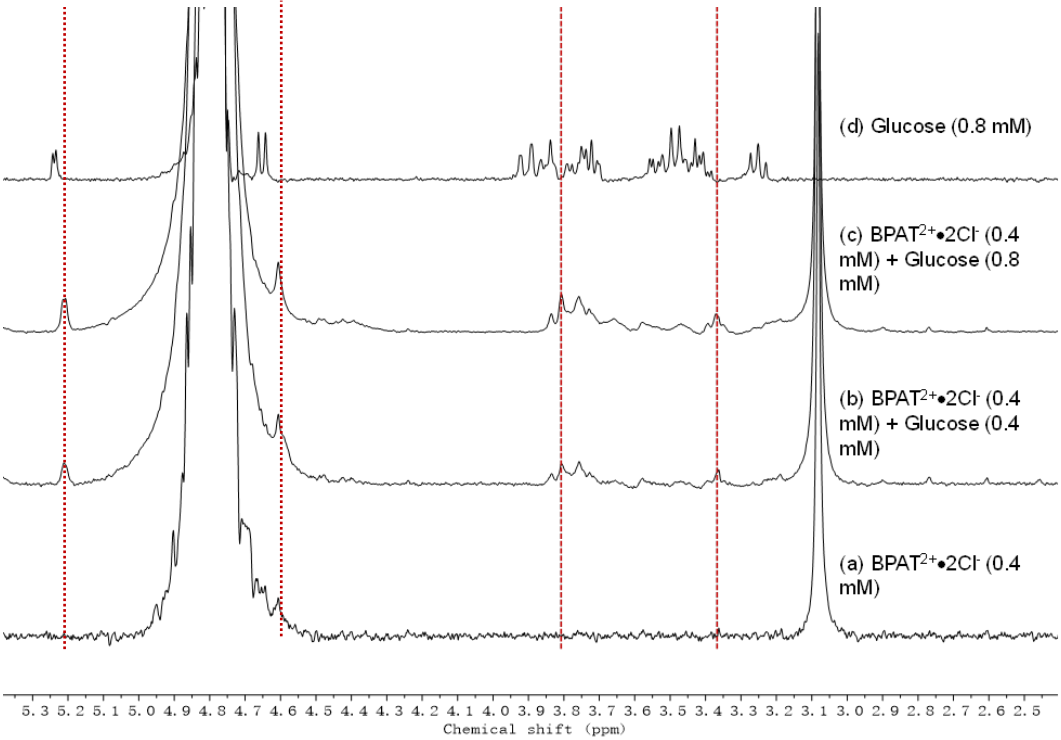

Fig. S71. Partial ^{1}H NMR spectra (400 MHz, D_2O, 298 K) of (a) $BPAT^{2+}$•$2Cl^{-}$ (0.4 mM), (b) a mixture of $BPAT^{2+}$•$2Cl^{-}$ (0.4 mM) and glucose (0.4 mM), (c) a mixture of $BPAT^{2+}$•$2Cl^{-}$ (0.4 mM) and glucose (0.8 mM), and (d) glucose (0.8 mM).

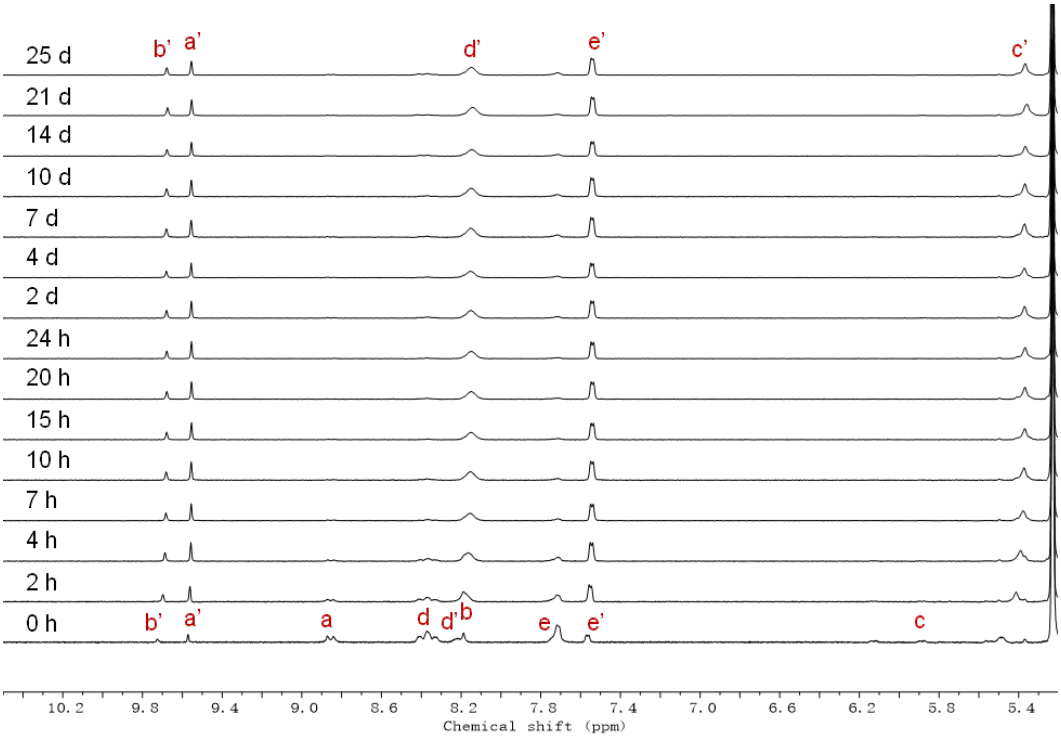

Fig. S72. Partial ^{1}H NMR spectra (600 MHz, D_2O, 298 K) of a mixture of $BPAT^{2+}$•$2Cl^{-}$ (0.2 mM) and glucose (33 mM) monitored over 25 days.

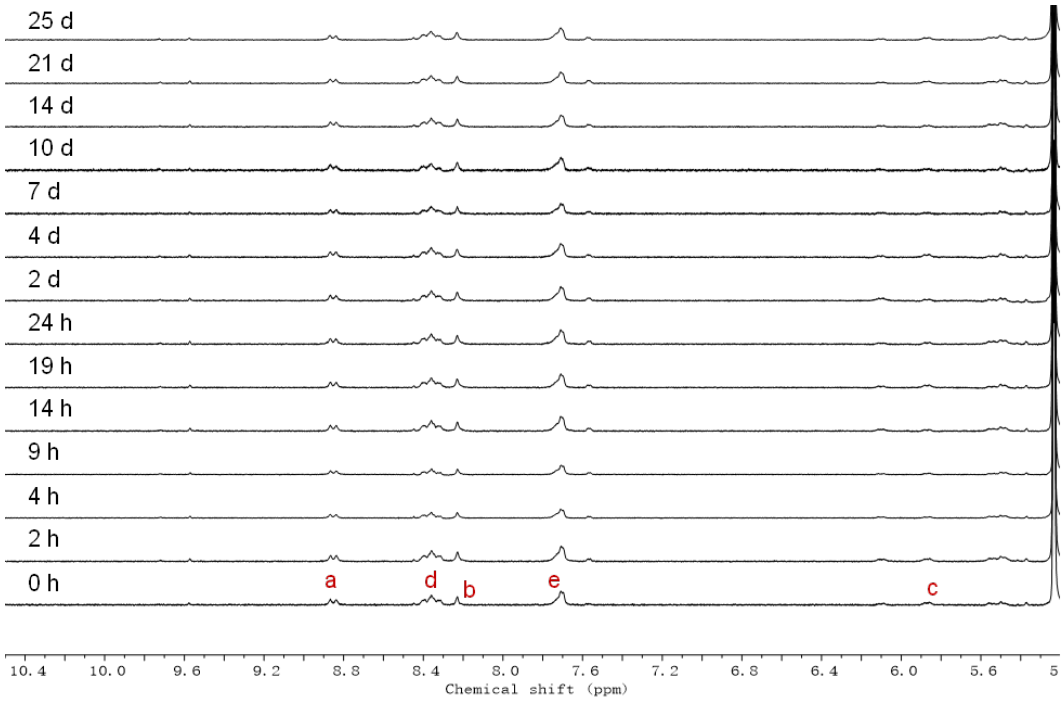

Fig. S73. Partial ^{1}H NMR spectra (600 MHz, D_2O, 298 K) of a mixture of $BPAT^{2+}$•$2Cl^-$ (0.2 mM), NaCl (20 mM), and glucose (33 mM) monitored over 25 days.

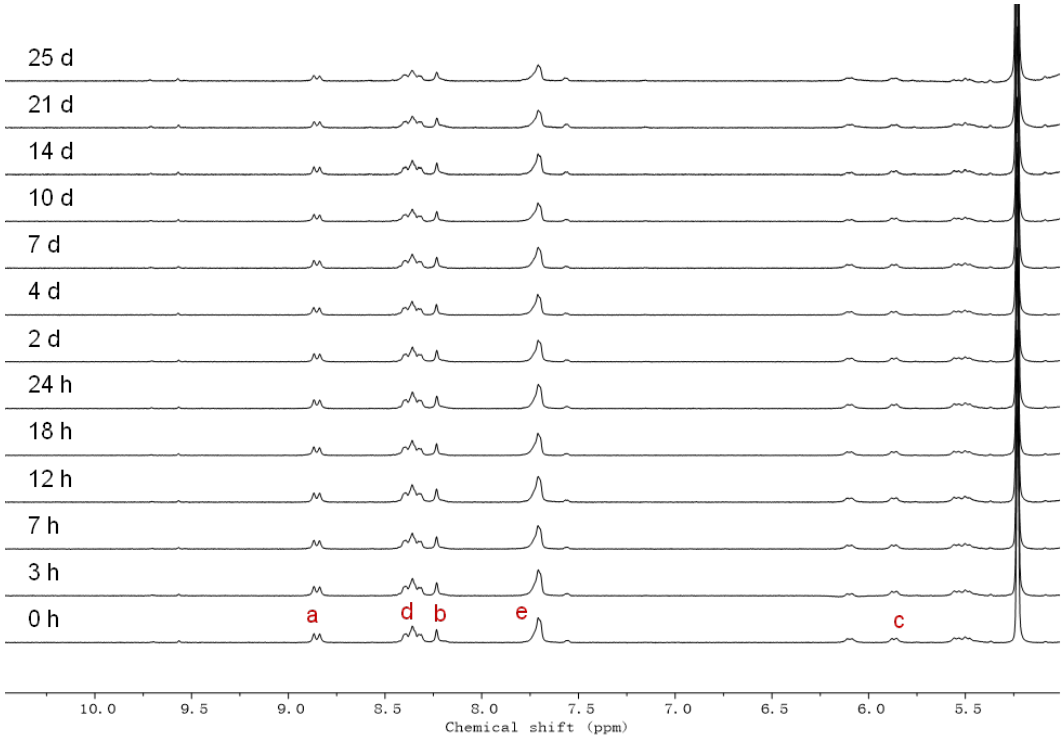

Fig. S74. Partial ^{1}H NMR spectra (600 MHz, D_2O, 298 K) of a mixture of $BPAT^{2+}$•$2Cl^-$ (0.5 mM), NaCl (20 mM), and glucose (40 mM) monitored over 25 days.

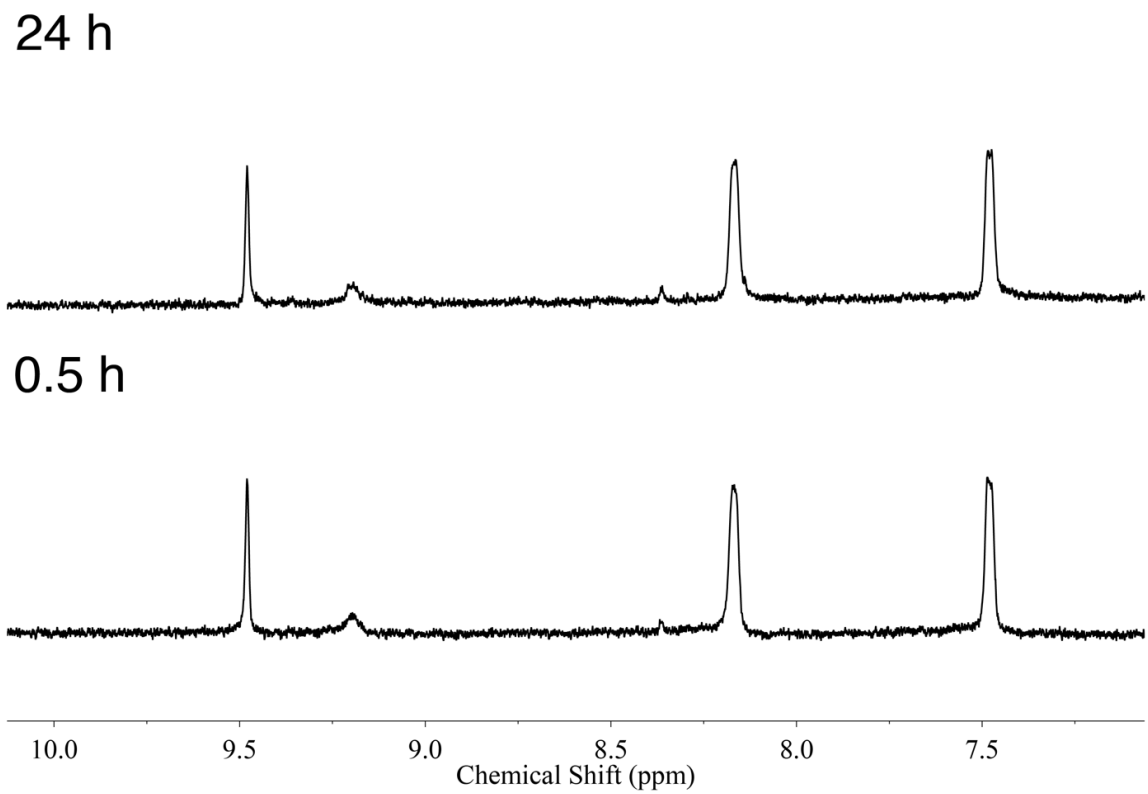

Fig. S75. ^{1}H NMR spectra (600 MHz, D_2O, 298 K) of a mixture of $BPAT^{2+}$•$2Cl^-$ (0.017 mM) and glucose (0.3 mM) monitored over 24 h at room temperature, showing no change of the chemical shift over time.

5. Isothermal Titration Calorimetry

Isothermal titration was performed on the MicroCal ITC_{200} system at 23 °C. The experiments were conducted in a titration cell with a working volume of 200 μL. The capacity of the injection syringe is 40 μL. The stirring speed was set at 750 rpm. Host and guest solutions were prepared in Milli-Q water. A stock solution of $BPAT^{2+}$•$2Cl^-$ was prepared in Milli-Q water and filtrated. The concentration of $BPAT^{2+}$•$2Cl^-$ was calibrated using UV-Vis absorption spectrometry. All samples were equilibrated for 24 hours before use. The host solution $BPAT^{2+}$•$2Cl^-$ was placed in the titration cell, and the guests were loaded into the titration syringe. In each case, 20-25 injections were performed. The heat of dilution was measured by titrating the guest into a blank solution. The heat of dilution was subtracted before analyzing with MicroCal iTC_{200} software using a 1:1 host-guest binding model and plotted by Origin Lab software.

Sugar binding of $BPAT^{2+}$•$2Cl^-$ in its free state

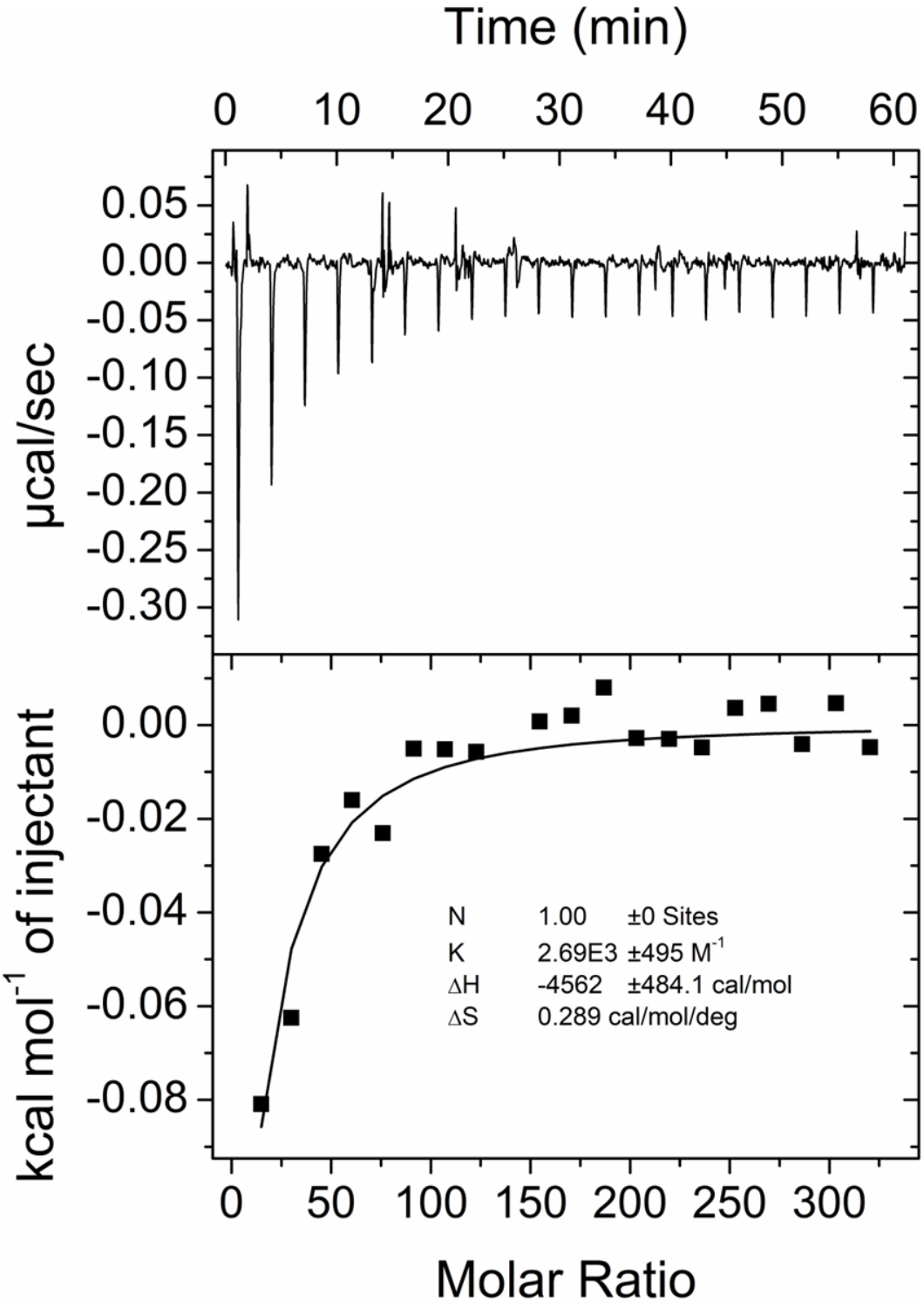

Fig. S76. ITC profiles for the titration of $BPAT^{2+}$•$2Cl^-$ (0.01 mM in the cell) with D-Glucose (20 mM in syringe) in H_2O. The solid line represents the best non-linear fit of the data to a 1:1 binding model (K_a = 2690 ± 495 M^{-1}, ΔH = -4.56 ± 0.48 kcal/mol).

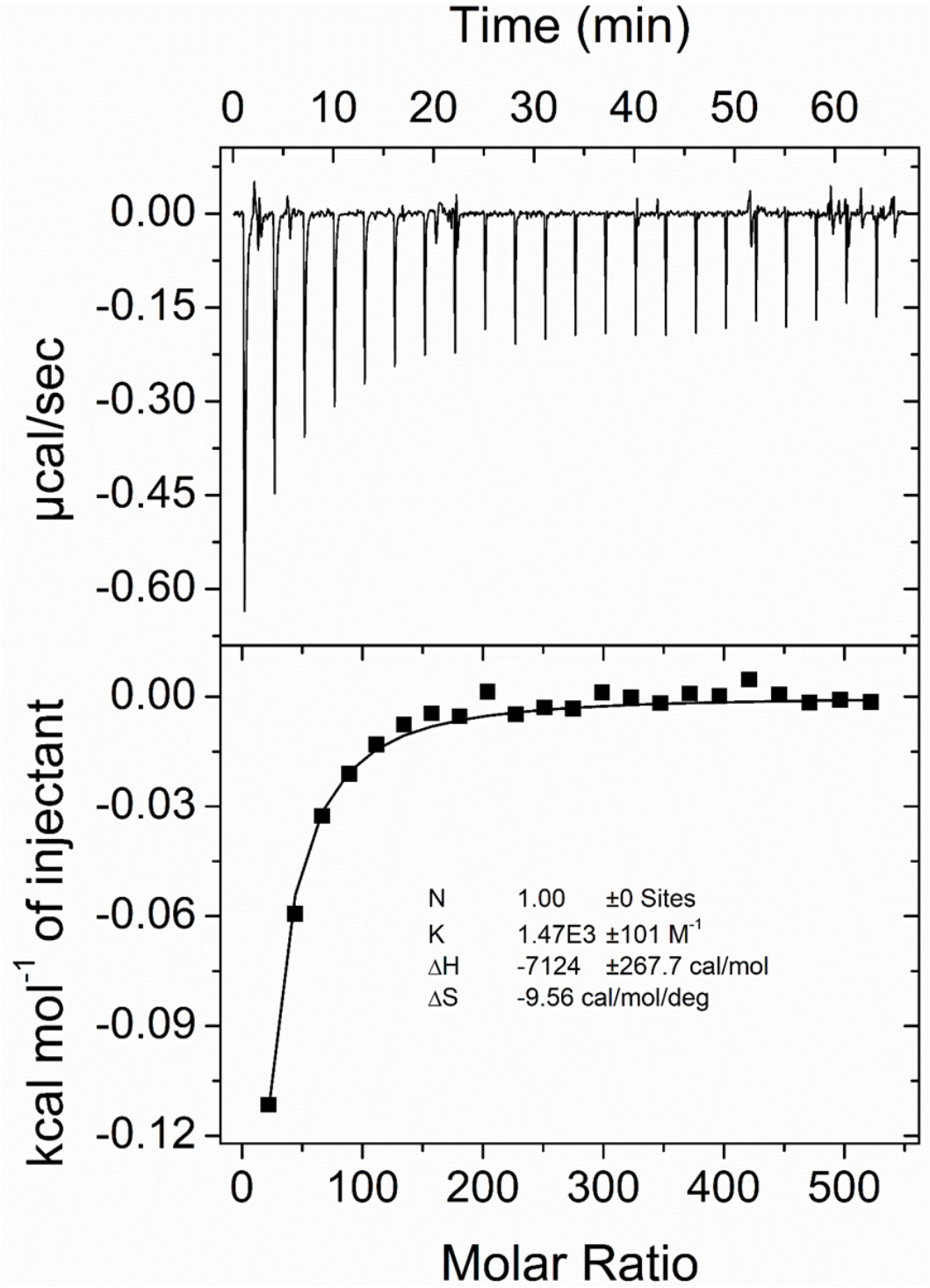

Fig. S77. ITC profiles for the titration of $BPAT^{2+}$•$2Cl^-$ (0.017 mM in the cell) with Me-β-glucoside (50 mM in syringe) in H_2O. The solid line represents the best non-linear fit of the data to a 1:1 binding model (K_a = 1470 ± 101 M^{-1}, ΔH = -7.12 ± 0.27 kcal/mol).

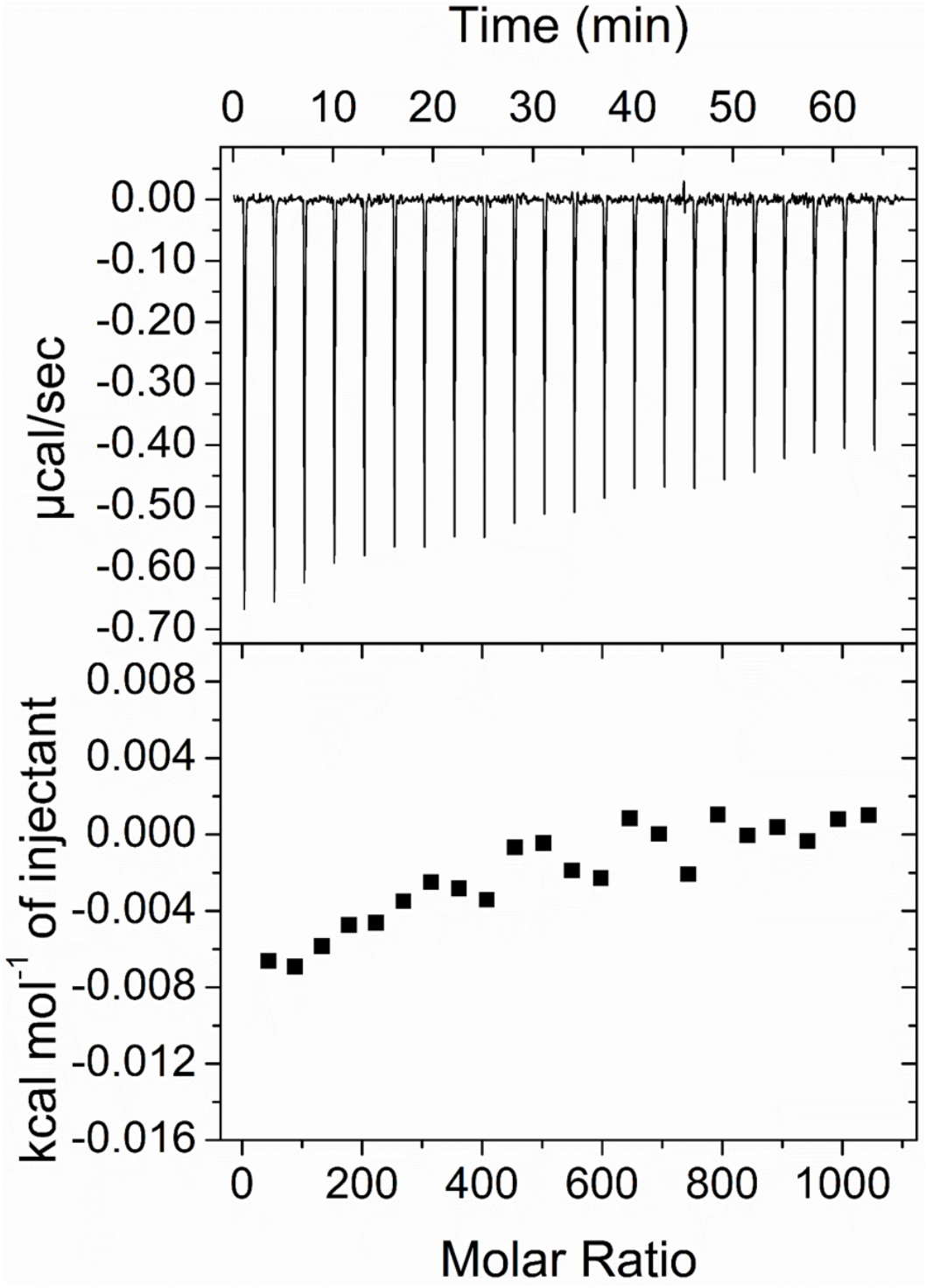

Fig. S78. ITC profiles for the titration of $BPAT^{2+}•2Cl^{-}$ (0.017 mM in the cell) with Me-α-glucoside (100 mM in syringe) in H_2O. Note: The heat formation is too small to reliably determine the K_a and ΔH.

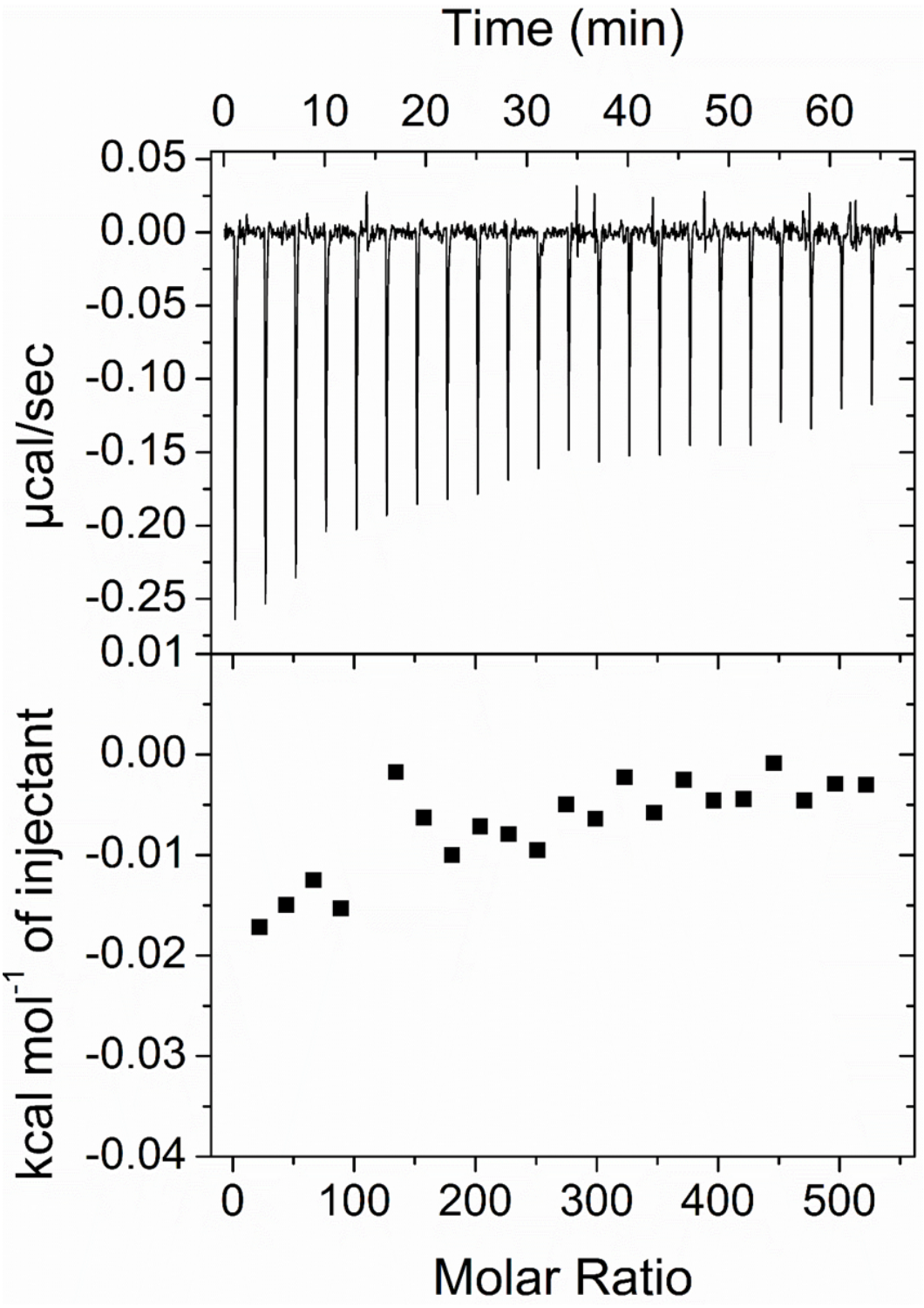

Fig. S79. ITC profiles for the titration of $BPAT^{2+}•2Cl^-$ (0.017 mM in the cell) with GluNAc (50 mM in syringe) in H_2O. Note: The heat formation is too small to reliably determine the K_a and ΔH.

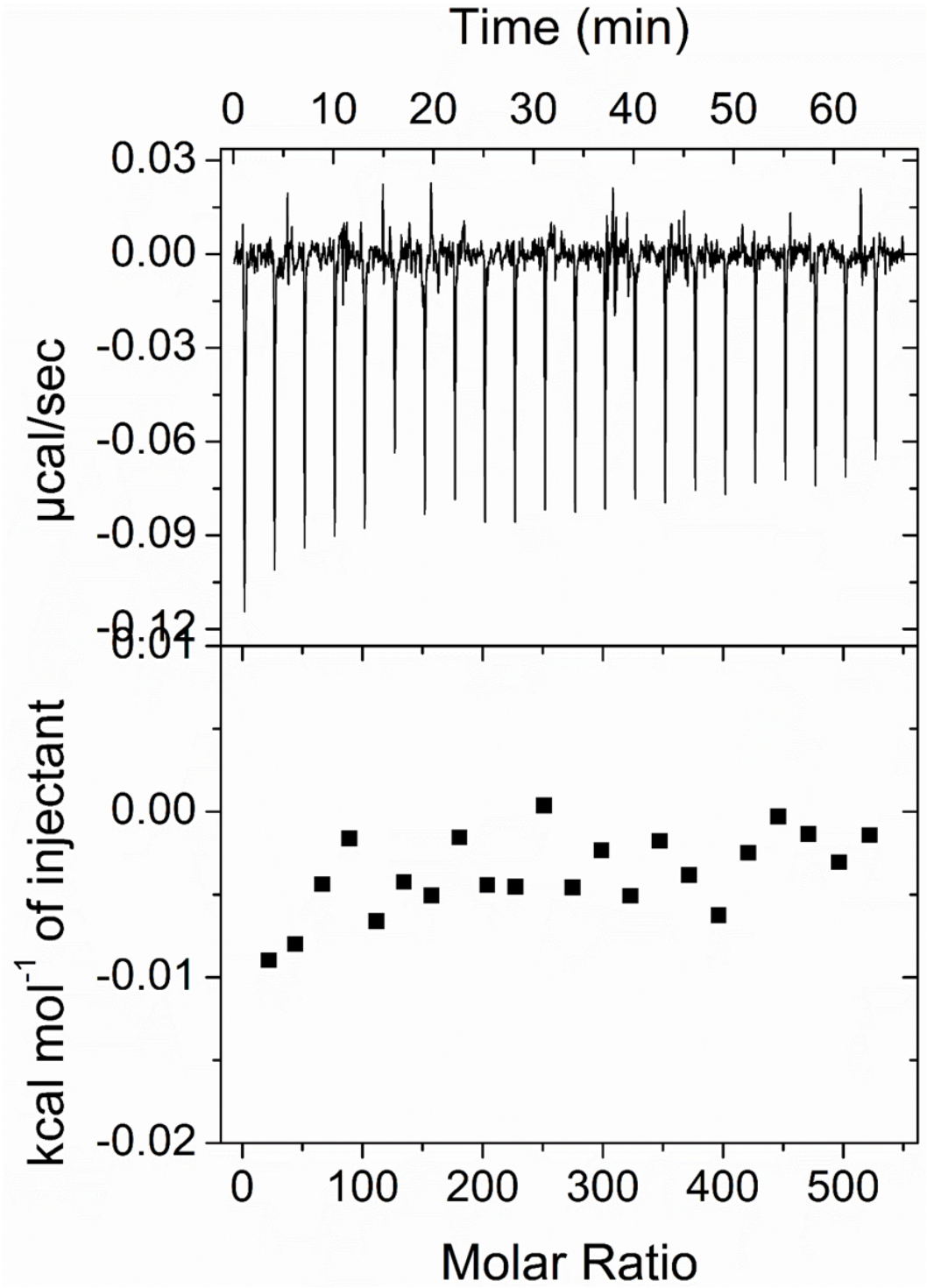

Fig. S80. ITC profiles for the titration of $BPAT^{2+}•2Cl^-$ (0.017 mM in the cell) with galactose (50 mM in syringe) in H_2O. Note: The heat formation is too small to reliably determine the K_a and ΔH.

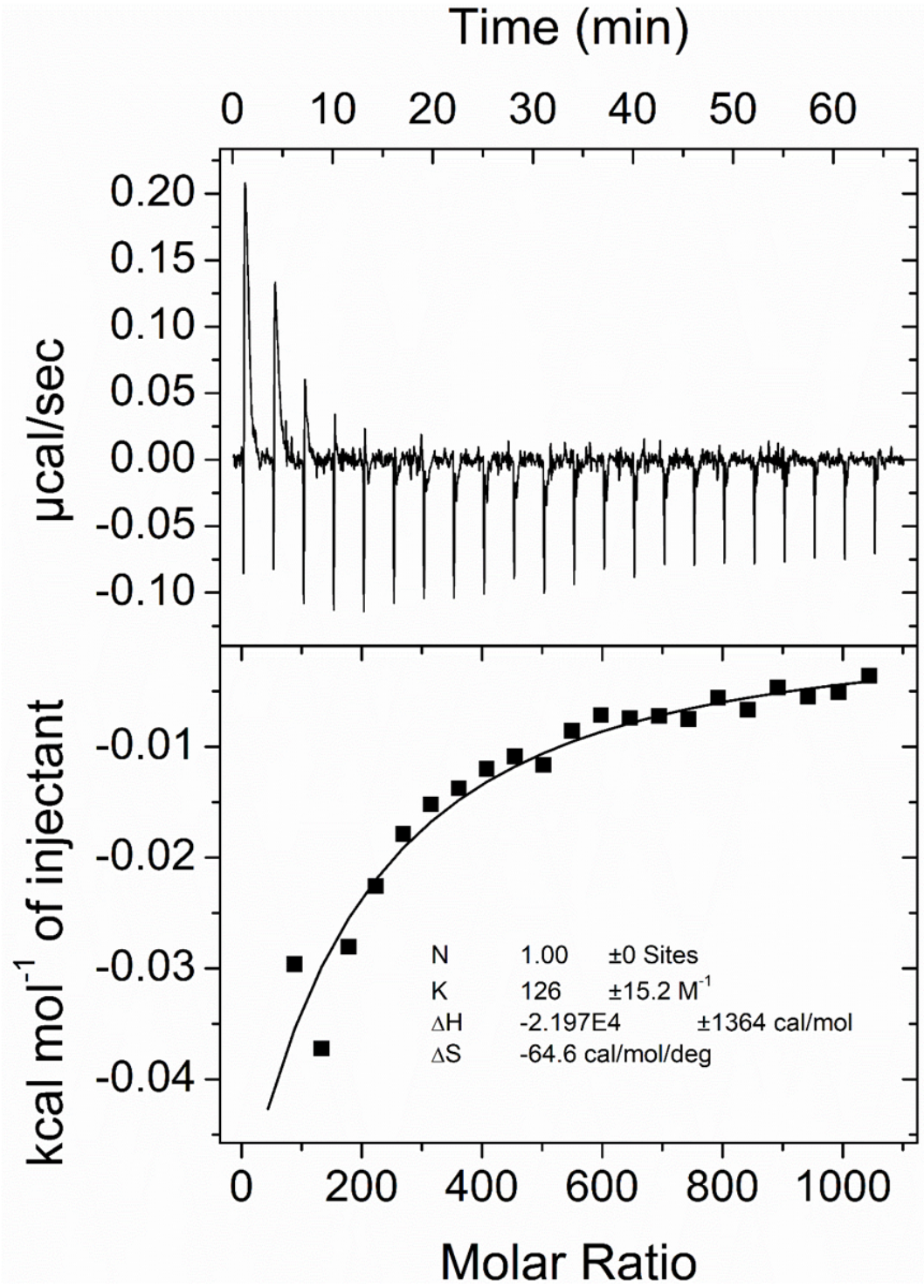

Fig. S81. ITC profiles for the titration of $BPAT^{2+}$•$2Cl^-$ (0.017 mM in the cell) with psicose (100 mM in syringe) in H_2O. The solid line represents the best non-linear fit of the data to a 1:1 binding model (K_a = 126 ± 15 M^{-1}, ΔH = -22 ± 1.4 kcal/mol).

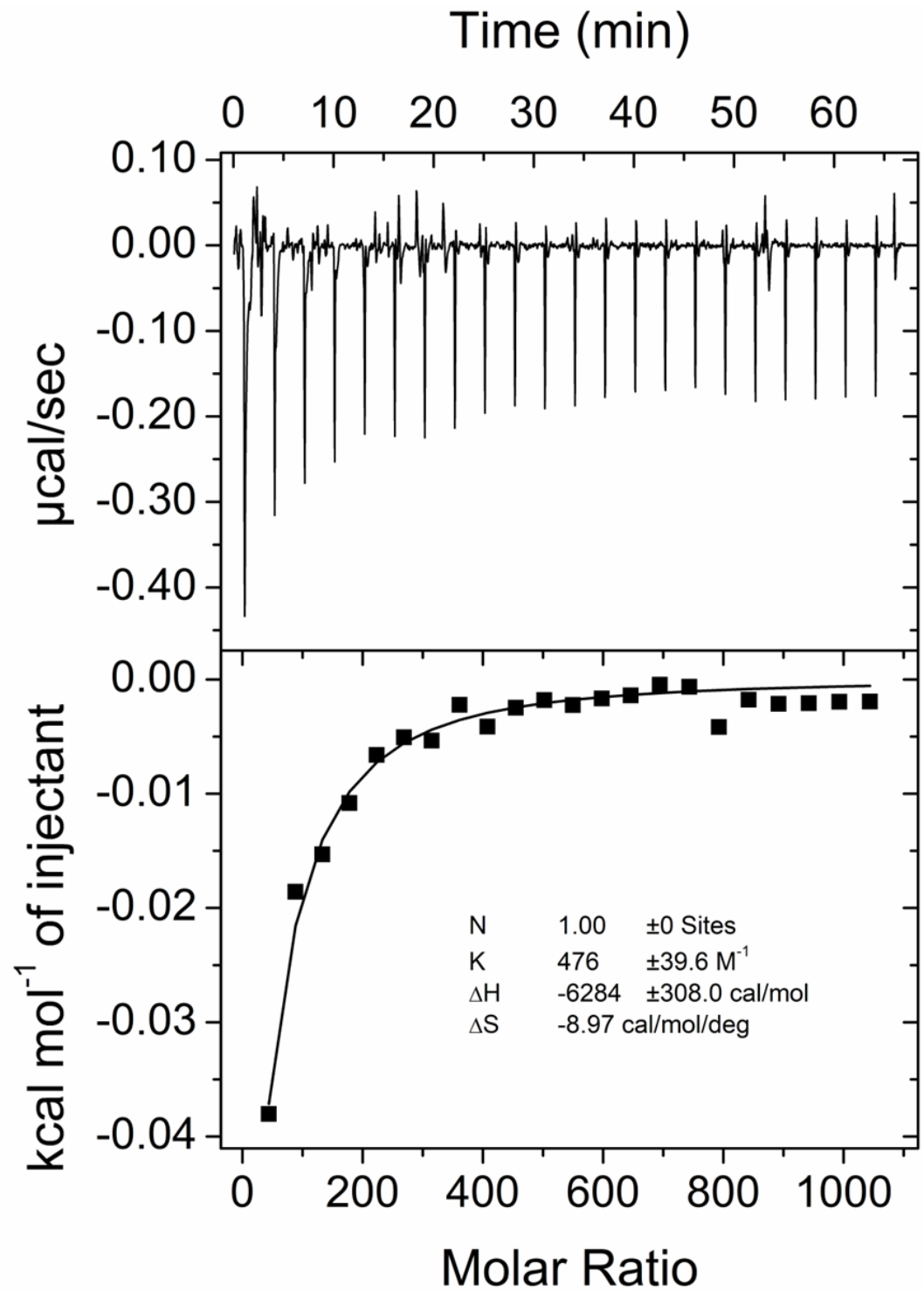

Fig. S82. ITC profiles for the titration of $BPAT^{2+}•2Cl^-$ (0.017 mM in the cell) with maltose (100 mM in syringe) in H_2O. The solid line represents the best non-linear fit of the data to a 1:1 binding model (K_a = 476 ± 40 M^{-1}, ΔH = -6.28 ± 0.31 kcal/mol).

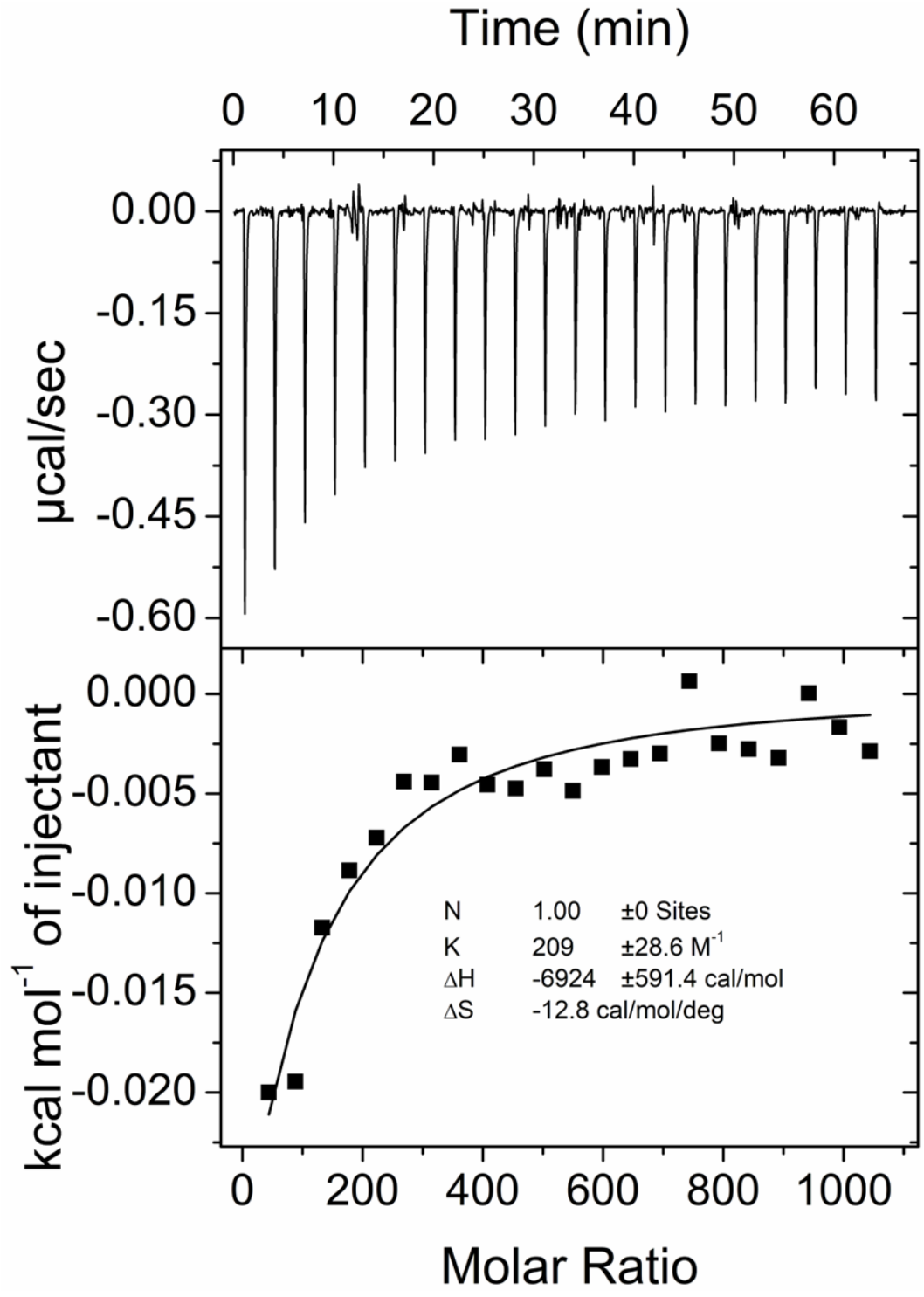

Fig. S83. ITC profiles for the titration of $BPAT^{2+}$•$2Cl^-$ (0.017 mM in the cell) with cellobiose (50 mM in syringe) in H_2O. The solid line represents the best non-linear fit of the data to a 1:1 binding model (K_a = 209 ± 29 M^{-1}, ΔH = -6.92 ± 0.59 kcal/mol).

Sugar binding of $BPAT^{2+}$•$2Cl^-$ in the aggregated state

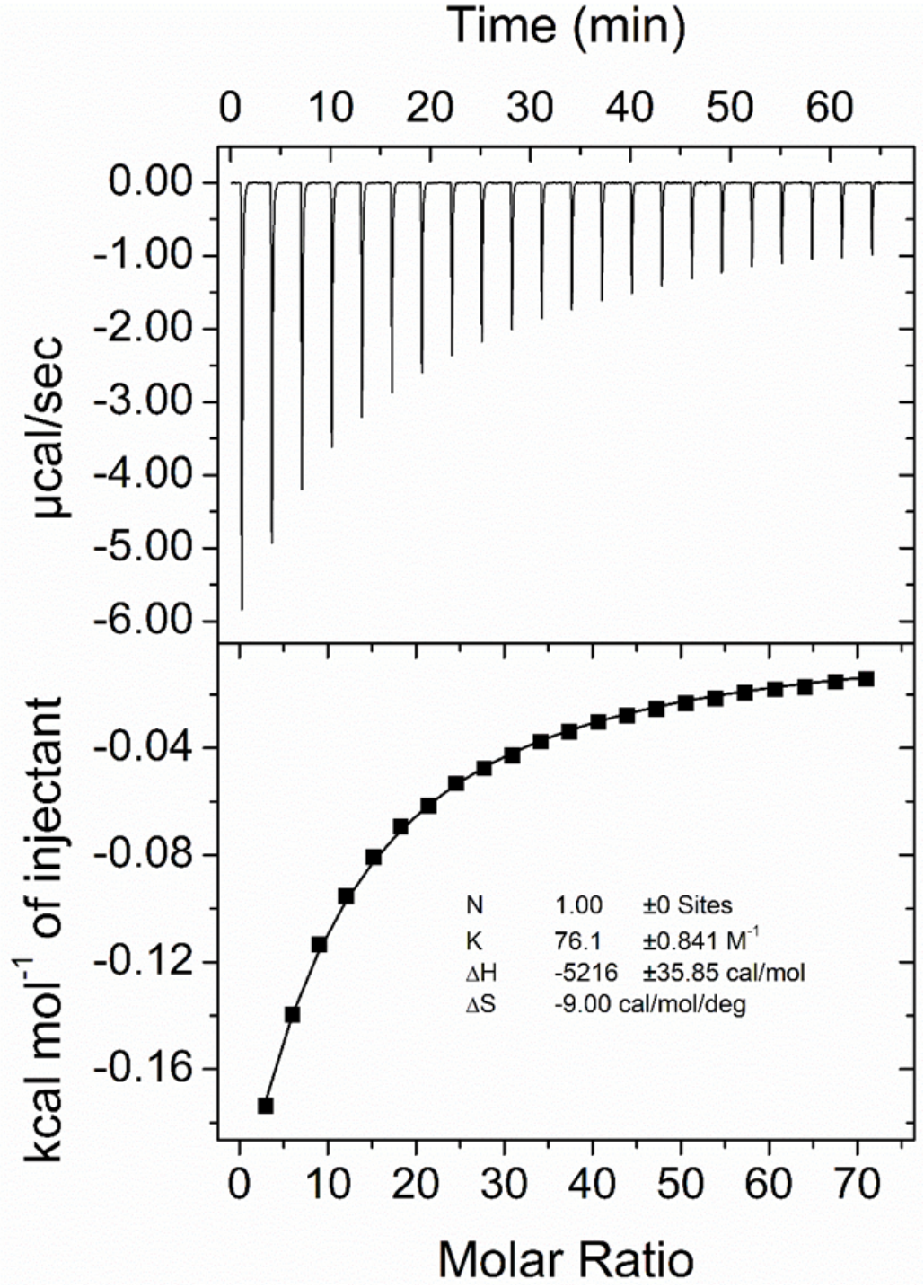

Fig. S84. ITC profiles for the titration of $BPAT^{2+}$•$2Cl^-$ (0.5 mM with NaCl 20 mM in the cell) with glucose (200 mM in syringe) in H_2O. The solid line represents the best non-linear fit of the data to a 1:1 binding model (K_a = 76 ± 0.8 M^{-1}, ΔH = -5.2 ± 0.04 kcal/mol).

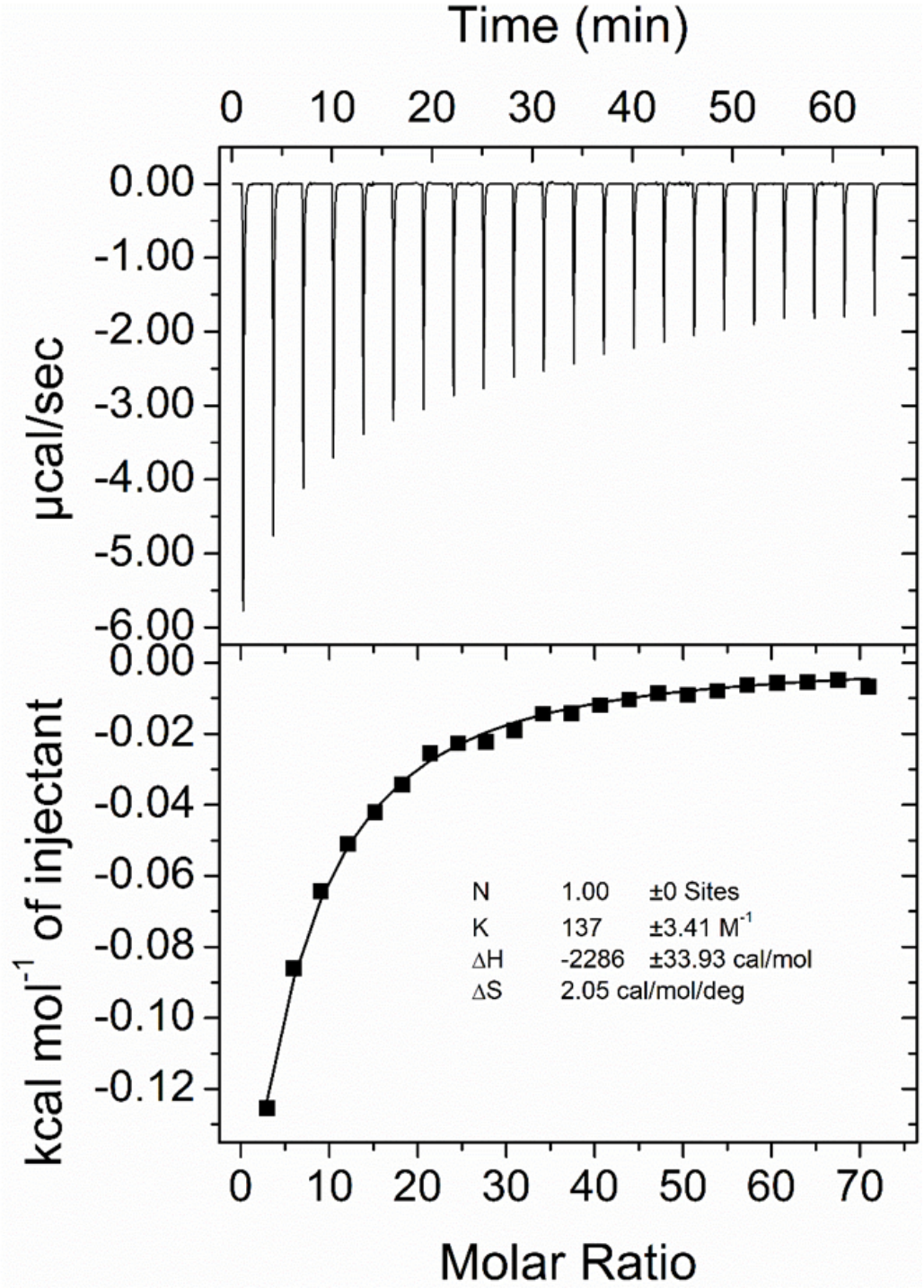

Fig. S85. ITC profiles for the titration of $BPAT^{2+}$•$2Cl^-$ (0.5 mM with NaCl 20 mM in the cell) with Me-β-glucoside (200 mM in syringe) in H_2O. The solid line represents the best non-linear fit of the data to a 1:1 binding model (K_a = 137 ± 3.4 M^{-1}, ΔH = -2.3 ± 0.03 kcal/mol).

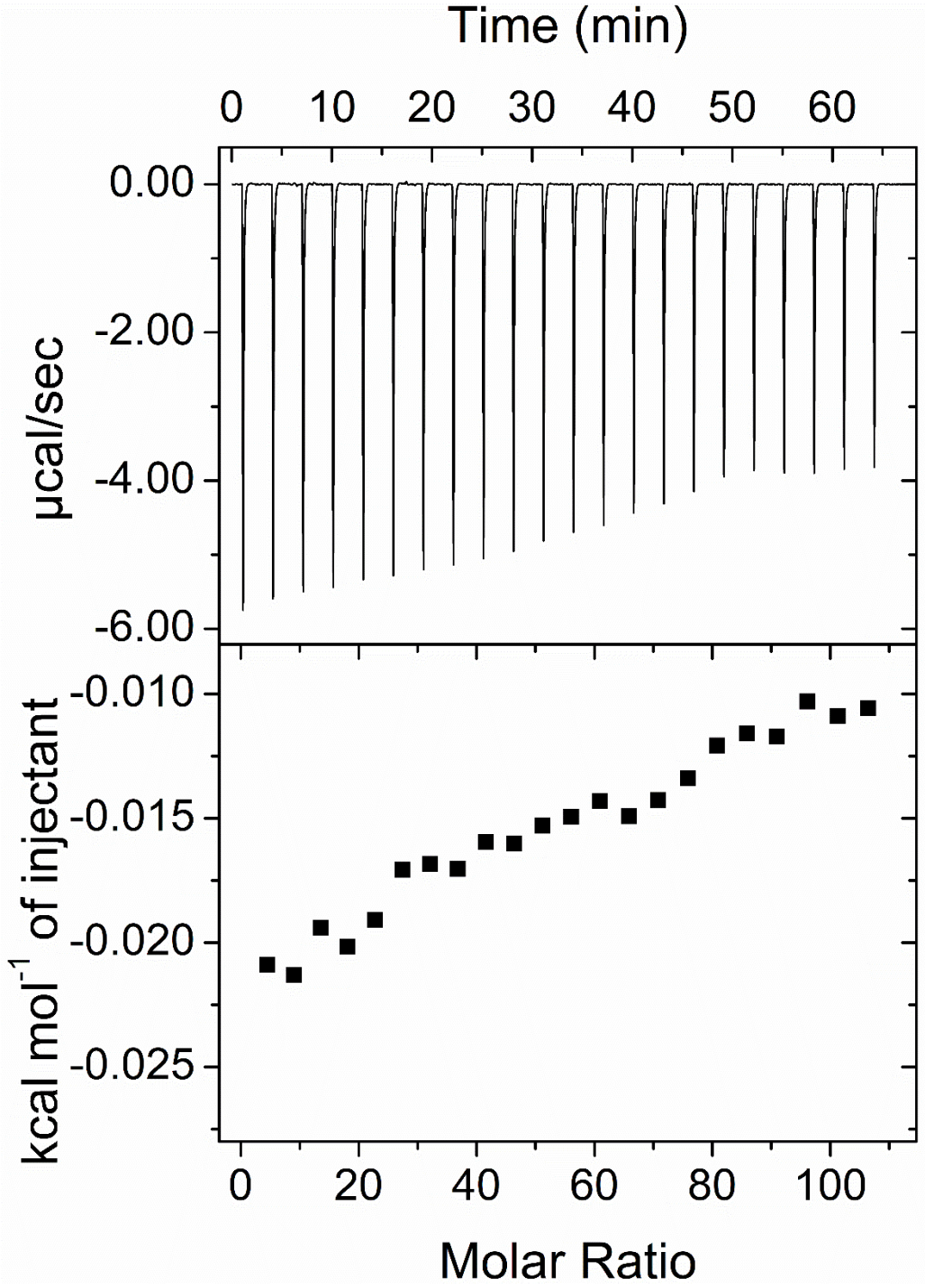

Fig. S86. ITC profiles for the titration of $BPAT^{2+}•2Cl^-$ (0.5 mM with NaCl 20 mM in the cell) with Me-α-glucoside (300 mM in syringe) in H_2O. Note: The heat formation is too small to reliably determine the K_a and ΔH.

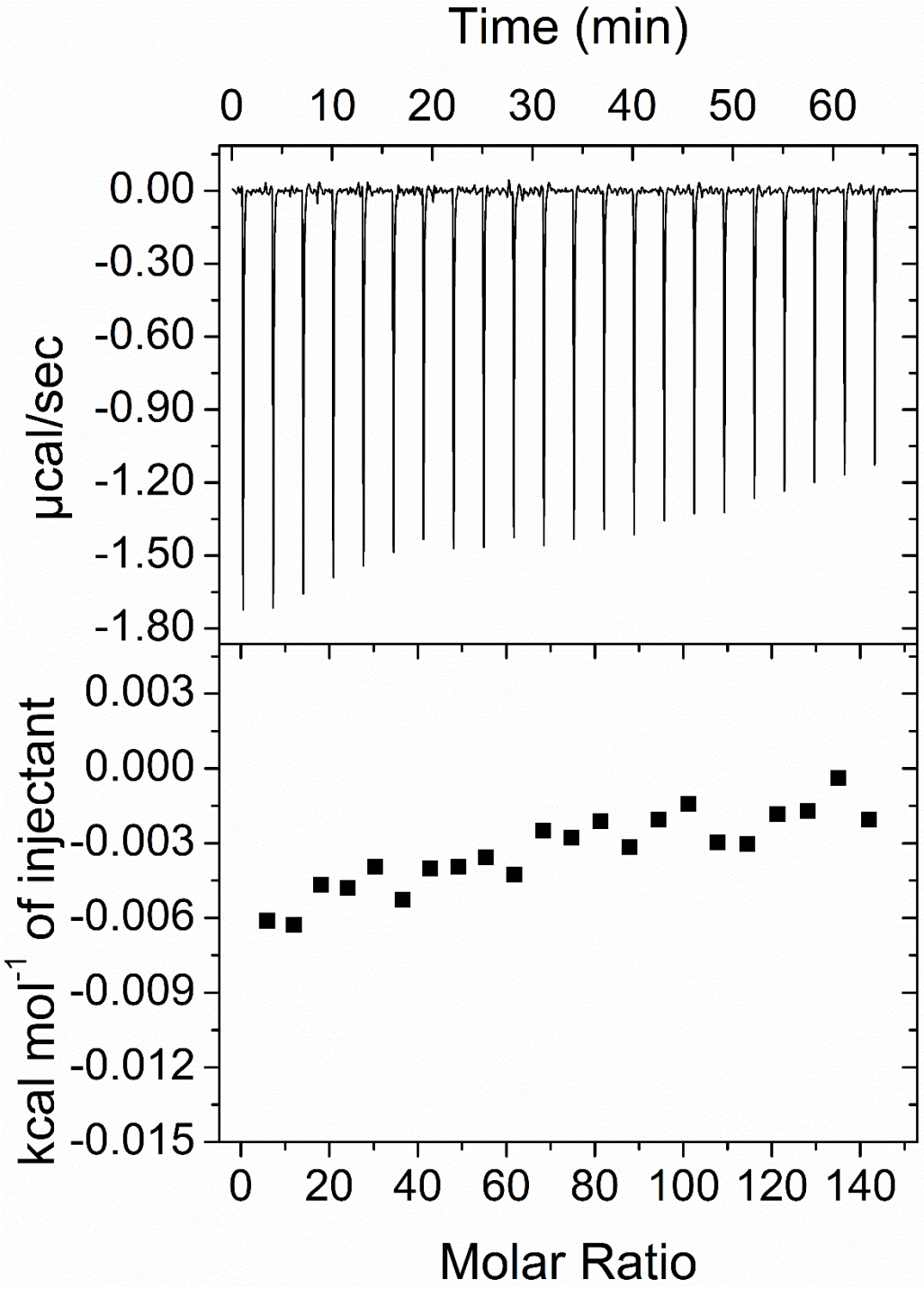

Fig. S87. ITC profiles for the titration of $BPAT^{2+}$•$2Cl^-$ (0.5 mM with NaCl 20 mM in the cell) with mannose (400 mM in syringe) in H_2O. Note: The heat formation is too small to reliably determine the K_a and ΔH.

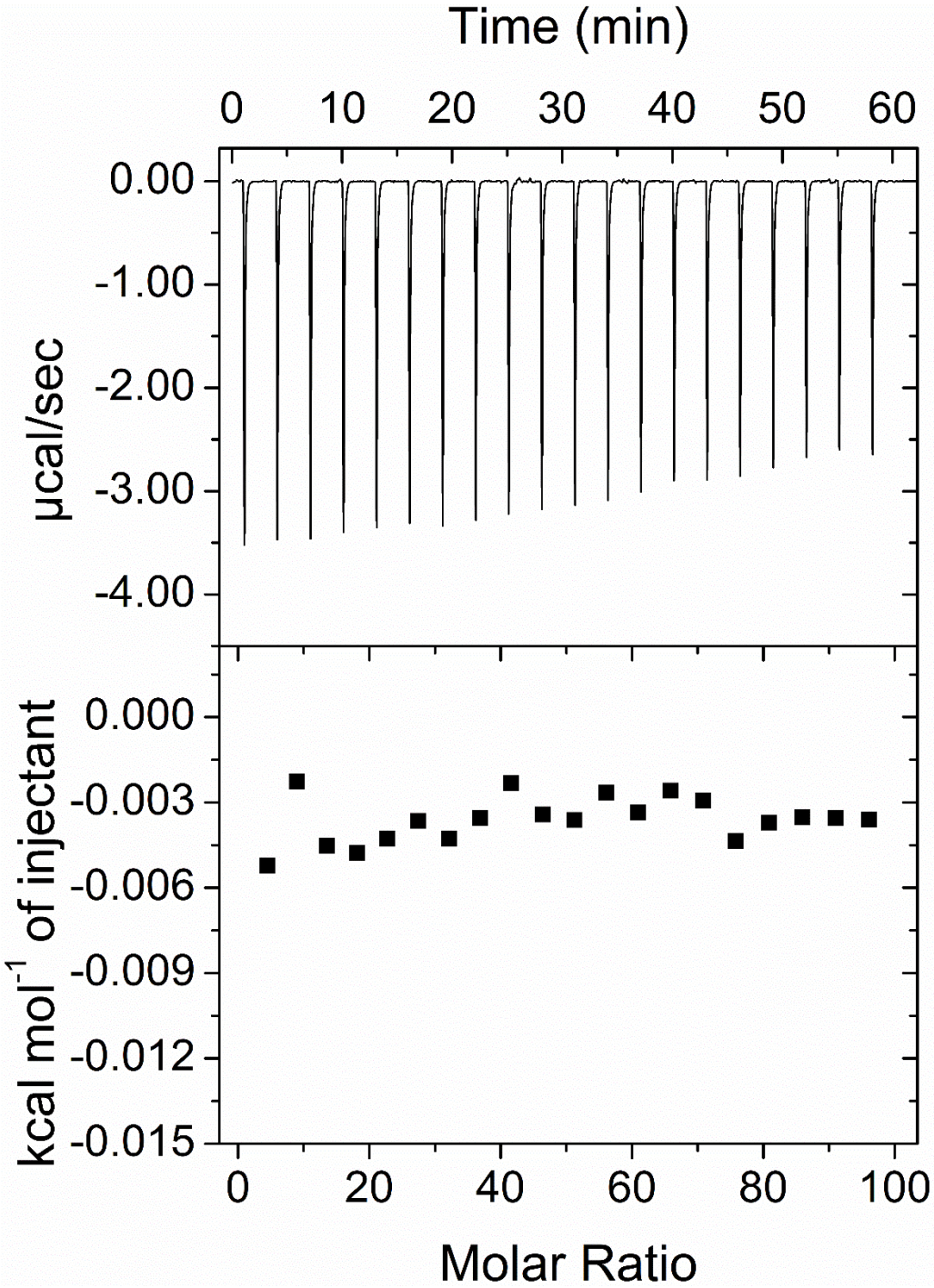

Fig. S88. ITC profiles for the titration of $BPAT^{2+}•2Cl^{-}$ (0.5 mM with NaCl 20 mM in the cell) with GluNAc (300 mM in syringe) in H_2O. Note: The heat formation is too small to reliably determine the K_a and ΔH.

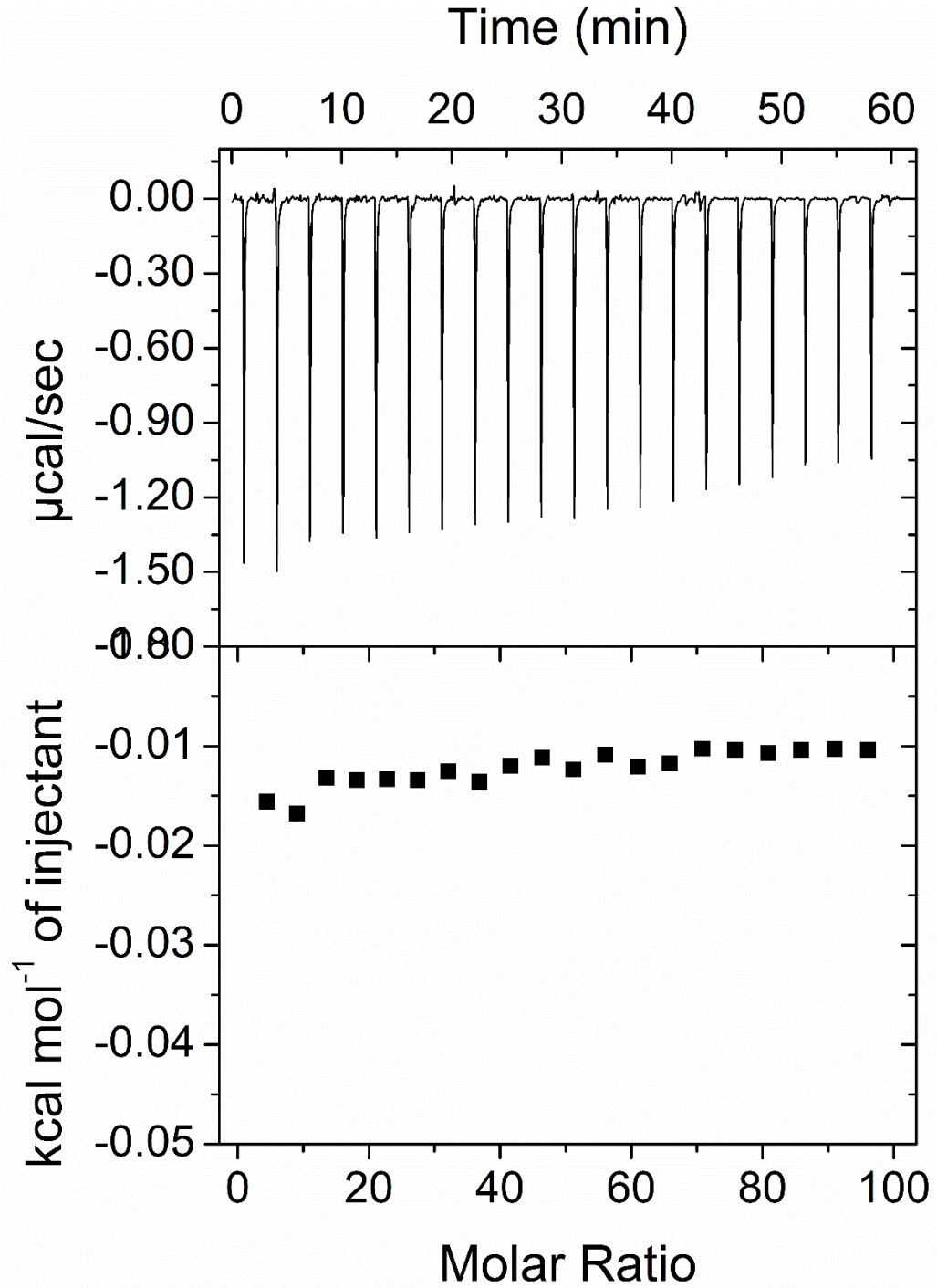

Fig. S89. ITC profiles for the titration of $BPAT^{2+}•2Cl^-$ (0.5 mM with NaCl 20 mM in the cell) with galactose (300 mM in syringe) in H_2O. Note: The heat formation is too small to reliably determine the K_a and ΔH.

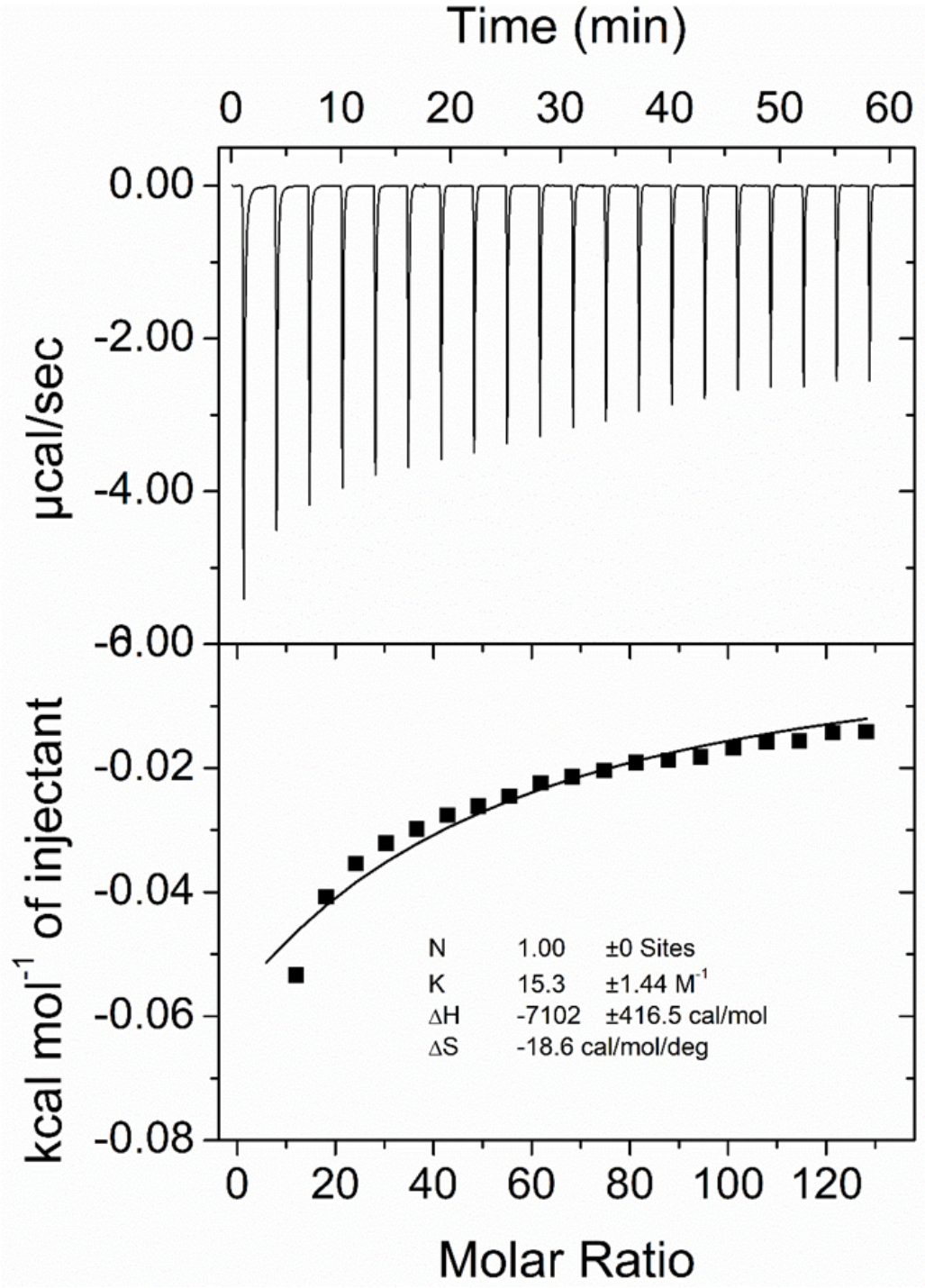

Fig. S90. ITC profiles for the titration of $BPAT^{2+}•2Cl^-$ (0.5 mM with NaCl 20 mM in the cell) with psicose (400 mM in syringe) in H_2O. The solid line represents the best non-linear fit of the data to a 1:1 binding model (K_a = 15 ± 1.4 M^{-1}, ΔH = -7.1 ± 0.4 kcal/mol).

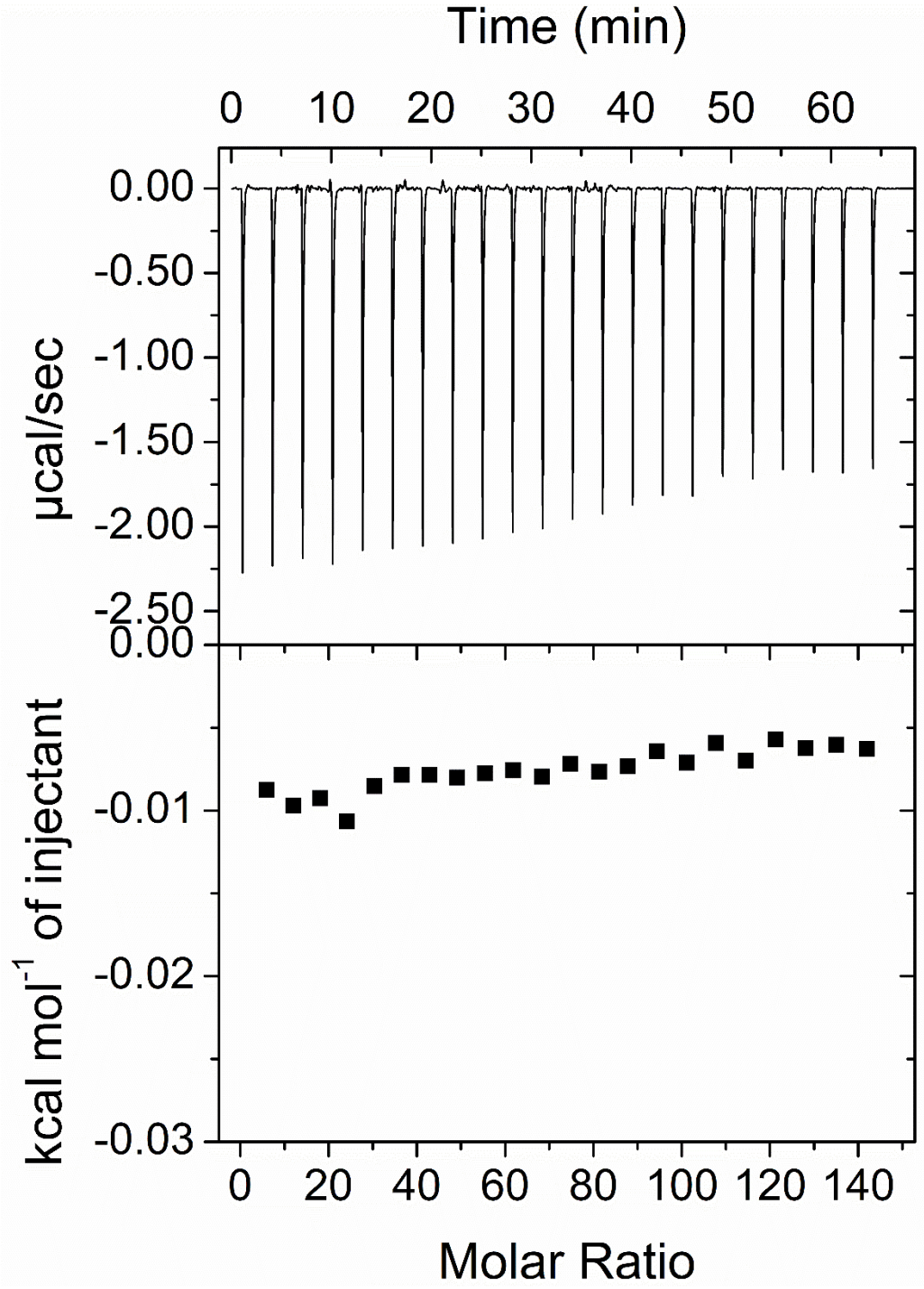

Fig. S91. ITC profiles for the titration of $BPAT^{2+}•2Cl^-$ (0.5 mM with NaCl 20 mM in the cell) with fructose (400 mM in syringe) in H_2O. Note: The heat formation is too small to reliably determine the K_a and ΔH.

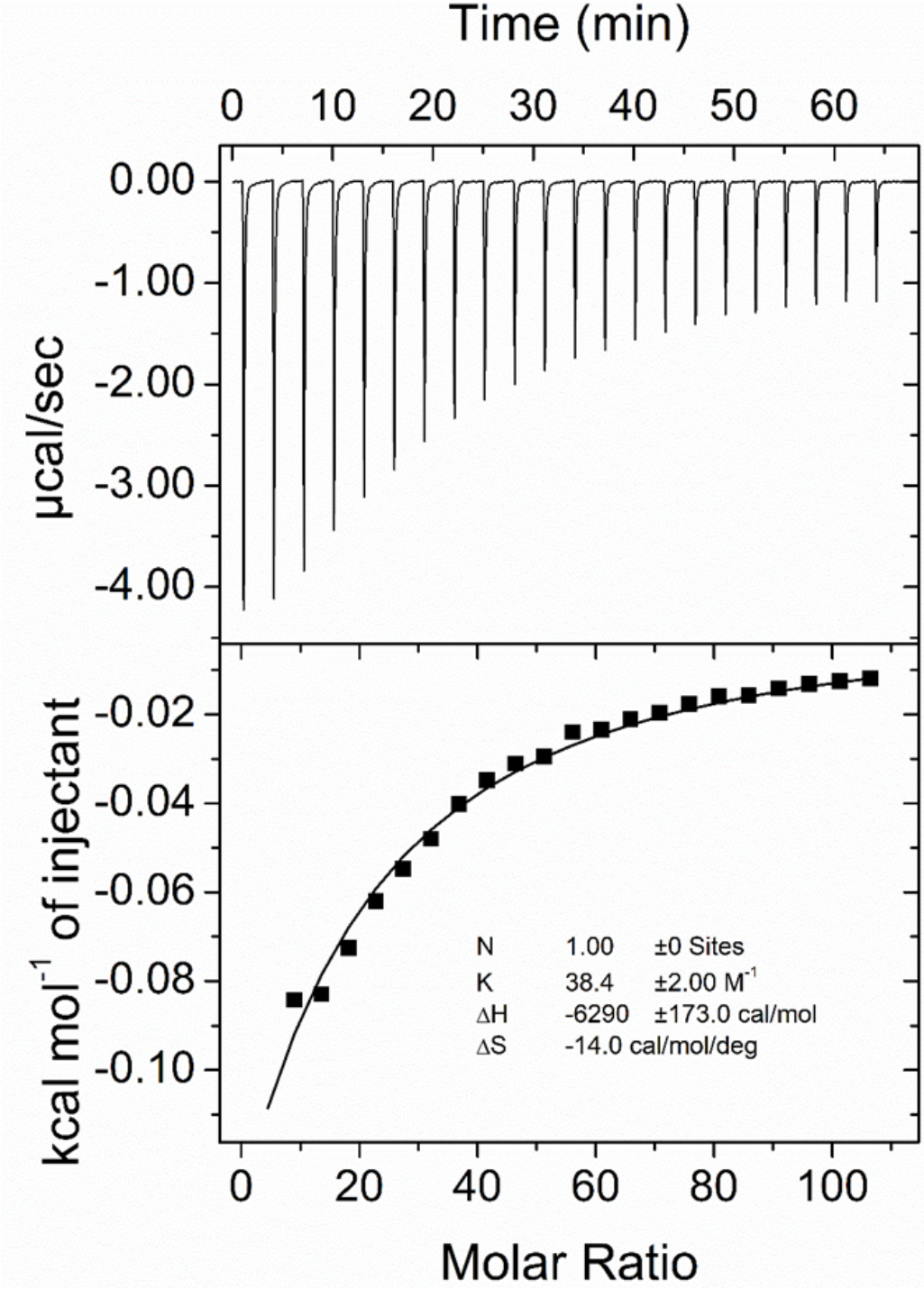

Fig. S92. ITC profiles for the titration of $BPAT^{2+}$•$2Cl^-$ (0.5 mM with NaCl 20 mM in the cell) with maltose (300 mM in syringe) in H_2O. The solid line represents the best non-linear fit of the data to a 1:1 binding model (K_a = 38 ± 2 M^{-1}, ΔH = -6.3 ± 0.2 kcal/mol).

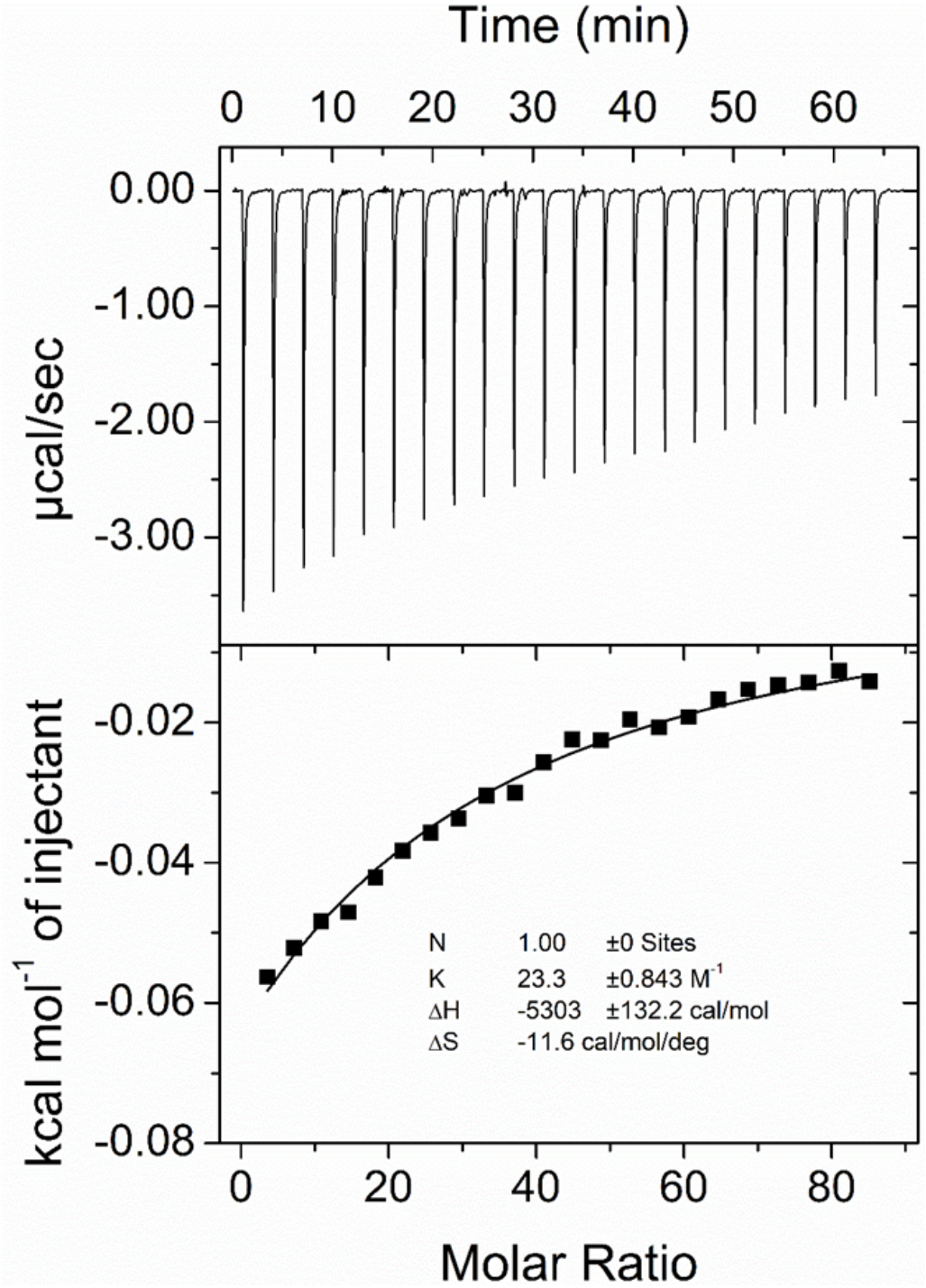

Fig. S93. ITC profiles for the titration of $BPAT^{2+}$•$2Cl^-$ (0.5 mM with NaCl 20 mM in the cell) with cellobiose (240 mM in syringe) in H_2O. The solid line represents the best non-linear fit of the data to a 1:1 binding model (K_a = 23 ± 0.8 M^{-1}, ΔH = -5.3 ± 0.1 kcal/mol).

Glucose binding of $BPAT^{2+}$•$2Cl^-$ in mixed states

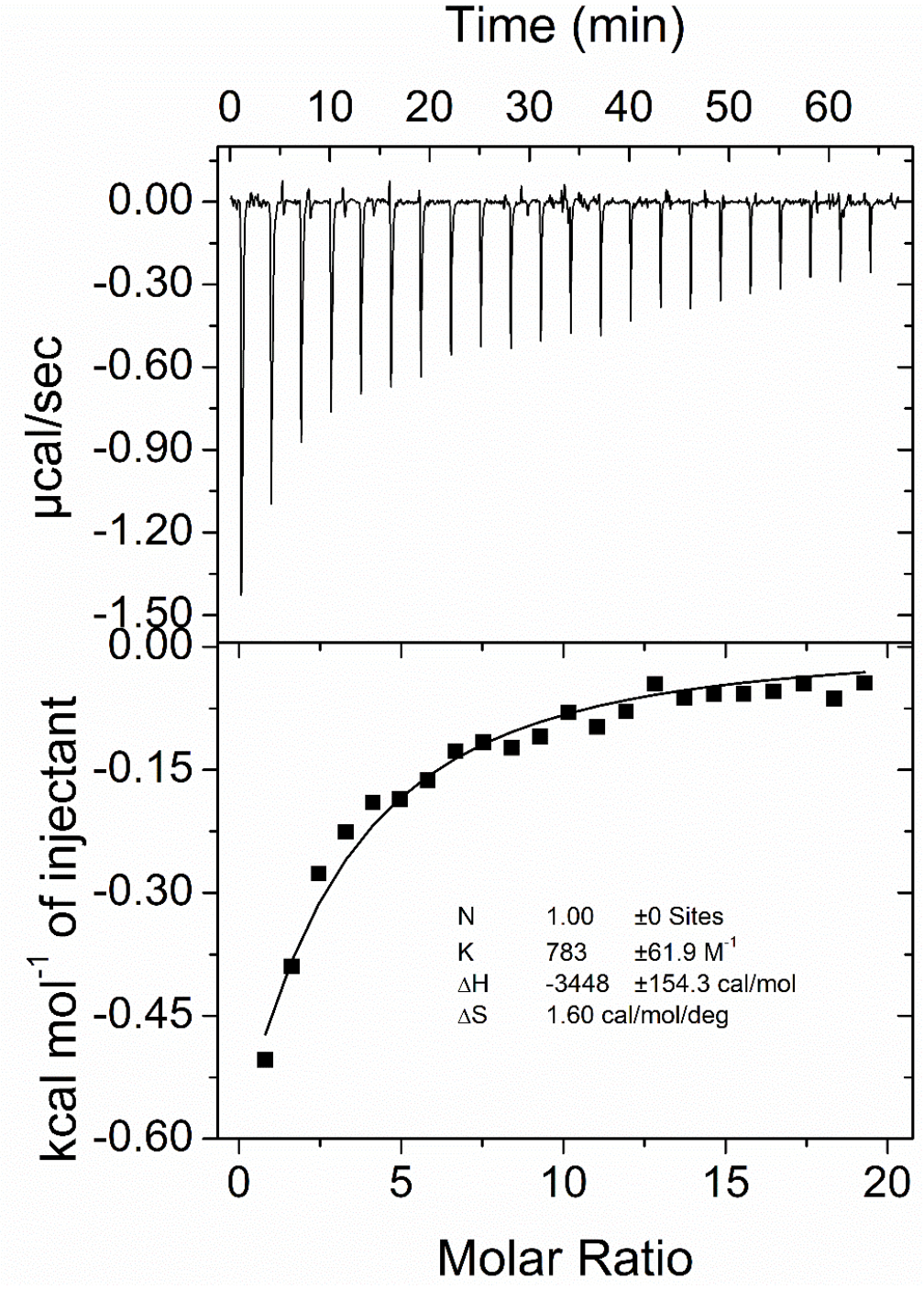

Fig. S94. ITC profiles for the titration of $BPAT^{2+}$•$2Cl^-$ (0.2 mM in the cell) with glucose (25 mM in syringe) in H_2O. The solid line represents the best non-linear fit of the data to a 1:1 binding model (K_a = 783 ± 62 M^{-1}, ΔH = -3.4 ± 0.2 kcal/mol).

6. UV/Vis Absorption Spectroscopy

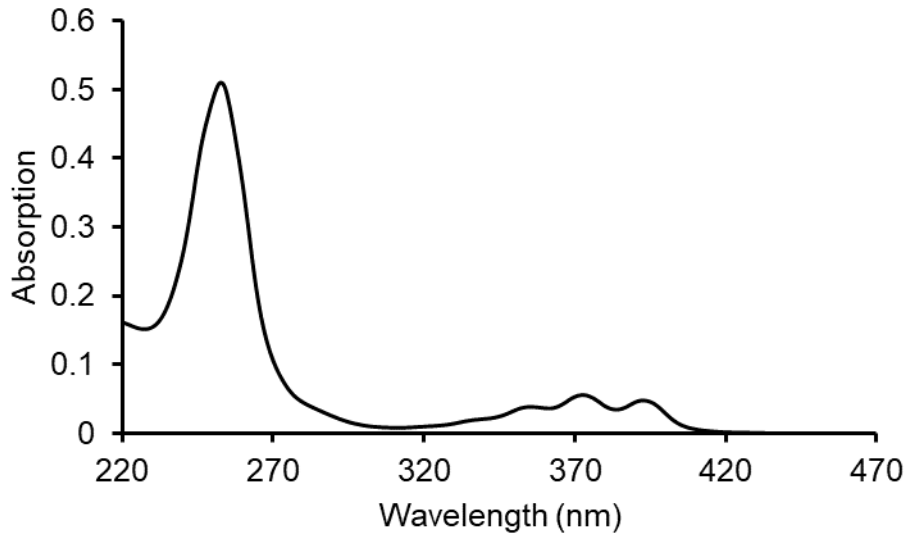

Fig. S95. UV/Vis absorption spectrum of $BPAT^{2+}•2Cl^-$ (2 μM) in water.

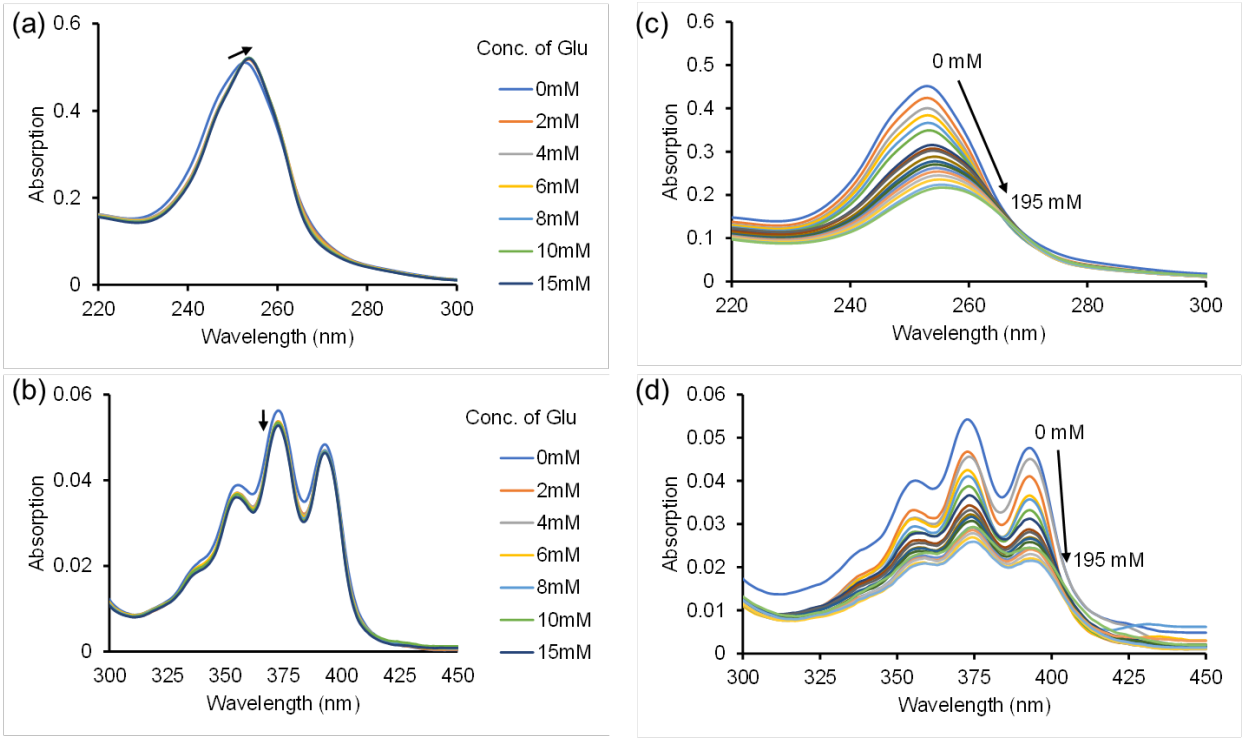

Fig. S96. UV/Vis absorption spectra (a and b) of $BPAT^{2+}•2Cl^-$ (2 μM) titrated with D-glucose in water. UV/Vis absorption spectra (c and d) of $BPAT^{2+}•2Cl^-$ (2 μM) titrated with NaCl in water.

7. Circular Dichroism Spectroscopy

Circular dichroism spectra were collected using the following acquisition parameters:

Measure Range	300 – 200 nm
Data pitch	0.5 nm
Data points	201
D.I.T.	0.5 sec
Bandwidth	1 nm
Scanning speed	200 nm/min
Shutter control	Auto
Accumulations	15
Solvent	DI. water, NaCl solution, or PBS
Cell length	1 cm
Temperature	25 °C

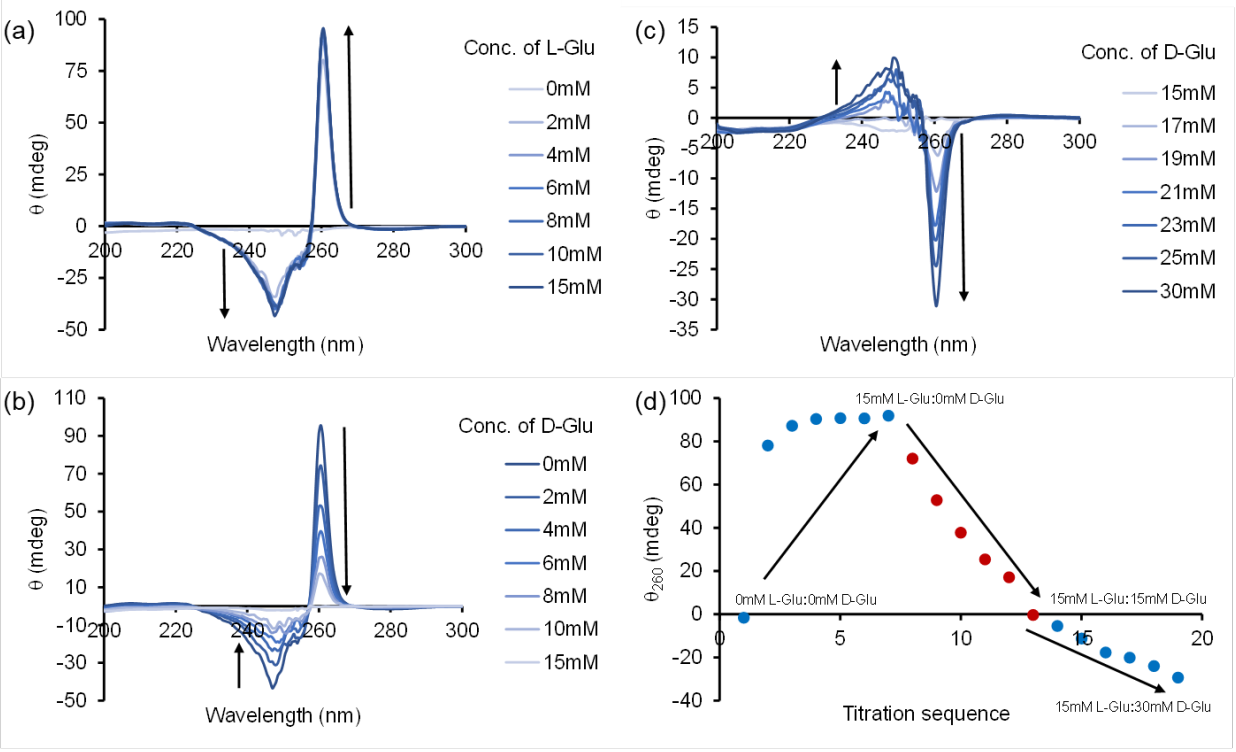

Fig. S97. Titration of $BPAT^{2+}$•$2Cl^-$ with L-glucose followed by addition of D-glucose. (a) CD spectra of $BPAT^{2+}$•$2Cl^-$ (10 μM) with increasing concentration of L-glucose (0–15 mM) in H_2O. (b) CD spectra of $BPAT^{2+}$•$2Cl^-$ (10 μM) in the presence of L-glucose (15 mM) with increasing concentration of D-Glucose (0–15 mM) in H_2O (continued from titration a). (c) CD spectra of $BPAT^{2+}$•$2Cl^-$ (10 μM) in the presence of L-glucose (15 mM) and D-glucose (15 mM) with an increasing concentration of D-glucose (15 mM–30 mM) (continued from titration b). (d) Change of CD signal at 260 nm from the corresponding CD titration experiment (a–c) of $BPAT^{2+}$•$2Cl^-$ with L- and D-glucose in water.

8. X-Ray Single Crystallography Data and Analysis

X-ray data and analysis for glucose ⊂$BPAT^{2+}$•$2Cl^-$ complex (CCDC: 2322713)

X-ray diffraction data were measured on Bruker D8 Venture PHOTON II CMOS diffractometer equipped with a Cu Kα INCOATEC ImuS micro-focus source (λ = 1.54178 Å). Indexing was performed using APEX4[S3] (Difference Vectors method). Data integration and reduction were performed using SaintPlus [S4]. Absorption correction was performed using the multi-scan method implemented in SADABS[S5]. The space group was determined using XPREP implemented in

APEX3[3]. The structure was solved using SHELXT[S6] and refined using SHELXL-2019/1[S7] (full-matrix least-squares on F2) through the OLEX2 interface program[S8]. The ellipsoid plot was made with Platon[S9]. Due to the disorder of H_2O/Cl^-, the assignment of Cl63 and Cl64 to electron density was tentative. Some of the disordered atoms were refined as O (tentatively H_2O).

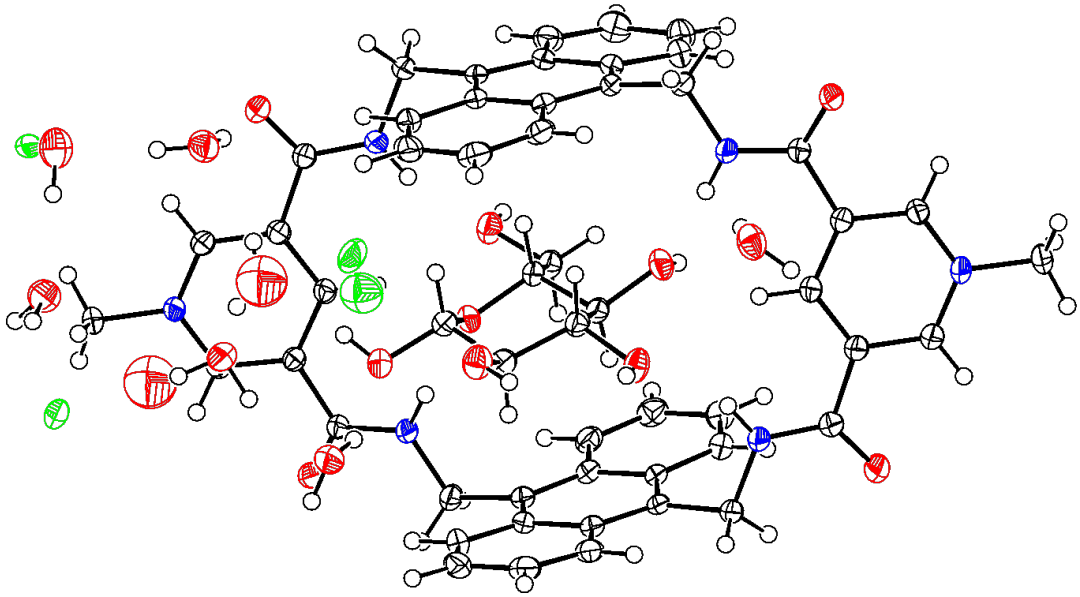

Fig. S98. The ellipsoid plot of glucose ⊂$BPAT^{2+}$•$2Cl^-$. Anisotropic displacement parameters were drawn at a 50% probability level.

Table S2 Crystal data and structure refinement for Glucose-BPAT.

Identification code	Glucose-BPAT
Empirical formula	$C_{54}H_{62.55}Cl_2N_6O_{15.81}$
Moiety formula	$C_{48}H_{40}N_6O_4$, $C_6H_{12}O_6$, 2(Cl), 5.28(H_2O), 0.54(O)
Formula weight	1119.59
Temperature/K	100.00
Crystal system	monoclinic
Space group	C2
a/Å	27.4244(4)
b/Å	13.2628(2)
c/Å	16.6870(2)
α/°	90
β/°	121.7740(10)
γ/°	90
Volume/$Å^3$	5159.84(13)
Z	4
$\rho_{calc}g/cm^3$	1.441
μ/mm^{-1}	1.800
F(000)	2356.0
Crystal size/mm^3	0.04 × 0.04 × 0.02
Radiation	CuKα (λ = 1.54178)
2Θ range for data collection/°	6.23 to 158.148
Index ranges	$-34 \leq h \leq 34$, $-16 \leq k \leq 16$, $-19 \leq l \leq 21$
Reflections collected	55151
Independent reflections	10690 [R_{int} = 0.0415, R_{sigma} = 0.0319]
Data/restraints/parameters	10690/24/791
Goodness-of-fit on F^2	1.048
Final R indexes [I>=2σ (I)]	R_1 = 0.0405, wR_2 = 0.1132
Final R indexes [all data]	R_1 = 0.0424, wR_2 = 0.1150
Largest diff. peak/hole / e $Å^{-3}$	0.61/-0.33
Flack parameter	0.056(4)

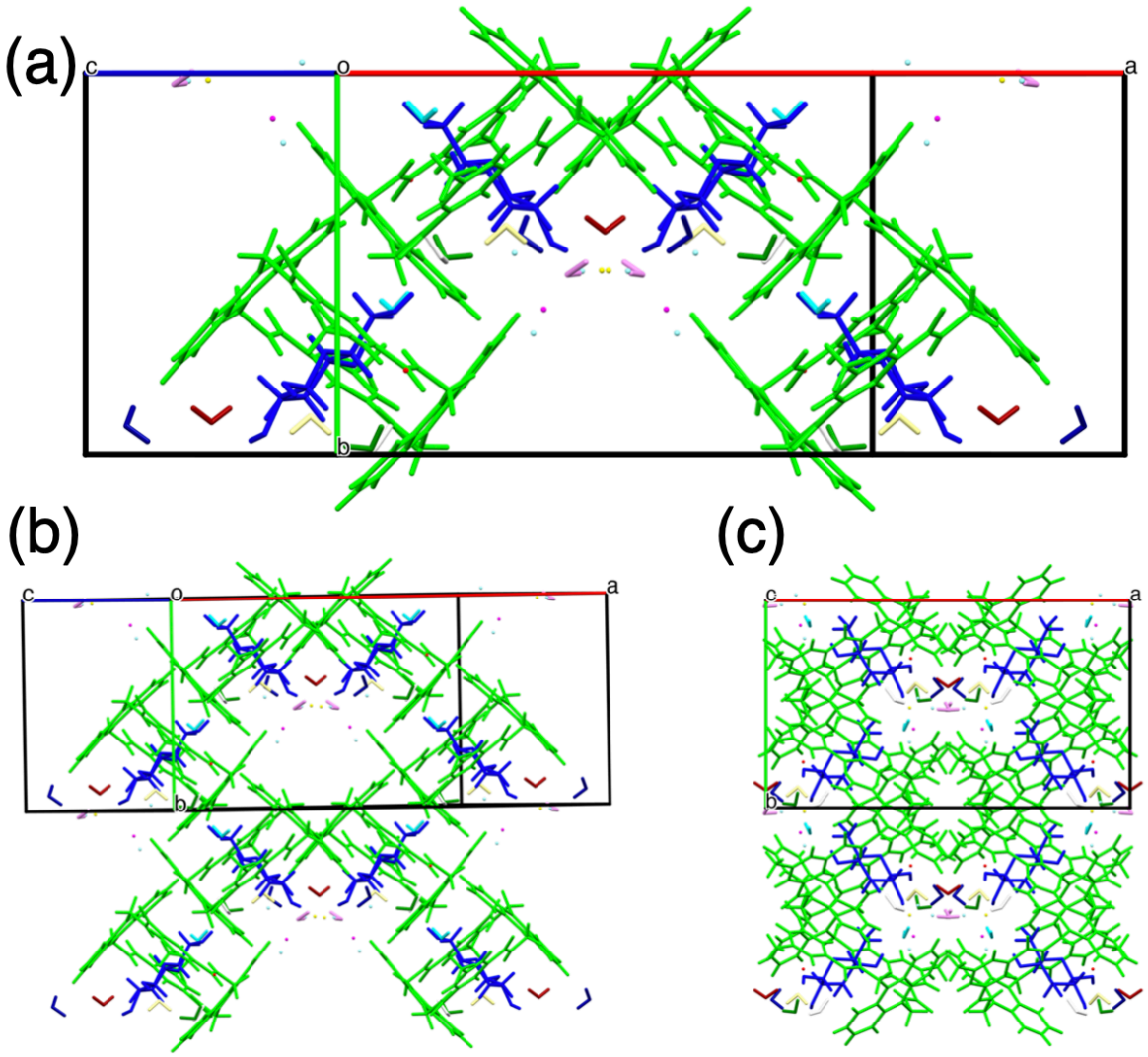

Fig. S99. (a) Side view of the unit cell along the c axis showing four glucose ⊂$BPAT^{2+}$•$2Cl^{-}$ packed in the same symmetry. (b) Side and (c) front view along the c axis of the unit cell showing the possible packing structure of glucose ⊂$BPAT^{2+}$•$2Cl^{-}$ observed in solution. Molecules were colored by symmetry equivalent, indicating all glucose ⊂$BPAT^{2+}$•$2Cl^{-}$ complexes have the same chemical environment.

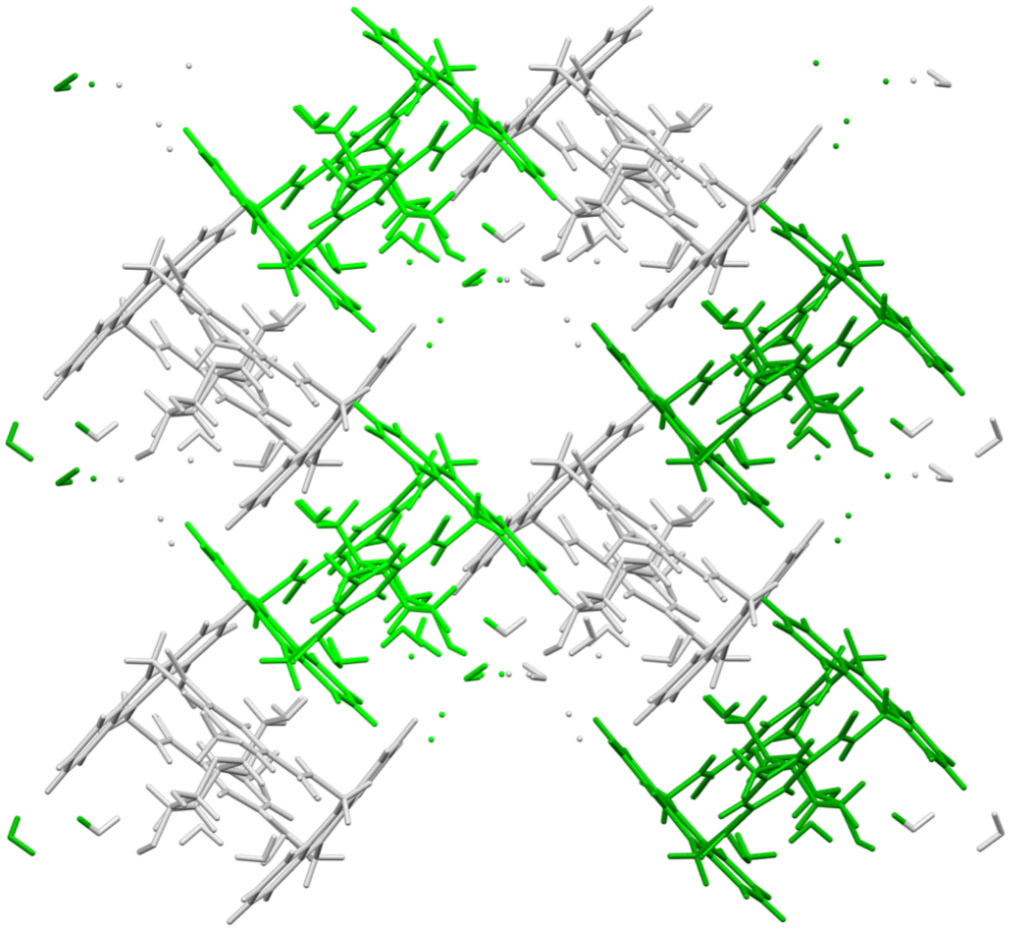

	Number	Symm.Op.	Description	Detailed Description
1	1	x,y,z	Identity	Identity
2	2	-x,y,-z	Rotation axis (2-fold)	2-fold rotation axis with direction [0,1,0] at 0,y,0
3	3	1/2+x,1/2+y,z	Centring vector	Centring vector [1/2,1/2,0]
4	4	1/2-x,1/2+y,-z	Screw axis (2-fold)	2-fold screw axis with direction [0,1,0] at 1/4,y,0 with screw component [0,1/2,0]

Fig. S100. Side view along the c axis of the unit cell showing possible macrocycle packing in aggregated state of $BPAT^{2+}•2Cl^{-}$ observed in solution. Molecules were colored by symmetry operations, revealing the highly symmetric feature of $BPAT^{2+}•2Cl^{-}$ packed in the unit cell.

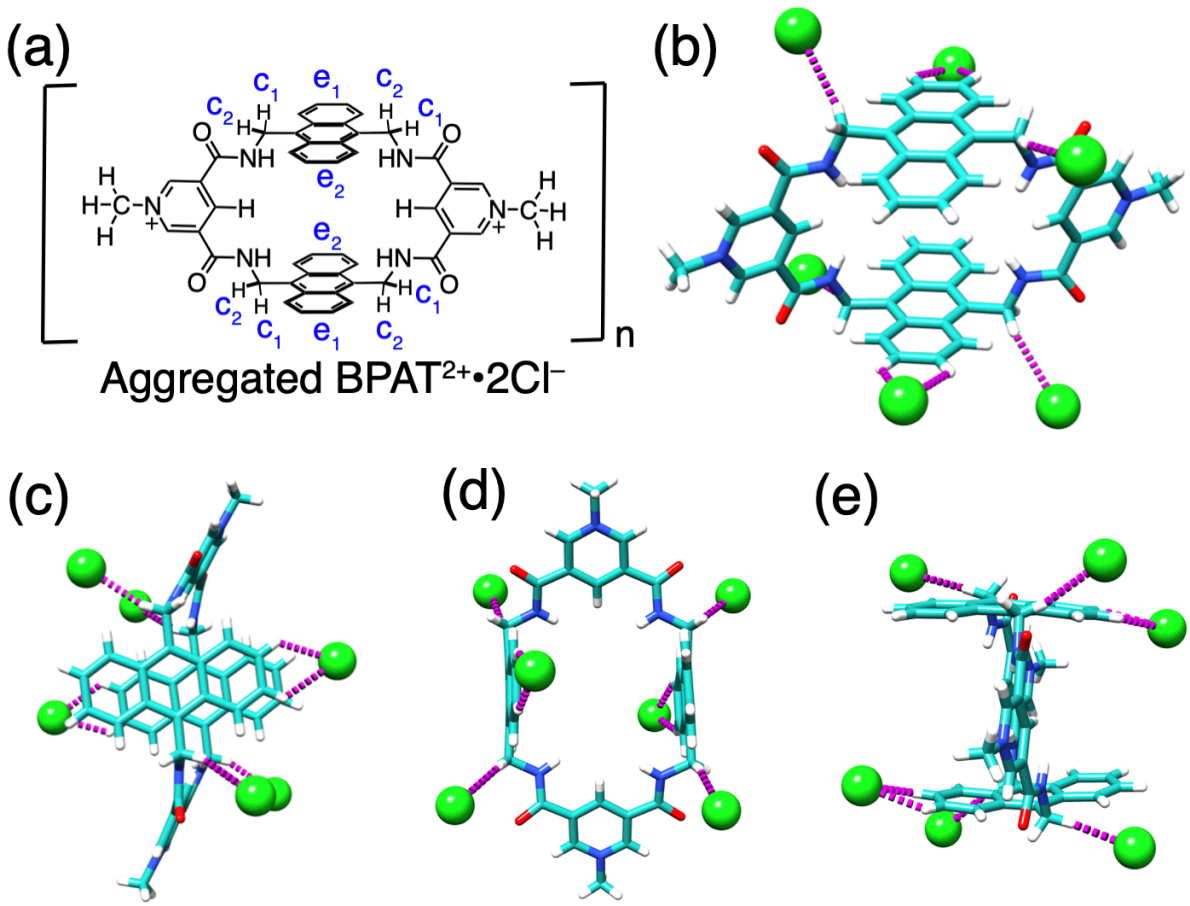

Fig. S101. (a) The structural formula of $BPAT^{2+}$•$2Cl^-$ highlighting two sets of peaks for protons c and e observed by ^1H NMR in the aggregated state. (b) Side-on, (c) front, (d) side, and (e) top view of $BPAT^{2+}$•$2Cl^-$ in the crystal structure of glucose ⊂$BPAT^{2+}$•$2Cl^-$, showing the hydrogen bonding between Cl^- and protons c and e.

9. Atomic Force Microscopy Imaging

Atomic force microscopy (AFM) imaging experiments were performed using a Bruker MultiMode 8 platform in tapping mode. A 40 μL sample of $BPAT^{2+}$·$2Cl^-$ in water was drop-cast onto a freshly cleaved mica surface. The solution was incubated for 5 minutes to allow the deposition of the macrocycle or its aggregated nanoparticles onto the mica surface. After incubation, the sample was rapidly dried with nitrogen gas before proceeding with AFM imaging.

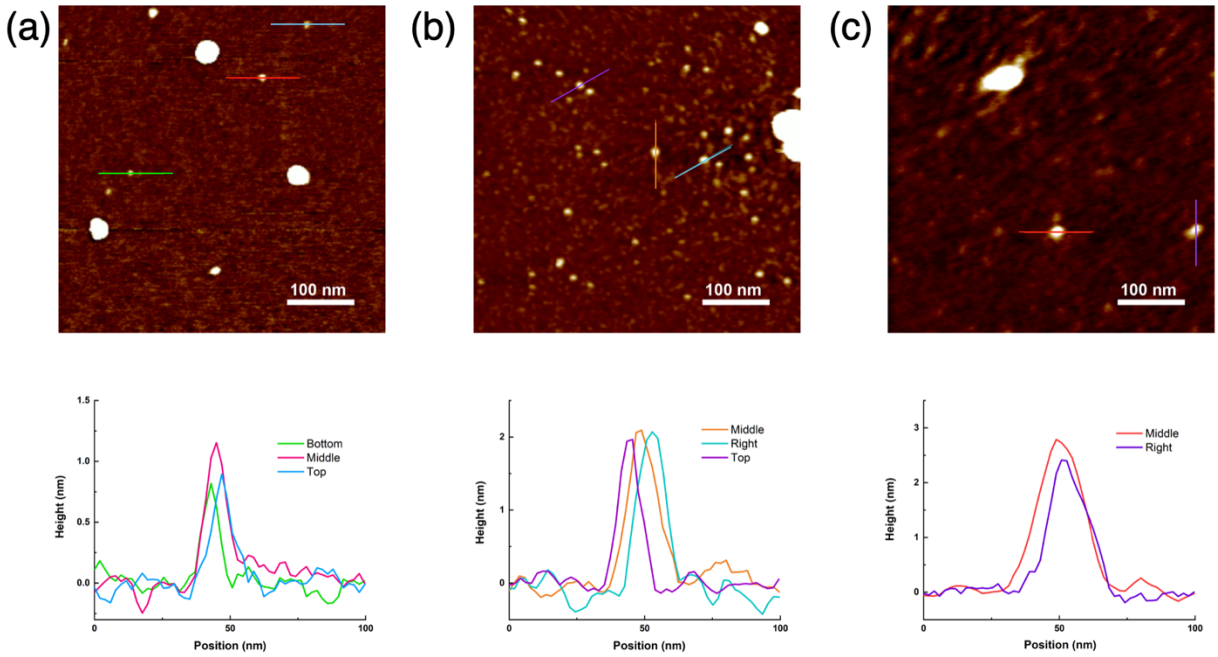

Fig. S102. AFM imaging (top) and particle height (bottom) for samples containing $BPAT^{2+}$•$2Cl^{-}$ solutions at concentrations of (a) 0.02 mM, (b) 0.2 mM, and (c) 0.8 mM. The colored lines in each AFM image indicate the regions measured for particle height.

Discussion on the results of AFM imaging:

Due to the well-known broadening effect of AFM imaging, particle dimensions in the x-y plane are not accurate (or significantly overestimated) and, therefore, not used for analyzing the particle size. Given AFM accurately measures the z dimension (i.e., the height of the particle), we analyzed the heights of the particles at different concentrations ((a) 0.02 mM, (b) 0.2 mM, and (c) 0.8 mM) and observed that higher concentrations yield larger size of the particle (or aggregate), which is consistent with the results of DOSY experiments.

10. Computational Analysis

Structural Optimization and Binding Energy Analysis

The XYZ coordinates for the calculations were extracted from the X-ray single crystal data. All optimizations and single-point calculations were performed with density functional theory (DFT) in the Orca program[S10] (version 5.0.3) using the Becke ’88 exchange and Lee-Yang-Parr correlation (BLYP) functional[S11], the

Ahlrich's double zeta Def2-SVP basis sets[S12] with geometrical counterpoise (gCP) scheme[S13], and Grimme's third-generation dispersion correction[S14] with Beck Johnson damping (D3BJ). In order to speed up the DFT optimizations, the Coulomb integral[S15] and numerical chain-of-sphere integration[S16] for the HF exchanges (RIJCOSX) method was applied with the Def2/J auxiliary basis (AuxJ) [S17]. All optimizations were performed in a water continuum with the Conductor-like Polarizable Continuum Model (CPCM) in Orca. Frequency calculations of the resulting optimized structures reveal no imaginary frequency, suggesting the optimized structures were in local energy minima.

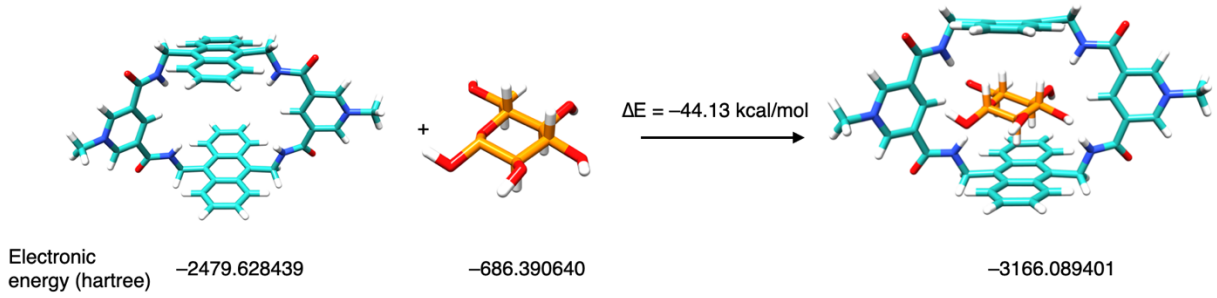

Fig. S103. Binding energy of glucose⊂ $BPAT^{2+}$ in H_2O based on optimized structure.

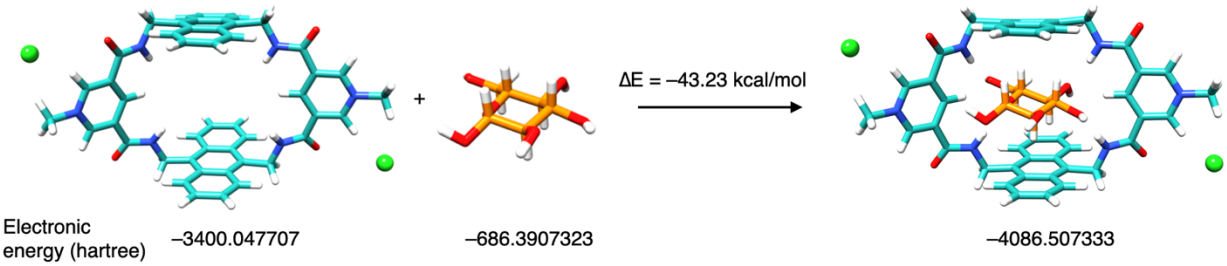

Fig. S104. Binding energy of glucose⊂ $BPAT^{2+}$•$2Cl^-$ in H_2O based on optimized structure.

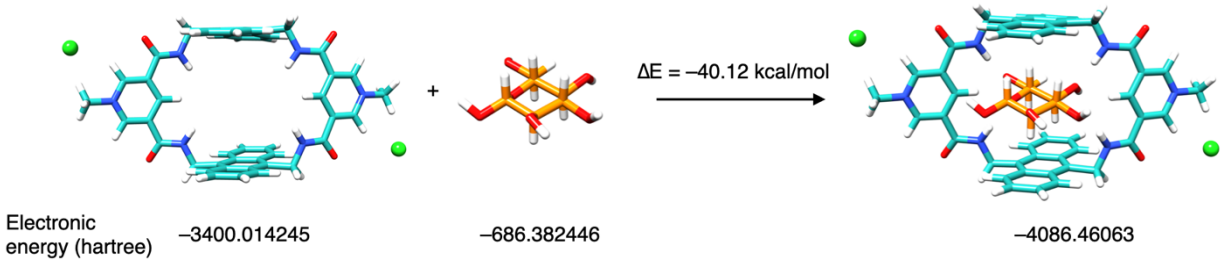

Fig. S105. Binding energy of glucose ⊂$BPAT^{2+}$•$2Cl^-$ in H_2O based on solid-state structure.

Electrostatic Potential Map:

Single point energy calculations of $BPAT^{2+}$ and $BPAT^{2+}$•$2Cl^-$ were performed at BLYP-SVP level. The resulting wavefunction files were used as input for calculating electron density and total electrostatic potential using the Multiwfn 3.6 program[S18] based on computerized optimized code[S19, S20]. The results were visualized using Chimera software.[S21]

Visualization of Noncovalent Interactions

Independent Gradient Model (IGM) analysis[S22] is an approach to identifying and visualizing intermolecular interactions. Strong polar attractions and weak van der Waals contacts are visualized as an isosurface with blue and green colors. X-ray single crystal structures were used as input files. The binding surface was calculated by the Multiwfn 3.6 program[S18] through function 20 (visual study of weak interaction) and visualized by Chimera software[S21].

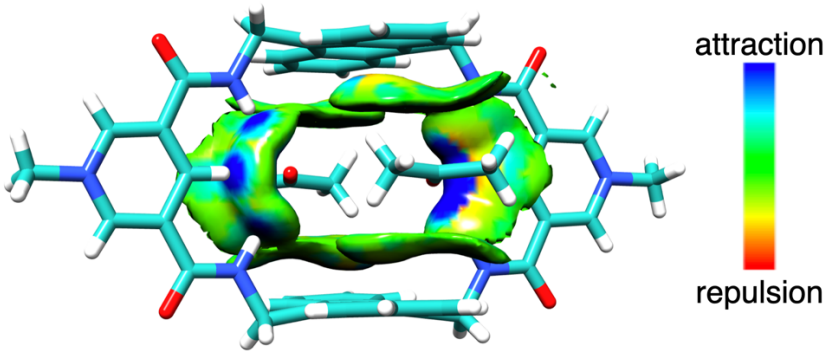

Fig. S106. IGM analysis of 2acetone⊂$BPAT^{2+}$ showing a noncovalent interaction isosurface of $\delta g^{inter} = 0.005$ a.u; color coding in the electron density range of $-0.05 < \text{sign}(\lambda_2)\rho < +0.05$ a.u.

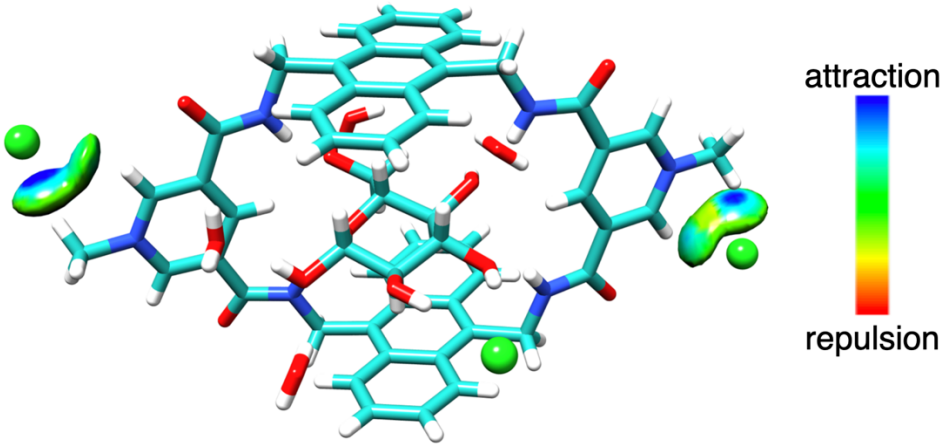

Fig. S107. IGM analysis of glucose⊂BPAT^{2+}•2Cl^{-} showing a noncovalent interaction isosurface of δg^{inter} = 0.005 a.u at the allosteric sites; color coding in the electron density range of –0.05<sign (λ_2)ρ <+0.05 a.u.

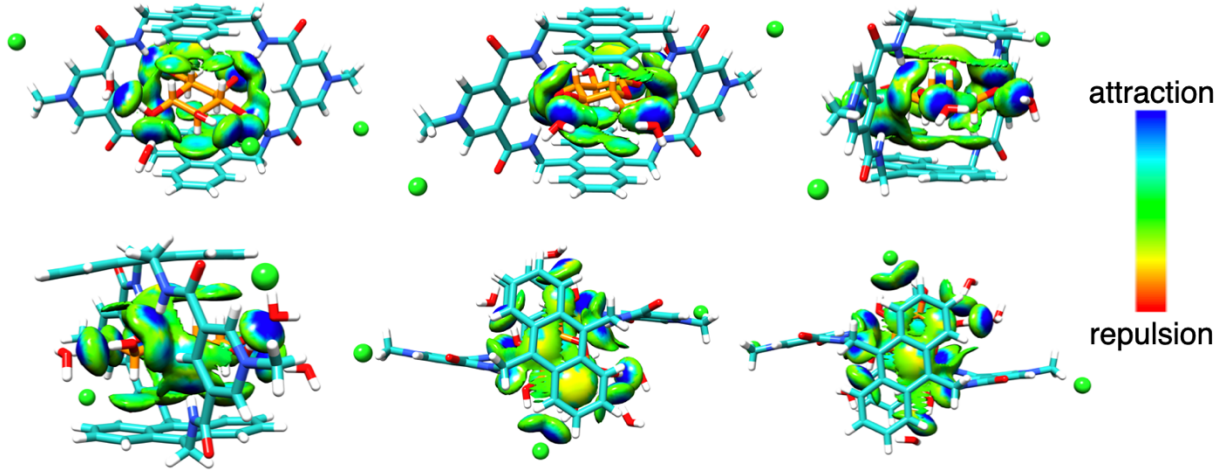

Fig. S108. IGM analysis of glucose⊂BPAT^{2+}•2Cl^{-} showing a noncovalent interaction isosurface of δg^{inter} = 0.005 a.u around the glucose; color coding in the electron density range of –0.05<sign (λ_2)ρ <+0.05 a.u.

Volume Calculation

The volume of BPAT^{2+} was calculated using MoloVol software[S23]. DFT optimized structure was used as input. Two spherical probes (small probe radius: 1.2 Å, large probe radius: 3 Å) were used to define cavities with a grid resolution of 0.2 Å and an optimization depth of 4.

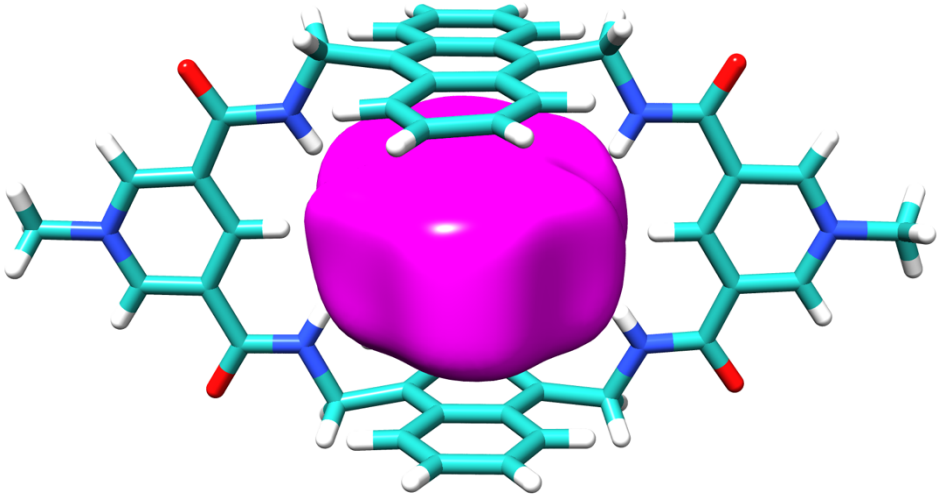

Fig. S109. Calculated cavity volume of $BPAT^{2+}$ represented by the purple colored isosurface.

Molecular Dynamic Simulation

Molecular dynamics simulations were performed using the Gromacs 2023.2 package.[S24] These simulations utilized the general AMBER force field[S25,S26] (GAFF) for $BPAT^{2+}$•$2Cl^-$, a molecule not previously characterized in terms of force constants. As a result, the positions of the $BPAT^{2+}$•$2Cl^-$ atoms were confined during the simulations. The amber99sb force field[S27, S28] was employed for water molecules, along with the Tip4pEW explicit water model[S29]. For the $BPAT^{2+}$•$2Cl^-$, atomic charges were fitted to the Restrained Electrostatic Potential (RESP) using the Multiwfn program[S18]. This fitting was based on single-point calculations derived from crystal structure geometries. These calculations were performed using the ORCA 5.0.3 package[S10] at the BLYP/SVP level of theory. The topology file of $BPAT^{2+}$•$2Cl^-$ was prepared using the Sobtop 1.0 program[S30]. The simulations were conducted in an NPT ensemble, maintaining a constant temperature of 300 K. The simulation was performed within a 4.0 nm edge-length cubic box designed to accommodate both the $BPAT^{2+}$•$2Cl^-$ and the water molecules. The simulations spanned 10 nanoseconds with a time step of 1 femtosecond, following the energy minimization and equilibration of the systems. The hydration of small molecules equilibrates in the timescale of picoseconds; the simulated time of 10 ns was enough to provide a robust statistic for the host solvation.[S31]

Conformer search

Conformer search was performed using Conformer-Rotamer Ensemble Sampling Tool (CREST) program[S32, S33]. X-ray single crystal structures or DFT-optimized structures were used as input for the sampling.

Constrains files were firstly created for anthracene panels and the rest of the resides in the input files was allowed for free movement during the sampling process. The MD/MTD time step was set as 1 fs, a GBSA implicit solvation for water was used, and the sampling was performed at the SQM level of GFN2-xTB.

Surface-Area Overlap (SAO) Analysis

Surface-area overlap analysis[S34] was performed by Chimera and Image J software. Single crystal structures[S35] of the receptor-substrate complex were truncated by removing the top half of the receptors and visualized by Chimera. The glucose and receptors were colored to show the bridging units, the binding cavity of the receptor, the area of glucose, and the overlapping portion between the receptor and glucose. ImageJ 1.49 software was used to measure the percent of SAO in each glucose-substrate complex. Values were calculated for the SAO-glucose (the overlapping portion between the receptor and glucose divided by the total area of the glucose).

Computational analysis of the binding mechanism

To uncover the underlying factors that contributed to the distinctive binding behaviors demonstrated by $BPAT^{2+}$ in both its free and aggregated states, we performed density functional theory (DFT) calculations at the BLYP-D3/SVP level. We used the X-ray single crystal structure of glucose ⊂ $BPAT^{2+}$•$2Cl^-$ as our starting point, optimizing this structure within a polarizable continuum solvent model in water. Our calculations revealed (Fig. S110a and 110b) that the energy (Fig. S103 and S104) of glucose ⊂ $BPAT^{2+}$•$2Cl^-$ with both allosteric sites occupied by Cl^- anions is 0.9 kcal/mol higher compared to the free macrocycle in complex with glucose (glucose ⊂ $BPAT^{2+}$). The electrostatic potential maps of $BPAT^{2+}$ (Fig. S110d) and $BPAT^{2+}$•$2Cl^-$ (Fig. S110e) indicated that chloride binding at the allosteric sites neutralizes the macrocycle's charge. This neutralization diminishes the pyridinium units' ability to polarize the inward-facing C–H bonds, weakening hydrogen bonding strength.

Moreover, the optimized structure of glucose ⊂ $BPAT^{2+}$ displayed a binding pattern to glucose slightly different from that observed in the solid state. In the optimized structure, one of the inward-facing C–H hydrogen bond donors is oriented (Fig S110a and S110b) towards the 4-hydroxyl group

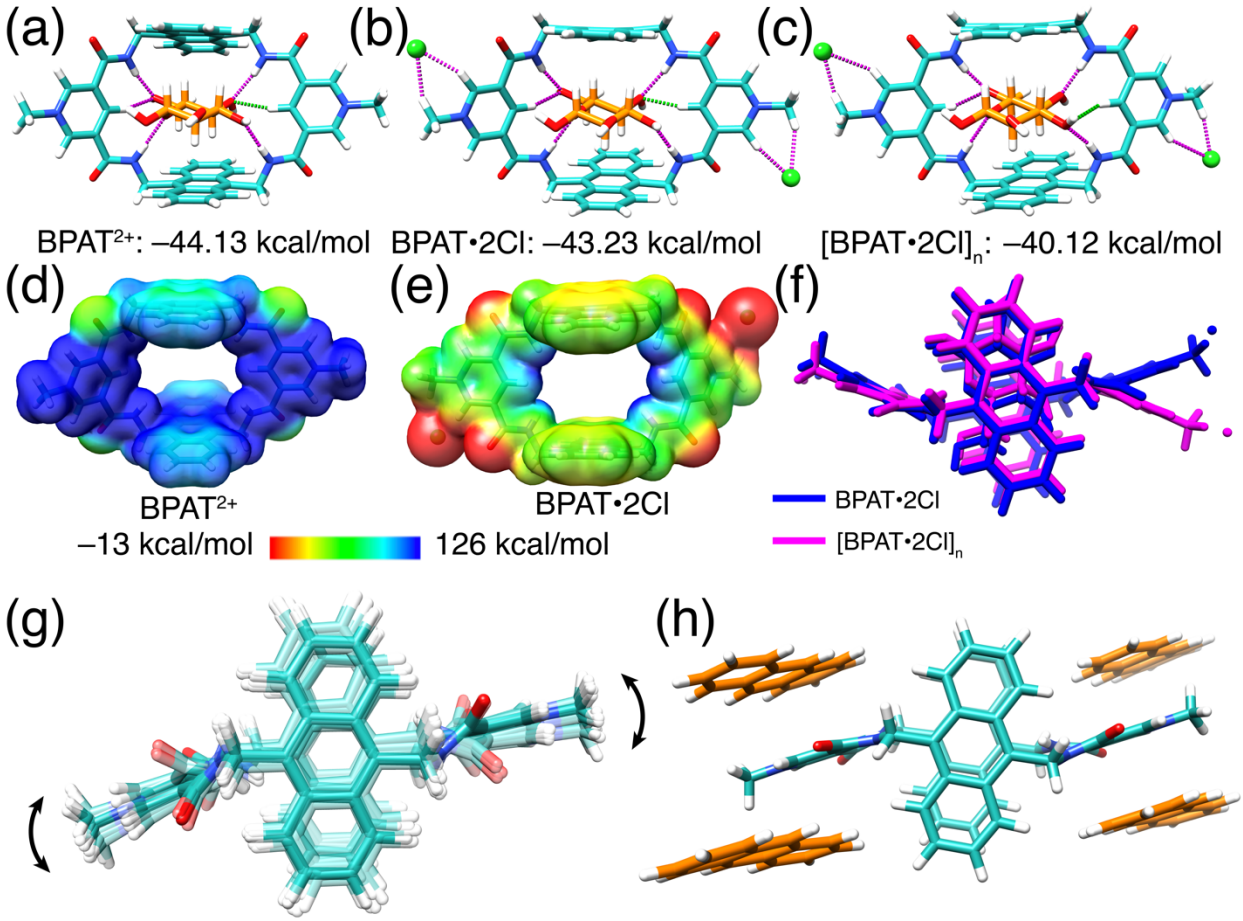

Fig. S110. DFT optimized structures and their corresponding binding energies of (a) glucose⊂$BPAT^{2+}$ and (b) glucose⊂$BPAT^{2+}$•$2Cl^{-}$. (c) X-ray single crystal structure of glucose⊂$BPAT^{2+}$•$2Cl^{-}$ and DFT-derived binding energies. Electrostatic potential maps of (d) $BPAT^{2+}$and (e) $BPAT^{2+}$•$2Cl^{-}$. (f) An overlay of DFT optimized structure (blue) of glucose⊂$BPAT^{2+}$•$2Cl^{-}$ with its x-ray single crystal structure (magenta). Magenta dashes represent the same type of hydrogen bonds between the optimized and solid-state structures while the green dashed line represents the different types of hydrogen bonds. (g) Overlay of low-energy conformers of $BPAT^{2+}$ identified by CREST program. (h) The only low-energy conformational isomer identified by the CREST program in the presence of two anthracene panels sandwiched between each pyridinium unit.

of glucose. In contrast, in the solid-state structure (Fig. S110c), this C–H bond is oriented towards the 3-hydroxyl group. The variation in binding patterns results in a higher energy state by 3.1 kcal/mol (Fig. S110b and S110c) when the C–H hydrogen bond donor targets the 3-hydroxyl group

in the solid state. An overlay of the optimized structure of glucose ⊂ $BPAT^{2+}$•$2Cl^-$ with its solid-state counterpart ([glucose ⊂ $BPAT^{2+}$•$2Cl^-$]$_n$) demonstrates (Fig. S110f) differences in the orientation of the pyridinium units, which influence the direction of the hydrogen bond donors' interaction with glucose. These results point to a combined effect of the macrocycle's charge neutralization and the misorientation of the pyridinium panels in contributing to the lower affinity observed in aggregated $BPAT^{2+}$•$2Cl^-$ compared to the free macrocycle.

The DFT calculations suggest that the macrocycle, in its solid state, cannot achieve optimal binding with glucose. Based on this observation, we propose (Fig. S110g and S110h) that $BPAT^{2+}$ has a flexible binding pocket in its free state, where the pyridinium units are associated with a rocking motion. This structural flexibility enables the macrocycle to adapt the direction of hydrogen bonding by reorienting the pyridinium units to accommodate the glucose's functional group distribution. In contrast, in the aggregated state (Fig. S110h), the aromatic stacking between macrocycles freezes the pyridinium units, resulting in a rigidified binding pocket. This rigidity prevents the reorientation of the hydrogen bonding sites, leading to suboptimal binding with glucose and a consequent reduction in affinity.

To test this hypothesis, we employed constrained conformational sampling of $BPAT^{2+}$ using the Conformer-Rotamer Ensemble Sampling Tool (CREST) program, applying constraints to the anthracene panels while allowing the pyridinium units to move freely. This approach identified ten low-energy conformers of $BPAT^{2+}$. An overlay of these ten conformers (Fig. S110g) demonstrated the structural flexibility of the pyridinium units, which can oscillate without impacting the molecule's overall low-energy state. To simulate the aggregated state, we positioned two anthracene panels adjacent to each pyridinium unit, akin to their arrangement in the solid-state structure. While the anthracene panels were fixed, the pyridinium units were left free to move. As anticipated, this restricted setup yielded only one conformer (Fig. S110h), supporting our hypothesis that the anthracene panels froze the pyridinium units, preventing them from reorienting to optimally bind glucose.

Our hypothesis is further supported by the experimental data from circular dichroism (CD) absorption spectroscopy. When $BPAT^{2+}$ binds glucose in its free state, it induces (Fig. 5a) strong

CD absorption peaks between 220-270 nm. These pronounced CD signals imply that the non-chiral $BPAT^{2+}$, in its free state, can adjust its conformation to bind chiral glucose, forming a well-defined chiral complex. In contrast, aggregated $BPAT^{2+}•2Cl^-$ under identical conditions exhibits (Fig. 5b) similar but significantly weaker CD signals. Notably, the strongest CD peak, occurring at 260 nm and associated with pyridinium absorption, is much less intense in the aggregated state than in the free state. This difference in peak intensity suggests that in its aggregated form, $BPAT^{2+}•2Cl^-$ has a more rigid structure, making it less effective at forming the indued chiral complex. These results suggest that hydrogen-bonding receptors with rigid molecular skeletons may not be able to establish optimal noncovalent interactions with substrates. Instead, the incorporation of flexible hydrogen bonding residues inside the binding pocket could facilitate substrate binding.

11. References

S1 P. Thordarson, *Chem. Soc. Rev.*, 2011, **40**, 1305–1323.
S2 D. Brynn Hibbert and P. Thordarson, *Chem. Commun.*, 2016, **52**, 12792–12805.
S3 APEX4 Software / Chemical Crystallography Bruker, Madison, Wisconsin, USA. 2022.
S4 Bruker SAINT Bruker AXS LLC, Madison, Wisconsin, USA.
S5 L. Krause, R. Herbst-Irmer, G. M. Sheldrick and D. Stalke, *J Appl Crystallogr*, 2015, **48**, 3–10.
S6 G. M. Sheldrick, *Acta Crystallogr A Found Adv*, 2015, **71**, 3–8.
S7 G. M. Sheldrick, *Acta Crystallogr C Struct Chem*, 2015, **71**, 3–8.
S8 O. V. Dolomanov, L. J. Bourhis, R. J. Gildea, J. A. K. Howard and H. Puschmann, *J Appl Crystallogr*, 2009, **42**, 339–341.
S9 A. L. Spek, *Acta Crystallogr E Cryst Commun*, 2020, **76**, 1–11.
S10 F. Neese, *WIREs Comput Mol Sci*, 2012, **2**, 73–78.
S11 A. D. Becke, *The Journal of Chemical Physics*, 1993, **98**, 5648–5652.
S12 F. Weigend and R. Ahlrichs, *Phys. Chem. Chem. Phys.*, 2005, **7**, 3297.
S13 H. Kruse and S. Grimme, *The Journal of Chemical Physics*, 2012, **136**, 154101.
S14 S. Grimme, J. Antony, S. Ehrlich and H. Krieg, *The Journal of Chemical Physics*, 2010, **132**, 154104.
S15 F. Weigend, *Phys. Chem. Chem. Phys.*, 2006, **8**, 1057.
S16 R. Izsák and F. Neese, *The Journal of Chemical Physics*, 2011, **135**, 144105.
S17 G. L. Stoychev, A. A. Auer and F. Neese, *J. Chem. Theory Comput.*, 2017, **13**, 554–562.
S18 T. Lu and F. Chen, *J Comput Chem*, 2012, **33**, 580–592.
S19 Y. Zhang and J. Zhao, *J Comput Chem*, 2023, **44**, 806–813.
S20 J. Zhang and T. Lu, *Phys. Chem. Chem. Phys.*, 2021, **23**, 20323–20328.
S21 E. F. Pettersen, T. D. Goddard, C. C. Huang, G. S. Couch, D. M. Greenblatt, E. C. Meng and T. E. Ferrin, *J Comput Chem*, 2004, **25**, 1605–1612.
S22C. Lefebvre, G. Rubez, H. Khartabil, J.-C. Boisson, J. Contreras-García and E. Hénon, *Phys. Chem. Chem. Phys.*, 2017, **19**, 17928–17936.
S23J. B. Maglic and R. Lavendomme, *J Appl Crystallogr*, 2022, **55**, 1033–1044.
S24B. Hess, C. Kutzner, D. Van Der Spoel and E. Lindahl, *J. Chem. Theory Comput.*, 2008, **4**, 435–447.
S25J. Wang, R. M. Wolf, J. W. Caldwell, P. A. Kollman and D. A. Case, *J Comput Chem*, 2004, **25**, 1157–1174.
S26J. Wang, W. Wang, P. A. Kollman and D. A. Case, *Journal of Molecular Graphics and Modelling*, 2006, **25**, 247–260.
S27V. Hornak, R. Abel, A. Okur, B. Strockbine, A. Roitberg and C. Simmerling, *Proteins*, 2006, **65**, 712–725.
S28E. J. Sorin and V. S. Pande, *Biophysical Journal*, 2005, **88**, 2472–2493.
S29H. W. Horn, W. C. Swope, J. W. Pitera, J. D. Madura, T. J. Dick, G. L. Hura and T. Head-Gordon, *The Journal of Chemical Physics*, 2004, **120**, 9665–9678.
S30T. Lu, Sobtop (version 1.0) http://sobereva.com/soft/Sobtop.
S31. F. Biedermann, W. M. Nau, H. J. Schneider, *Angew. Chem. Int. Ed.* **2014**, *53*, 11158–11171.
S32 P. Pracht, F. Bohle and S. Grimme, *Phys. Chem. Chem. Phys.*, 2020, **22**, 7169–7192.
S33S. Grimme, *J. Chem. Theory Comput.*, 2019, **15**, 2847–2862.
S34 W. Liu, S. Bobbala, C. L. Stern, J. E. Hornick, Y. Liu, A. E. Enciso, E. A. Scott, J. Fraser Stoddart, *J. Am. Chem. Soc.* **2020**, *142*, 3165–3173.

S35 P. K. Mandal, B. Kauffmann, H. Destecroix, Y. Ferrand, A. P. Davis, I. Huc, *Chemical Communications* **2016**, *52*, 9355–9358.